UNIVERSITY OF CALIFORNIA,
IRVINE

A Fully Integrated Frequency-Domain Diffuse Optical Imaging System in 180 nm Standard CMOS

DISSERTATION

submitted in partial satisfaction of the requirements
for the degree of

DOCTOR OF PHILOSOPHY

in Electrical Engineering

by

Siavash Sedighzadeh Yazdi

Dissertation Committee:
Professor Michael Green, Chair
Professor G.P. Li
Associate Professor Ozdal Boyraz

2017

DEDICATION

To my family

TABLE OF CONTENTS

LIST OF FIGURES

LIST OF TABLES

ACKNOWLEDGMENTS

I would like to express my most sincere gratitude to my mentor and PhD advisor Prof. Michael Green for his support, guidance and patience as well as all the invaluable discussions we shared during the last five years. He is one of the nicest and most thoughtful persons I have ever known. He gave me enough time to learn, enough freedom to find my own way, and enough guidance to keep me in the right direction. Not many graduate students I know, enjoy working with their advisors, but that was never the case for me. Thank you Mike!

I am thankful to my dissertation committee members Prof. G.P. Li and Prof. Ozdal Boyraz for their guidance and for judging my work.

I would also like to thank Dr. Albert Cerussi and Prof. Bruce Tromberg, our collaborators at Beckman Laser Institute. Albert introduced this topic of research to me and shared his invaluable information on the topic. Bruce made this project possible with his support and strategic vision.

Many thanks to Prof. Nader Bagherzadeh, Dr. Ashkan Eghbal and Dr. Pouria Yaghini for their collaborative research.

The friends I made during these past years are like family to me. They have made my life happier. Ashkan who has one of the biggest hearts, Bahareh who is always full of energy, Arash with his funny and sometimes insipid jokes, Soroush the news guru, Kimia with her artistic soul, cheerful Negar, and Ali with his tendency to overthink are only some of the great friends I made these years. Thank you guys for all the good memories! I look forward to many more years of friendship.

My family are the ones to whom I truly owe all my accomplishments.
My parents, who always told me that I can achieve whatever I want, are my safe havens. They helped me with everything I needed to focus on my studies, to stay confident and to aim higher. Though, geographically apart, they are always with me. My Mom who, like all other mothers, is always worried about me and my Dad who, like many other fathers, doesn't express his feelings verbally, both have always put my happiness before their owns. I know I can never make up for all their sacrifice. Thank you Mom! Thank you Dad!
Hossein, whom I know I can always count on, is a truly supportive brother. Thank you Hossein!
Finally, I would like to thank my Elmira, for sharing all the ups and downs of life with me during these years. I would indefinitely be grateful for the sacrifices she made to be with me. Without her love and encouragement, this work was not possible. Thank you Elmira! You have made me a better person.

CURRICULUM VITAE

Siavash Sedighzadeh Yazdi

EDUCATION

Doctor of Philosophy in Electrical Engineering **2017**
University of California, Irvine *Irvine, California*

Master of Science in Electrical Engineering **2014**
University of California, Irvine *Irvine, California*

Bachelor of Science in Electrical Engineering **2011**
Sharif University of Technology *Tehran, Iran*

RESEARCH EXPERIENCE

Graduate Research Assistant **2012–2017**
University of California, Irvine *Irvine, California*

TEACHING EXPERIENCE

Teaching Assistant **2012–2016**
University of California, Irvine *Irvine, California*

PUBLICATIONS

1. S. Yazdi and M. Green, "A precise 360-range phase detector based on an N-path filter," in *2016 14th IEEE International New Circuits and Systems Conference (NEWCAS)*, June 2016.

2. S. S. Yazdi, A. E. Cerussi, and M. M. Green, "A precise 360-range phase detector for fdNIRS application using a pair of XNORs," in *2015 IEEE 58th International Midwest Symposium on Circuits and Systems (MWSCAS)*, Aug 2015.

3. H. S. Yazdi, T. D. O'Sullivan, A. Leproux, B. Hill, A. Durkin, S. Telep, J. Lam, S. S. Yazdi, A. M. Police, R. M. Carroll, F. J. Combs, T. StrÃűmberg, A. G. Yodh, and B. J. Tromberg, "Mapping breast cancer blood flow index, composition, and metabolism in a human subject using combined diffuse optical spectroscopic imaging and diffuse correlation spectroscopy," *Journal of Biomedical Optics*, vol. 22, pp. 22 – 22 – 10, 2017.

4. A. Eghbal, P. M. Yaghini, S. S. Yazdi, and N. Bagherzadeh, "Tsv-to-tsv inductive coupling-aware coding scheme for 3d network-on-chip," in *Defect and Fault Tolerance in VLSI and Nanotechnology Systems (DFT), 2014 IEEE International Symposium on*. IEEE, 2014, pp. 92–97.

5. P. M. Yaghini, A. Eghbal, S. S. Yazdi, N. Bagherzadeh, and M. M. Green, "Capacitive and inductive tsv-to-tsv resilient approaches for 3d ics," *IEEE Transactions on Computers*, vol. 65, no. 3, pp. 693–705, 2016.

6. P. M. Yaghini, A. Eghbal, S. S. Yazdi, and N. Bagherzadeh, "Accurate system-level tsv-to-tsv capacitive coupling fault model for 3d-noc," in *Proceedings of the 9th International Symposium on Networks-on-Chip*. ACM, 2015.

ABSTRACT OF THE DISSERTATION

A Fully Integrated Frequency-Domain Diffuse Optical Imaging System in 180 nm Standard CMOS

By

Siavash Sedighzadeh Yazdi

Doctor of Philosophy in Electrical Engineering

University of California, Irvine, 2017

Professor Michael Green, Chair

Frequency-domain diffuse optical imaging (fd-DOI) systems require accurate phase and amplitude measurement of the modulating signal for precise calculation of optical properties of a medium. To reach this accuracy, the current time-resolved DOI methods are prohibitively complex, bulky, and expensive, and generally not compatible with the vision of compact wearable devices. In this dissertation, for the first time, a complete fd-DOI transceiver unit is implemented on a chip. Using only standard CMOS technology to reduce the cost, this transceiver paves the way for complete integration of a time-resolved DOI SoC. Novel methods for measuring phase and amplitude are introduced to enable accurate measurement over more than a decade of frequencies and 60 dB input dynamic range. The systems reaches an optical sensitivity of -57 dBm at 400 MHz modulation frequency with phase and amplitude measurement accuracy of 2° and 1dB, respectively. Works like this along with the advances in the vertical cavity surface emitting lasers (VCSELs) and CMOS-integrated photodiodes will enable the development of new methods and devices with the accuracy, precision, and power of time-resolved techniques, but the simplicity, low cost, and wearability of CW devices.

Chapter 1

Introduction

There is an urgent need for more powerful and cost-effective wearable and bedside technologies to meet the needs of healthcare providers and patients for personalized medicine and personal health. With nearly $18B of venture investment in "digital health" between 2011-2016 [1] this much anticipated transformation of medicine is already underway. However, many conventional strategies are insufficient and there are clear opportunities for new technologies to meet this rapidly growing demand.

Tissue optical spectroscopy is widely used in biomedical research and clinical medicine to characterize and image perfusion, metabolism, and molecular composition and can potentially provide new approaches to meet this challenge. Biomedical scientists have developed optical methods for detection, diagnosis, and therapeutic guidance in virtually all major areas of medicine, including: neurologic disease, cancer, cardiovascular disease, diabetes, obesity, metabolic disease, and trauma/critical care. Recent animal and human studies utilizing optical spectroscopy include mapping and assessing brain activation [2–4], identifying and tracking cerebral ischemia [5, 6], studying the progression and treatment of breast cancer [7–11], and studying muscle composition and metabolism [12, 13]. In addition, the

diffuse photoplethysmographic (PPG) waveform is essential for assessing heart rate in personal health monitors (e.g. FitBit, Apple Watch, etc.) as well as in medical devices for tissue oximetry and continuous blood pressure monitoring.

While much of this work is conducted using time-independent, continuous-wave (CW) illumination methods that assess changes in light intensity, a significant and growing body of work shows that time-resolved methods, which employ high-speed modulated (e.g. >50 MHz) or picosecond-pulsed sources to measure changes in the temporal dispersion of light, have powerful advantages. Unlike CW techniques that typically do not account for alterations in optical scattering that can occur during the measurement period and between individuals, time-resolved measurements have the ability to quantitatively determine optical path length and excited state lifetime in centimeter-thick, multiply-scattering tissues by measuring either the phase velocity or temporal dispersion of modulated or pulsed sources, respectively. As a result, time-resolved methods in both the time- and frequency-domain are used to separate light absorption from scattering, measure fluorescence lifetime, and provide substantially greater information content vs. CW intensity alone [14]. Their quantitative features allow for absolute comparisons between individuals and longitudinal monitoring of subjects with exceptional accuracy and precision over days, weeks, months, and years. Unfortunately, current time-resolved methods are prohibitively complex, bulky, and expensive, and generally not compatible with the vision of compact wearable devices.

The goal of this work is to develop a quantitative diffuse optical imaging (DOI) sensor that will increase the applicability and scalability of quantitative DOI technology, while reducing the cost and making it more accessible for research and education. Specifically, a CMOS integrated circuit implementation of the broadband transceiver to perform frequency-domain photon migration (FDPM) for quantitative tissue spectroscopy is implemented. This FDPM engine will enable quantitative sensing of tissue composition and metabolism and high-speed quantitative photoplethysmography in a wearable form factor. Such a device has significant

research and commercial applications. The FDPM IC will also dramatically improve the scalability of quantitative DOI by reducing the size and cost required for high-density, multi-channel sensing as is required for brain functional imaging using Diffuse Optical Tomography (DOT).

In the second chapter of this dissertation, the theory, physics, and some simple math behind the diffuse optical spectroscopy are explained. In the third chapter, the overall system architecture is explained. Chapters 4-7 explain the architecture and circuit-level implementation of the main building blocks, frequency synthesizer, receiver front-end, receiver baseband, and transmitter, respectively. Chapter 8 includes the measurement results for the fabricated chip. Chapter 9 discusses the future work and concludes this work.

Chapter 2

Diffuse Optical Imaging Basics and Theory

Diffuse Optical Imaging (DOI) is a noninvasive medical technique for imaging and/or monitoring of tissue architecture and function [10]. It is noninvasive since there is no need for biopsy or any other surgical procedure in this method. This technique, also known as Near-InfraRed Spectroscopy (NIRS), utilizes near-infrared light (optical wavelengths from 650 to 950 nm) to gain information from the tissue inside the body. In this range of optical wavelengths (also known as the medical window), the photon absorption rate of the water molecules present in the body is low and therefore light has the potential to travel deep into the tissue to provide information from parts of the body well below the surface of skin. Like any other optical imaging system a DOI system consists of two major parts: The source and the detector. A typical setup for a DOI experiment is shown in Fig. 2.1.

Based on the principles of operation, DOI systems can be categorized into three modalities described in the following sections [34].

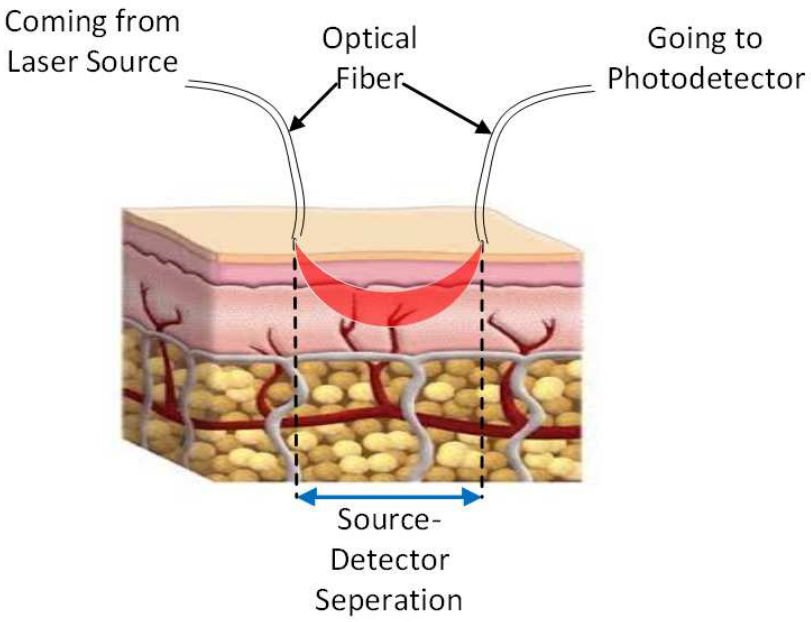

Fig. 2.1: Configuration of a typical DOI experiment

2.1 Continuous-Wave (CW) DOI

The most common and simplest form of a DOI system is continuous-wave or CW DOI. In this technique, a light source with a fixed intensity is continuously projected into the tissue. After the light travels through the tissue its intensity is detected by a photodetector and compared with the input light intensity. If the path-length that the light travels is known, the absorption rate of the medium can be calculated based on the amount of attenuation measured. Although this method is the least expensive, it is unable to measure the absolute concentration of different materials in the tissue since it is unable to take into account the scattering of light introduced by the turbid medium of tissue. However it can provide information regarding the relative change of each of these absorbers, which is used in most pulse oxymeters. In order to measure the absolute concentration of materials, there should be some means of measuring the scattering and separating its effect from the effect of absorption. Then based on the amount of absorption, the concentration of different absorbers can be calculated. To this goal, two other modalities of DOI exist, which will be explained next.

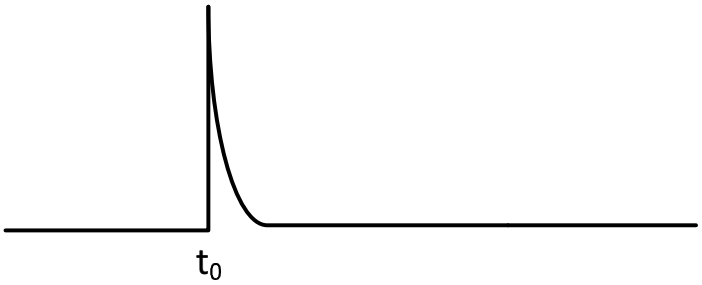

(a)

(b)

Fig. 2.2: Time Domain (a) Input and (b) Output Pulse

2.2 Time-Domain (TD) DOI

In the time-domain approach, also known as time-domain photon migration (TDPM), the light source is modulated with a narrow electrical pulse. On the detector side, a widened, attenuated version of the projected pulse is then detected (shown in Fig. 2.2). A narrow time-domain pulse includes a wide range of frequency contents; therefore the detected pulse includes a vast amount of information encompassing a range of frequencies. Based on the amount of attenuation and pulse widening, important information about the absorption and scattering coefficients of the medium can be obtained. The drawback with TD-DOI is the stringent timing resolution required and the need for photon counting photodetectors which makes the electronics complex and power-hungry. Thus this technique is not suitable for low-power wearable operation.

2.3 Frequency-Domain(FD) DOI

Another method that is a good compromise between the accuracy of TD-DOI and simplicity of CW-DOI is frequency-domain DOI (FD-DOI). In this method, also known as frequency-domain photon migration (FDPM), a continuous light source is modulated by a sinusoidal signal before being projected into the tissue. At the detector side the dc attenuation, ac attenuation, and phase shift of the light, shown in Fig. 2.3(a), are then measured. The analytical solution of the photon migration inside a semi-infinite medium is used [15]. The data obtained from the FD-DOI measurements for different modulation frequencies are fit into this analytical solution in order to obtain the absorption coefficient and reduced scattering coefficient at a specific wavelength. This measurement can then be repeated for multiple wavelengths of light. Based on the calculated values, absorption can be separated from scattering, and the absolute concentration of different absorbers inside the tissue (e.g. water, fat, oxygenated hemoglobin, and deoxygenated hemoglobin) can be calculated. The block diagram of the FD-DOI system is shown in Fig. 2.3(b). In the block diagram, the modulator is responsible for modulating the power of the laser source. Following the photodetecor, there is a phase and amplitude measurement block. The controller synchronizes different blocks and adjusts the modulation frequency and wavelength of the laser (for the case of a super-continuum laser or multiple laser diodes). It is also responsible for sending the data acquired from the experiment to a processing unit for data fitting and extracting optical properties.

2.3.1 FD-DOI Theory

The analytical solution to the photon movements inside the tissue start with transport theory. For light in highly scattering media – e.g. NIR light in tissue – it can be shown that transport theory simplifies to Fick's laws of diffusion at points far from the source or strong

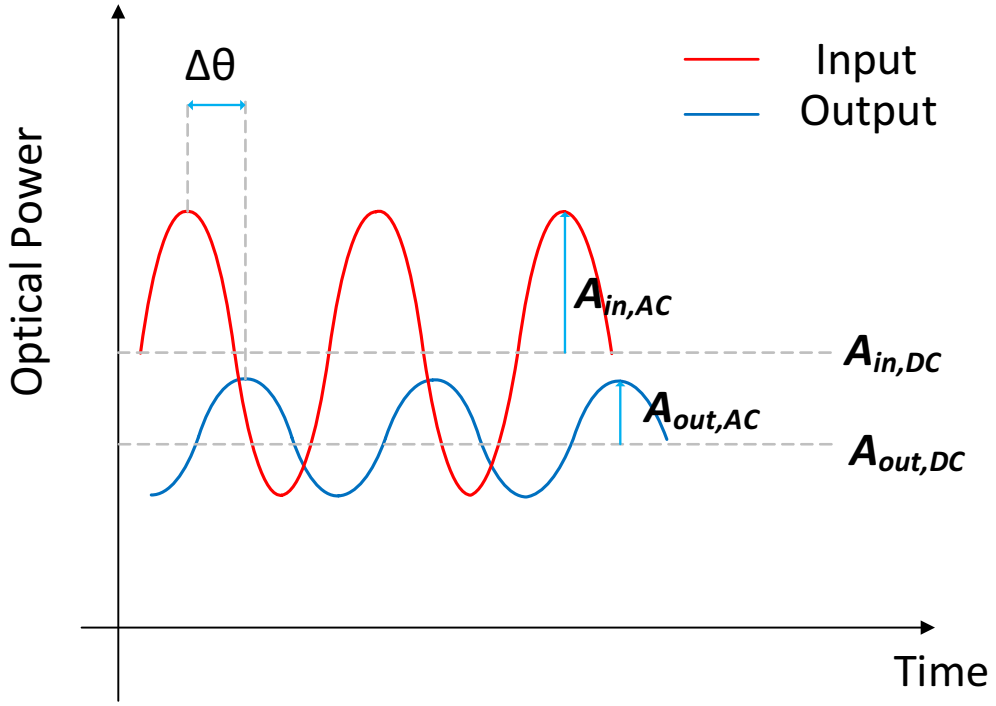

(a)

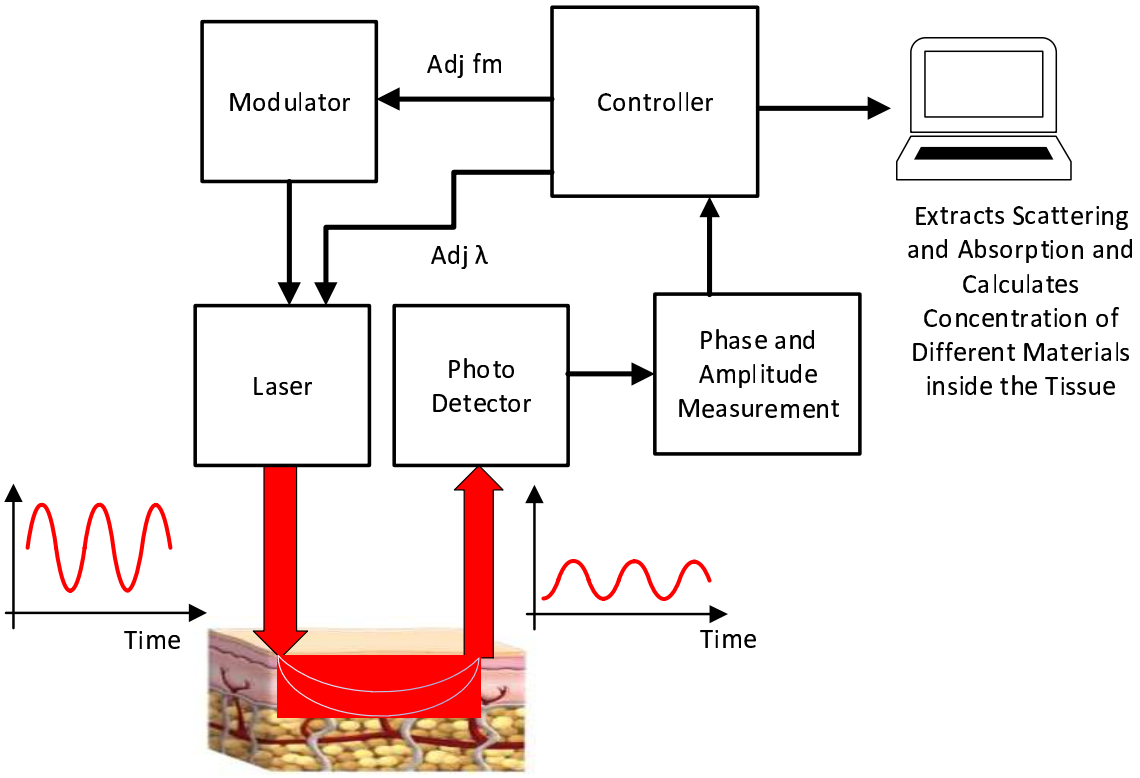

(b)

Fig. 2.3: Frequency Domain DOI System: (a) Input and Output Waveform; (b) Block Diagram.

absorbers [16]. Based on Fick's first law:

$$J = -\chi \frac{\partial C}{\partial x} = -D \frac{\partial \phi}{\partial x} \tag{2.1}$$

where J is the flux $[\frac{\mathrm{W}}{\mathrm{cm}^2}]$ in the x [cm] direction; $C = \frac{\phi}{c}$ is the concentration of optical energy $[\frac{\mathrm{J}}{\mathrm{cm}^3}]$; ϕ is the fluence rate $[\frac{\mathrm{W}}{\mathrm{cm}^2}]$; $\chi = cD$ is the diffusivity $[\frac{\mathrm{cm}^2}{\mathrm{s}}]$; c is the speed of light in the medium [cm/s]; and $D = \frac{1}{3(\mu_a + \mu_s')}$ [cm] is the diffusion length, in which μ_a is the absorption coefficient $[\mathrm{cm}^{-1}]$ and μ_s' is the reduced scattering coefficient of the medium $[\mathrm{cm}^{-1}]$. The mean free path of the light $l_{tr} = 1/(\mu_a + \mu_s')$ is defined as the mean distance a photon travels inside a medium before being absorbed or scattered. (2.1) states that optical flux goes from points with higher optical energy concentration to points with lower energy concentration. Fick's first law is valid for steady state and does not take into effect time-varying changes in concentration. Fick's second law considers such variations; its 1-dimensional form can be written as:

$$\frac{\partial C}{\partial t} = \chi \frac{\partial^2 C}{\partial x^2} \tag{2.2}$$

If the source of light is an isotropic point source, the generic solution to (2.2) with respect to space and time will be in the form of Green's function:

$$C(r,t) = Q \frac{exp[-r^2/(4\chi t)]}{(4\pi\chi t)^{3/2}} \tag{2.3}$$

where Q [J] is the energy of the point source at origin ($r = 0$) at $t = 0$. (2.3) gives the concentration of optical energy at time t [sec] at a distance r [cm] from the origin but does

not include the effect of absorption. In order to take its effect into account the right side of (2.3) should be multiplied by a factor of $\exp(-\mu_{\mathrm{a}}\mathrm{ct})$, where ct is the pathlength that the photon travels in time t, and μ_a [cm^{-1}] is the absorption coefficient of the medium. If in (2.3), C is replaced with ϕ/c and χ with cD the following equation will be obtained for the fluence rate (ϕ) in a scattering and absorbing medium:

$$\phi_1(r,t) = cQ\frac{exp[-r^2/(4cDt)]}{(4\pi cDt)^{3/2}}exp(-\mu_a ct) \tag{2.4}$$

It should be noted that this function (ϕ_1) describes the diffusion of light from an isotropic impulse source of light with an energy of Q applied at $r = 0$ and at $t = 0$. To obtain the steady-state response to a continuous source of light, as in CW-DOI, we can assume the impulse repeats every T seconds and therefore the fluence rate will be the sum of the responses to each of the individual impulse sources:

$$\phi(r,t) = \sum_{n=0}^{\infty} \phi_1(r, t-nT)u(t-nT) \tag{2.5}$$

where $u(t)$ is the step function. If Q and T both approach zero while Q/T is held constant with value P [W], it is straightforward to show that the above sum can be written in integral form. For very long times ($t \to \infty$), the fluence rate will reach its steady-state value, which can be written as:

$$\phi(r) = \lim_{t\to\infty} \phi(r,t) = \lim_{t\to\infty} \frac{1}{T}\int_{t'=0}^{t} \phi_1(r,t')dt' = P\frac{exp(-r/\delta)}{4\pi Dr}. \tag{2.6}$$

In this equation δ [cm] is the optical penetration depth and is related to the optical properties

through (2.7):

$$\delta = \sqrt{\frac{D}{\mu_a}} = \frac{1}{\sqrt{3\mu_a\left(\mu_a + \mu_s'\right)}}. \tag{2.7}$$

The inverse of this penetration depth is known as the effective attenuation coefficient $\mu_{eff} = 1/\delta$ [cm^{-1}]. The integration in (2.6) is not straightforward but it can be calculated using conservation of energy as shown in [17]. This equation shows the steady-state value of the fluence rate at a distance r while an optical isotropic point source located at $r = 0$ radiates a constant optical power (P) into the medium for the case of a CW source.

In order to obtain the equations for frequency-domain diffuse optical spectroscopy, we next assume the input power source amplitude is sinusoidally modulated:

$$P(t) = P_0(1 + m_0 \sin \omega t) \tag{2.8}$$

where P_0 [W] is the average optical power, m_0 [dimensionless] is the modulation depth and ω [rad/s] is the angular modulation frequency of the source. As shown in [16], the fluence rate for the amplitude-modulated light source inside the medium is:

$$\phi(r) = P_0 \frac{exp(-r/\delta)}{4\pi D r}\left[1 + m_0\ exp(-r(k'' - 1/\delta))\ sin(\omega t - k'r)\right] \tag{2.9}$$

where k' [cm^{-1}] and k'' [cm^{-1}] are:

$$k' = \frac{1}{\delta\sqrt{2}} \left[\left(1 + (\frac{\omega}{\mu_a c})^2 \right)^{1/2} - 1 \right]^{1/2}, \tag{2.10}$$

$$k'' = \frac{1}{\delta\sqrt{2}} \left[\left(1 + (\frac{\omega}{\mu_a c})^2 \right)^{1/2} + 1 \right]^{1/2}. \tag{2.11}$$

Therefore by comparing the input optical power in (2.8) to the power at a distance r from the source shown in (2.9) we can infer some important results. First, the average power is attenuated by a factor of $\frac{exp(-r/\delta)}{4\pi Dr}$ as expected. Second the modulation depth is attenuated by a factor of $exp(-r(k''-1/\delta))$ and finally the modulation phase is shifted by $k'r$. Therefore we can write:

$$phase = k'r \tag{2.12}$$

$$m = m_0 \; exp(-r(k'' - 1/\delta)). \tag{2.13}$$

The modulation depth and phase both depend on the modulation frequency and on optical properties of the medium through the coefficients k' and k''. In FDPM spectroscopy, amplitude and phase of the modulated light will be measured and compared with the source of light. Using the measured phase shift and modulation depth of the detected light, and by knowing the source detector separation (r) and modulation frequency (ω) the values of the k' and k'' can be calculated from (2.13). The values of μ_s' and μ_a can then be calculated from k' and k''.

The formulations derived up to this point are all based on two assumptions: First, that the optical source is isotropic and the optical power radiates evenly in all directions; second, that the medium is infinite without any boundaries. However in reality, neither of these is true. Regarding the first assumption, the light source used is usually a laser coupled to the surface of the tissue through an optical fiber, thus making it highly dimensional rather than

isotropic. However it can be shown [18] that the directional light of the fiber can still be very well approximated with an isotropic point source at the depth of l_{tr} below the surface of the tissue. Regarding the second assumption, it should be mentioned that spectroscopy is a noninvasive imaging technique and therefore the light source and photo detector are placed on the surface of the body, which means the boundary between the air and body should be considered in deriving the formulas. The simplest model that approximates tissue for spectroscopy is a homogeneous semi-infinite medium. The method of images [18] can be employed to find the diffusion equation for the semi-infinite medium having a boundary with air. Therefore the diffusion equation for the problem of the directed light projected into a semi-infinite homogeneous medium at its surface, shown in Fig. 2.4(a), is equivalent to the problem of Fig. 2.4(b) while the fiber is replaced with an isotropic point source (at depth l_{tr} under the surface of the medium) and the boundary is modeled by a negative point source at height $(l_{tr} + 2z_b)$ above the surface, where $z_b = 2l_{tr}\frac{1+R_{eff}}{3(1-R_{eff})}$ [cm] and R_{eff} [dimensionless] is the effective reflection coefficient due to optical index mismatch between tissue and air. The diffusion equation can then be obtained using superposition due to the two (positive and negative) point sources.

$$\phi(\rho, z = 0) = \frac{P_0}{4\pi cD}\left[\frac{exp(-kr_1)}{r_1} - \frac{exp(-kr_b)}{r_b}\right], \tag{2.14}$$

where,

$$r_1 = \sqrt{{l_{tr}}^2 + \rho^2}, \tag{2.15}$$

$$r_b = \sqrt{(2z_b + l_{tr})^2 + \rho^2}, \tag{2.16}$$

$$k = k'' - ik'. \tag{2.17}$$

In the above equations cylindrical coordinates are used to simplify the equations with the

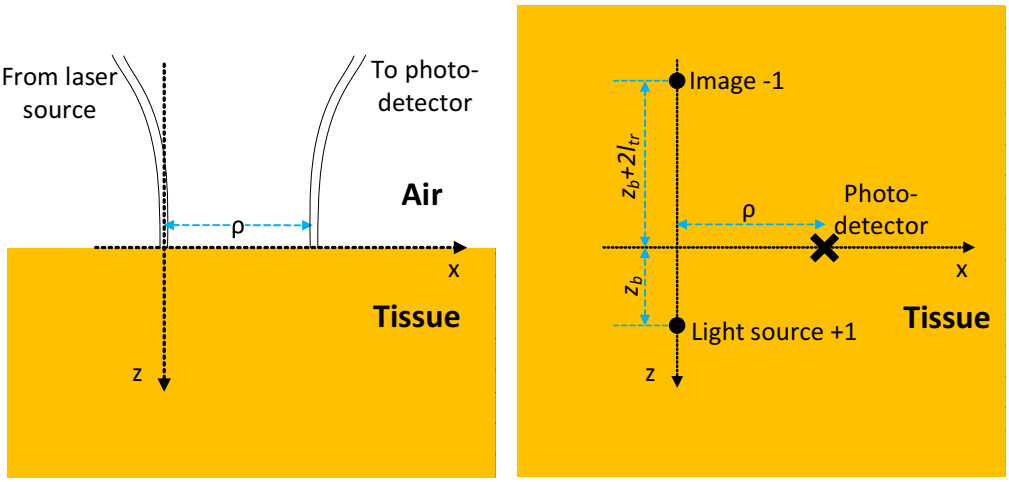

(a) (b)

Fig. 2.4: Method of images applied to solve the diffusion equation for the semi-infinite medium: (a) Experimental configuration; (b) light source fiber replaced by a point light source at $z = z_b$ (Light source +1) and the boundary is replaced with an equivalent point image source (Image -1) at $z = -(z_b + 2l_{tr})$

x and z axes defined as shown in Fig. 2.4. In this coordinate system $z = 0$ is the surface of the semi-infinite medium and the source fiber is located at $z = 0$ and $\rho = 0$ while the photo detector (or the fiber coupled to it) collects light at a distance ρ from the source on the surface (i.e. located at $z = 0$ and ρ). If $\rho \gg (l_{tr} + 2z_b)$ then (2.14) can be simplified to:

$$\phi(\rho, z = 0) \approx \frac{P_0}{4\pi cD} \frac{exp(-k\rho)}{\rho^2} \left(2k \left(l_{tr} + {z_b}^2\right)\right) = A(\rho)\ exp(i\theta(\rho)). \tag{2.18}$$

where,

$$\ln\left(\rho^2 \frac{A(\rho)}{A_0}\right) = -k''\rho, \tag{2.19}$$

$$\theta(\rho) = -k'\rho + \theta_0. \tag{2.20}$$

After measuring the amplitude and phase shift of the detected light with respect to the

input light, these values can be used in (2.14) or (2.18) to fit for the values of the μ_s' and μ_a. In addition to the parameters explained previously, the detected light signal amplitude and phase are related to some experimental parameters that are difficult to predict theoretically. Therefore in a real FD-DOI system the measurements are usually done at multiple source-detector separations or at multiple modulation frequencies to enable calibration of the system and reduce the systematic errors.

2.3.2 Tissue Chromophore Concentration Calculation

The absorption rate of the tissue depends on the absorption rate of the chromophores forming the tissue and their absorption. The wavelength-dependent absorption coefficient of a tissue can be written as:

$$\mu_a(\lambda) = \sum_i \varepsilon_i(\lambda)\ c_i \tag{2.21}$$

where ε_i and c_i are the extinction coefficient and concentration of the ith chromophore, respectively. The extinction coefficients of tissue chromophores (e.g. water, fat, oxygenated hemoglobin and deoxygenated hemoglobin) as a function of wavelength are known, as shown in Fig. 2.5. If the absorption rate of the tissue at M different wavelengths is measured, a system of M coupled equations will be obtained that can be solved to find the concentration

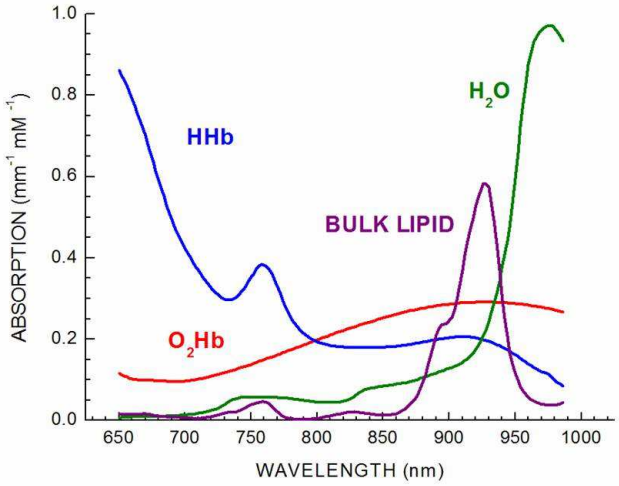

Fig. 2.5: Extinction Coefficient of Tissue Chromophores

of each of the N chromophores ($M \geq N$):

$$\begin{bmatrix} c_1 \\ c_2 \\ \vdots \\ c_N \end{bmatrix} = \begin{bmatrix} \varepsilon_1(\lambda_1) & \varepsilon_2(\lambda_1) & \cdots & \varepsilon_N(\lambda_1) \\ \varepsilon_1(\lambda_2) & \varepsilon_2(\lambda_2) & \cdots & \varepsilon_N(\lambda_2) \\ \vdots & \vdots & \ddots & \vdots \\ \varepsilon_1(\lambda_M) & \varepsilon_2(\lambda_M) & \cdots & \varepsilon_N(\lambda_M) \end{bmatrix}^{-1} \begin{bmatrix} \mu_a(\lambda_1) \\ \mu_a(\lambda_2) \\ \vdots \\ \mu_a(\lambda_M) \end{bmatrix} \tag{2.22}$$

The FD-DOI method can be employed to find the absorption rate at different optical wavelengths. For the purpose of pulse oxymetry, only the concentrations of two chromophores – oxygenated and deoxygenetad hemoglobin – are of interest and therefore two different optical wavelengths – one more sensitive to the oxygenated (∼830nm) and the other more sensitive to the deoxygenated (660-780nm) – are used. For other applications when the concentration of fat, water, or other chromophores inside the body is of interest, other wavelengths are used.

The accuracy of the overall system depends on how accurately absorption and scattering rate can be measured. In order to achieve high resolution in measuring the optical proper-

ties the FD-DOI system should be able to measure amplitude and phase shift accurately. Experiments have shown that phase accuracy is the most important between the two parameters [14]. Fig. 2.6 (a) and (b) show how 1% and 10% changes in the absorption and scattering coefficients, respectively, affect the measured phase vs. frequency. In this experiment, simulated in Virtual Photonics [19], the phase shift is measured once for the base optical properties and then for the cases when absorption and scattering coefficient increased from their baseline values by 1% and 10%. The change in measured phase from the baseline measurement is then plotted vs. frequency for each of the cases. This experiment is done for a source-detector separation of 20 mm. The base optical properties considered for this simulation are $\mu_a = 0.1$ cm^{-1} and $\mu_s' = 10$ cm^{-1}. This graph shows the importance of accurate phase measurement for accurate extraction of optical properties. For example, in Fig. 2.6(b) at frequencies about 1 GHz, a 1% change in absorption introduces about 0.3° change in measured phase. Therefore a FDPM system with a phase resolution of 0.3° or better is required to measure changes as small as 1% in the absorption coefficient. This graph also illustrates the benefit of operating at higher frequencies. For example a 1% change in the scattering coefficient introduces about 0.1° phase change at 100 MHz while it introduces about 1° at 1 GHz. Hence if the FDPM system can keep its phase measurement accuracy at higher frequencies, the system can resolve smaller changes of chromophore concentration.

Considering the importance of accuracy in measuring phase and amplitude for accurate detection of optical properties of the tissue, the focus of this research is on finding precise measuring techniques that can be adapted over a wide frequency range to enable multi-frequency FDPM measurement. The next chapter explains the overall architecture of the proposed system to achieve this goal.

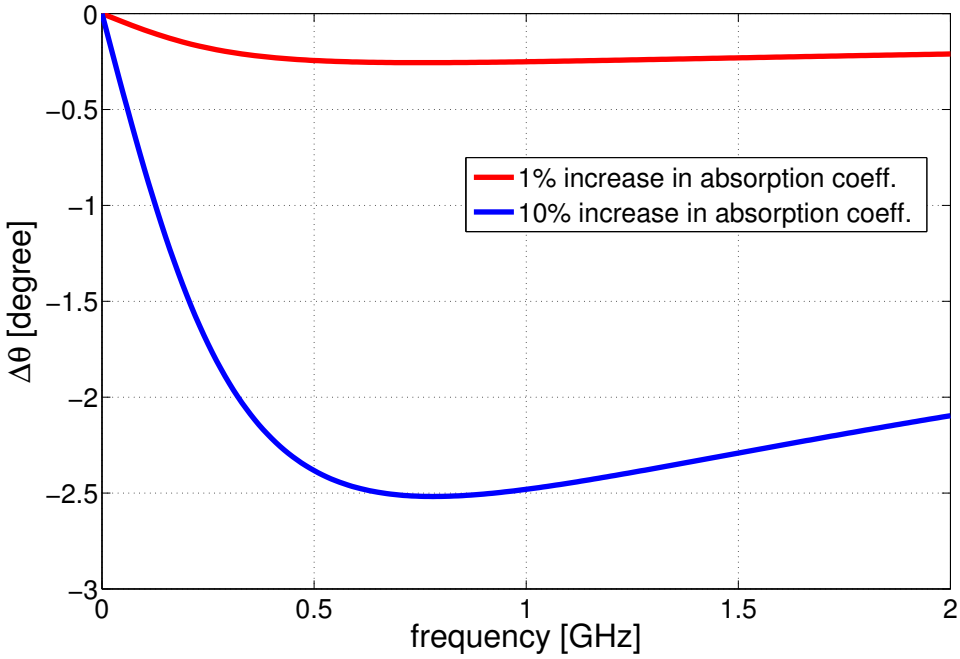

(a)

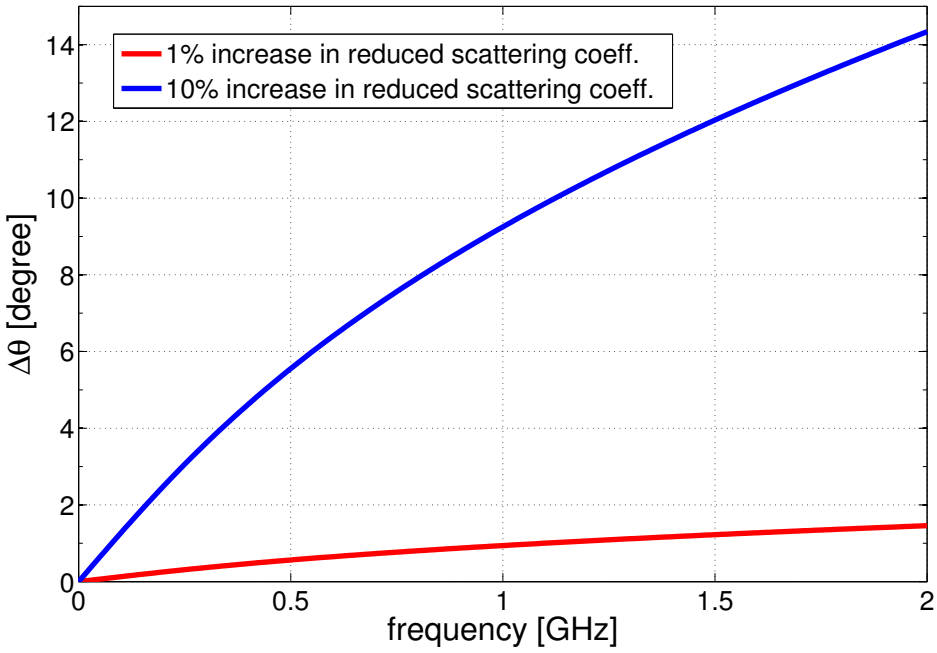

(b)

Fig. 2.6: Effect of changes in (a) absorption coefficient and (b) reduced scattering coefficient in measured phase vs. frequency.

Chapter 3

FDPM System

FDPM instrumentation size and complexity have been dramatically reduced over the past 25 years driven, in large part by advances in telecommunications technologies. An early demonstration of broadband FDPM relied on a benchtop Ar-ion pumped tunable laser with a Pockels cell modulator [15]. One of the first portable instruments (Fig. 3.1(a)) suitable for use in a medical clinic was large (60" x 24" x 24") and used laser diodes modulated with a swept RF source provided by a network analyzer at a total cost of $80k. The current incarnation of a broadband FDPM module, shown in Fig. 3.1(b), is a PCB-based integration of off-the-shelf and custom RF components and is about the size of an external hard drive (5" x 6" x 2") [20]. This module was developed at the UC Irvine Beckman Laser Institute, costs $3k, and is currently being used in clinical studies. However, this module is neither easily scalable to multiple-channel sensing, nor suitable for continuous wearable sensing, an area that is clearly the next frontier both in terms of research and commercial impact. Moreover, since it uses a collection of commercial chips connected together on a printed circuit board, each input and output operating at the RF modulating frequency must be terminated by 50Ω resistors, which requires many line drivers that dissipate substantial power. An advantage of a single-chip implementation is that only two terminations are needed — one at the output

(a) (b)

Fig. 3.1: FDPM implementations: (a) 1st generation RF network analyzer based FDPM system (60" x 24" x 24"); (b) 2nd generation PCB-based FDPM module (5" x 6" x 2").

of the transmitter, and the other at the input of the receiver.

Recently, Sthalekar and Koomson developed a single-frequency (100 MHz) fd-NIRS chip in standard CMOS [21]. They followed this work with an 80MHz chip fabricated on a BiCMOS 130 nm process [22]. This chip has an extended dynamic range of 60 dB using an on-chip transimpedance amplifier (TIA). This single-wavelength, single source-detector design had 0.5° phase accuracy and clearly established that frequency-domain tissue optical spectroscopy can be practically implemented using CMOS technologies. However, unlike our broadband multi-frequency approach where absorption, scattering, and fluorescence properties can be determined using a single, fixed, source-detector "view" by sweeping through multiple modulation frequencies, single-frequency operation requires that multiple measurements be taken over different source-detector separation distances, which can limit performance in layered tissue structures. Moreover, the relatively low 80 MHz frequency may have insufficient sensitivity to separate multiple processes (absorption, fluorescence, scattering) in complex tissues. Our proposed chip design includes a number of advantages: First, it allows for a range of modulating frequencies from 50 MHz to 1 GHz and features fast measurement times of tens

of microseconds per frequency. Second, our design includes an internal signal generator, which can significantly reduce the power dissipation of the system. Therefore, the reference signal is readily available on chip, eliminating the need for a separate reference detection path. Third, our proposed ASIC employs, in addition to the receiver front end, baseband processing (i.e. the amplitude and phase detection) implemented on chip. Auto calibration and offset cancelling mechanisms provide very accurate measurement of phase and amplitude without additional signal processing. The on-chip phase detector has a resolution of 0.1 degrees at 100 MHz. The amplitude detector has a detection range of 60 dB and the receiver front-end provides 40 dB to 120 dB gain adjustability in 10dB steps providing overall wide dynamic range. The detailed block diagram of the proposed integrated FDPM CMOS chip is shown in Fig. 3.2. The boundary between the on-chip circuitry and its peripherals is designated with a dotted black line. As shown all the main building blocks except diodes (Laser diodes and avalanche photo detector), the laser driver and the controller are included on the chip. The controller adjusts the modulation frequency by adjusting the control voltage applied to a quadrature voltage-controlled oscillator. The quadrature outputs of the signal generator will be low-pass filtered to reduce their harmonic content retaining only the first harmonic. The filtered in-phase output of the oscillator is fed as a current into the external laser driver, which modulates one of the four laser diodes (selected by the digital bits coming from the controller). The laser driver has to provide a large current amplitude at frequencies up to 1GHz and thus would be inefficient if implemented in CMOS. The modulated light will pass through the tissue under test and the attenuated phase-shifted light will be detected by the avalanche photodiode. This attenuated light will be amplified by the internal gain of the APD, as well as the TIA and variable gain amplifiers (VGA) following the APD. The amplified signal will be filtered by an N-path filter whose baseband output will be used for phase and amplitude detection. The outputs of the phase and amplitude detectors are dc voltages for each test, which will be sampled by the internal ADC of the controller. Multiple tests with different modulation frequencies and optical wavelengths, and possibly multiple

source detector separations will be performed and recorded by the controller. All the building blocks will be discussed in more detail in Chapters 4-7.

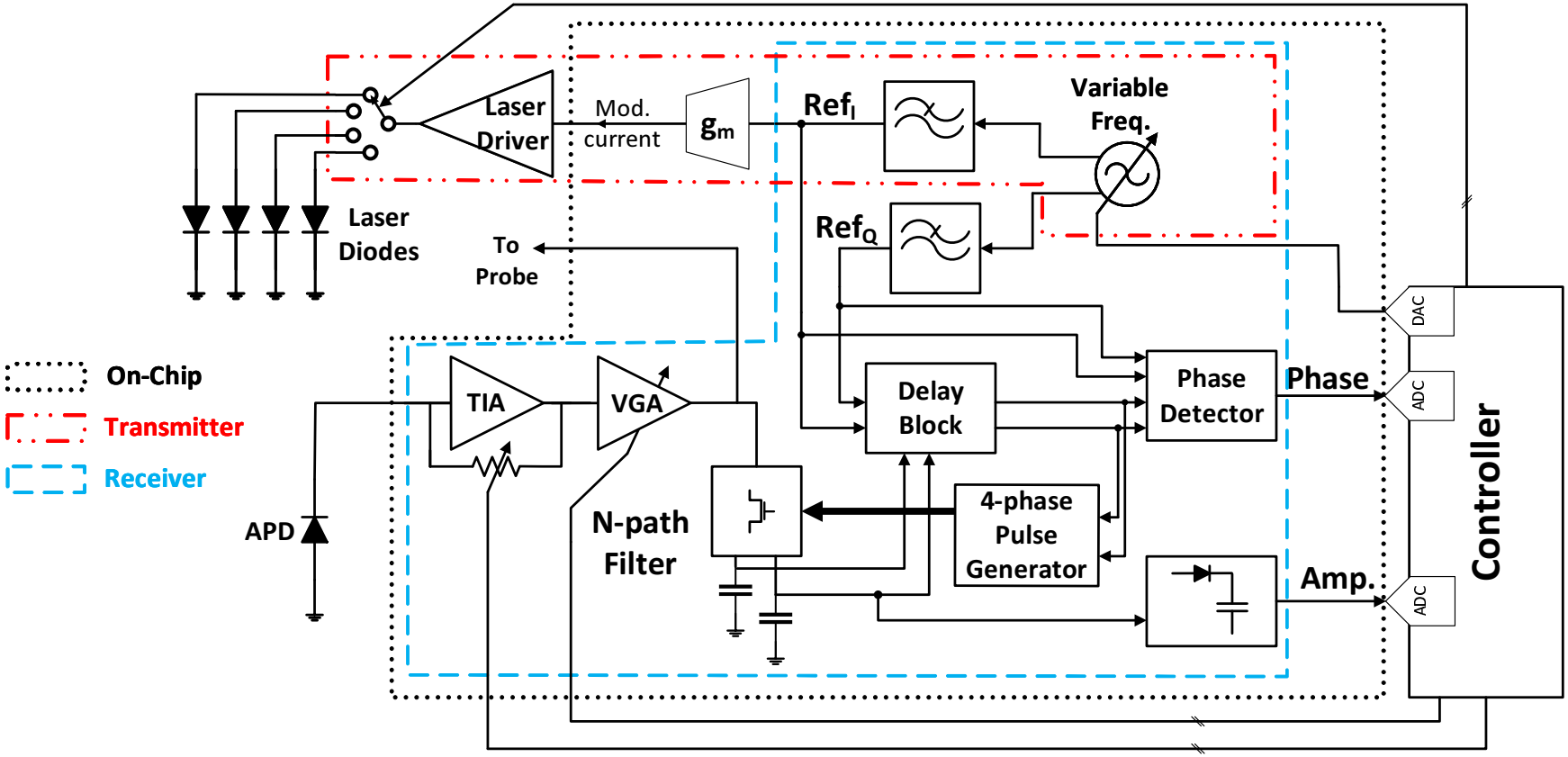

Fig. 3.2: Architecture of proposed Integrated CMOS FDPM chip

Chapter 4

Frequency Synthesizer

One of the main building blocks of the FDPM chip is the frequency synthesizer which should be able to generate sinusoidal signals for a wide range of frequencies –from 100 MHz to 1 GHz. To cover such a wide range of frequencies, three different methods can be employed which are discussed next. In the first method shown in Fig. 4.1(a), known as heterodyning, the outputs of two VCOs are mixed to generate a signal at a lower frequency. In this architecture one or both VCO's can have variable frequency. The benefit of this architecture compared with a single VCO is that the VCO can function with a more modest tuning range. For example one oscillator fixed at 2GHz and another one variable from 2.1-3 GHz (i.e. a tuning ratio of less than 1.5) can provide an output frequency in the range of 100 MHz-1 GHz. However this architecture has a number of drawbacks, including high power consumption (two oscillators both at higher frequencies compared to a single oscillator), mixing spurs, and possibly higher phase noise. The second architecture, depicted in Fig. 4.1(b), consists of multiple LC VCOs, each covering a portion of the overall range. This architecture is the best in terms of power consumption and phase noise performance since each VCO can be optimized for a limited frequency range. However this design is very area-demanding since it needs multiple LC tank circuits, some large enough to resonate at low frequencies. The

simplest and most area efficient design is a single ring oscillator with a wide tuning range as depicted in Fig. 4.1(c). In general, such a VCO will exhibit higher phase noise as compared to an LC VCO. A test VCO based on the third approach is implemented on chip, due to its compact area and wide tuning range.

The output of this ring-oscillator is a square-shaped signal. A $g_m - C$ biquad low-pass filter (LPF) is designed to follow this oscillator to generate clean sinusoidal signals for laser modulation as well as for proper operation of the phase interpolators (discussed in Chapter 6). The design of the VCO and LPF is explained in more detail in the next Section.

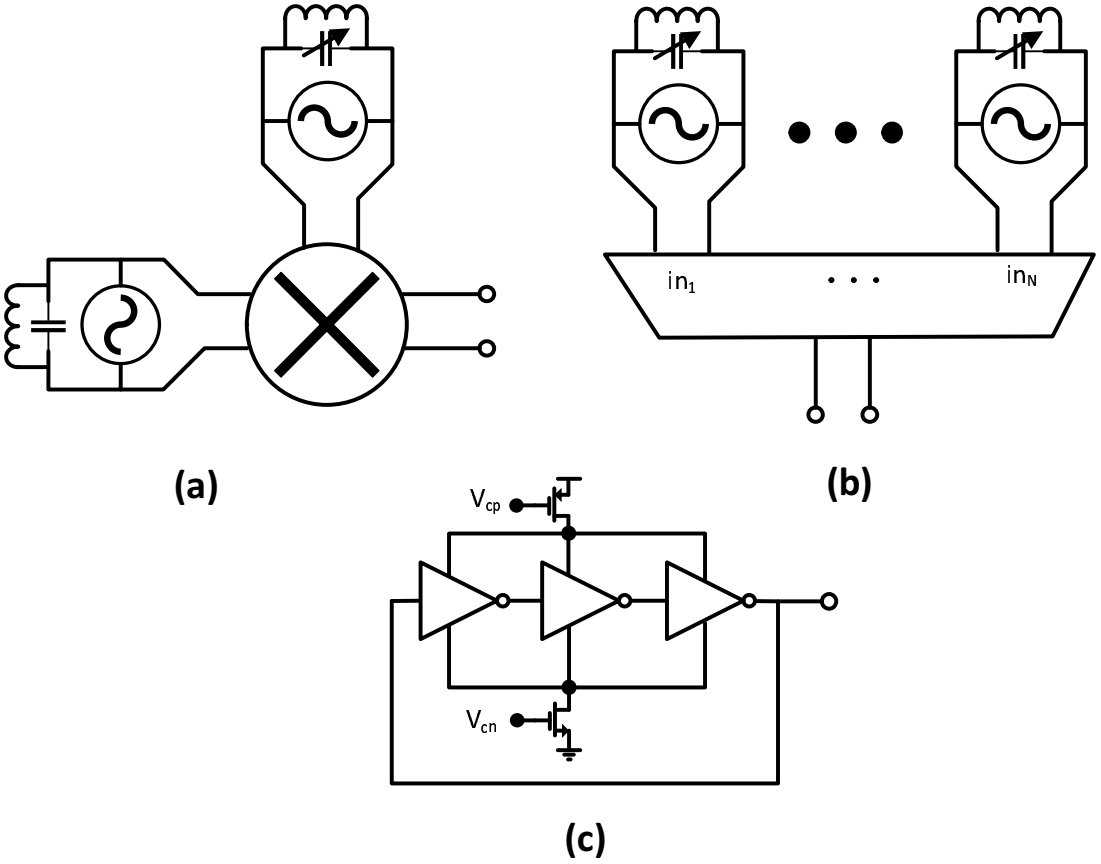

Fig. 4.1: Methods for generating signals over a wide frequency range

4.1 VCO Architecture

The architecture of the implemented VCO is shown in Fig. 4.2. As described in [23] this is a four-stage ring oscillator made up of inverters I_1 to I_4, with additional feed-forward paths, made up of inverters I_5 to I_8. Without the feed-forward paths the ring acts like a bistable circuit that will latch up to one of its two stable states and thus does not oscillate. Each feed forward inverter provides a negative G_m at its output, which forces the structure to oscillate. There is a limit to the size of the feed-forward inverter relative to the ring inverters that allows oscillation to occur. A PMOS current source and a NMOS current sink control the total amount of current available to the delay cells. The lower the current, the longer it takes for the capacitors to charge and discharge, and thus the lower the oscillation frequency.

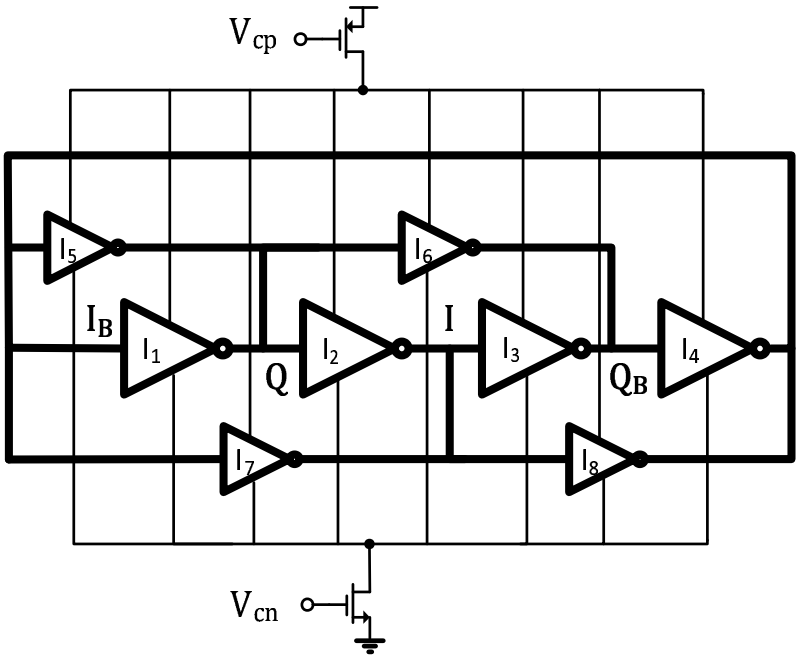

Fig. 4.2: Ring Oscillator Core

The circuit shown in Fig. 4.3 is the controller circuit for the Fig. 4.2 ring oscillator. The value of the voltage V_{tune} determines the amount of current going through the diode-connected PMOS transistor. The gate of the diode-connected PMOS is connected to V_{cp} in the oscillator core and a replica bias circuit (shown on the right end of Fig. 4.3), as well as the tail current

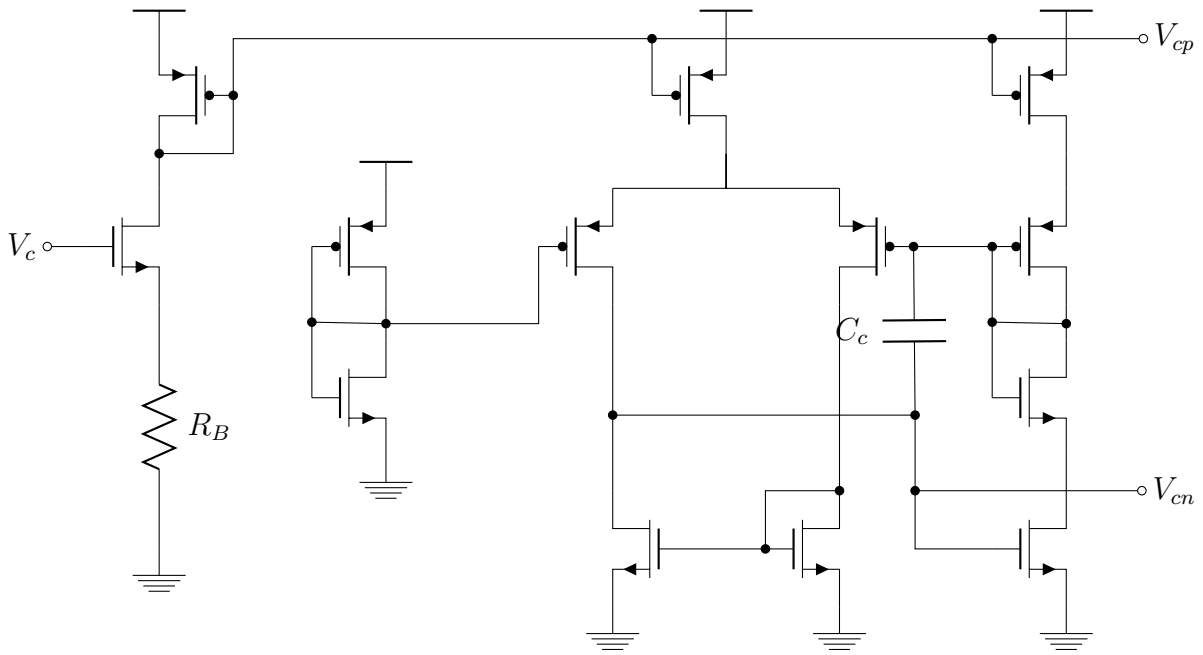

Fig. 4.3: VCO controller circuit

source of a differential amplifier. In order to make sure that the current of the PMOS current source and NMOS current sink in the core are matched, the differential amplifier compares the value at the output of the replica bias circuit to a reference voltage generated by connecting the input and output of an inverter and adjusts the gate voltage of the NMOS current source accordingly. This loop ensures that the delay cells of the ring are dc-biased at their transition point and therefore keeps the duty-cycle of the oscillation waveforms close to 50%.

4.2 VCO Performance

In this section we look at the performance of the VCO in terms of the characteristics like phase noise, tuning range, K_{vco}, harmonic content, power consumption, and area.

Tuning Range & K_{vco}

The output frequency of the VCO has a linear relationship with the log of the control current. In the final design, in order to minimize the number of pins required for controlling the VCO frequency, a simplified voltage-to-current conversion scheme is used as shown in Fig. 4.3.

Fig. 4.4 shows the output frequency vs. control voltage characteristic of the final ring oscillator. The slope of this curve at each point determines the rate of change of output frequency for a small change in control voltage. The average slope of this curve, also known as K_{vco}, is almost 570 MHz/V. The VCO can be tuned anywhere from below 10MHz to above 750MHz with a single input control voltage (tuning ratio of 75). The upper limit on the the frequency is due to the simple voltage-to-current conversion circuit employed, which limits the maximum available current to the oscillator core; otherwise the simulations show that the oscillation can go well above 1 GHz.

Harmonic Content

Figures 4.5 & 4.6 show the waveform of the oscillator at 100 MHz and 700 MHz, respectively. Existence of higher harmonics is evident in these waveforms. For the FDPM system, clean single-tone sine waves are required to modulate the laser diode. Also, as will be explained in Chapter 6, the phase interpolator works based on sine-waves. Although any kind of soft transition edges would work with the phase interpolator, the characteristic would be most linear in the absence of higher order harmonics.

The frequency content of these waveforms is shown in Fig. 4.7. In order to attenuate the 3rd, 5th and other harmonics an active $g_m - C$ filter is utilized, which will be explained in

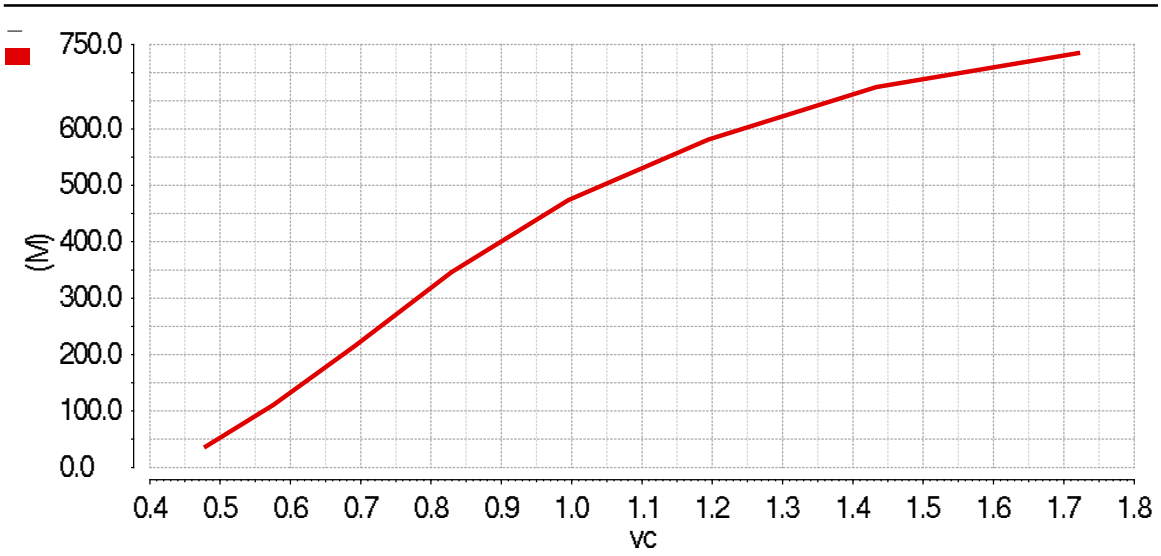

Fig. 4.4: VCO Oscillation Frequency vs. Control Voltage (V_{tune})

Section 4.3.

Power & Area

The designed VCO is low power. It only consumes about 660μA from a 1.8 V supply at 750 MHz oscillation frequency. Its layouts dimensions are $42 \times 38 \mu m$.

Phase Noise

The phase noise for oscillation frequencies of 100 MHz and 700 MHz is depicted in Fig. 4.8. Fig. 4.9 shows the phase noise at 10 MHz offset while the oscillation frequency is swept from 20 MHz to 700 MHz.

4.3 Bi-quad $g_m - C$ Filter

The FDPM system works with sinusoidal signals. The output of the VCO has significant power at odd harmonics as shown earlier. To get the best performance out of the system the VCO is followed by two identical 4^{th}-order bi-quad $g_m - C$ lowpass filters – one for in-phase

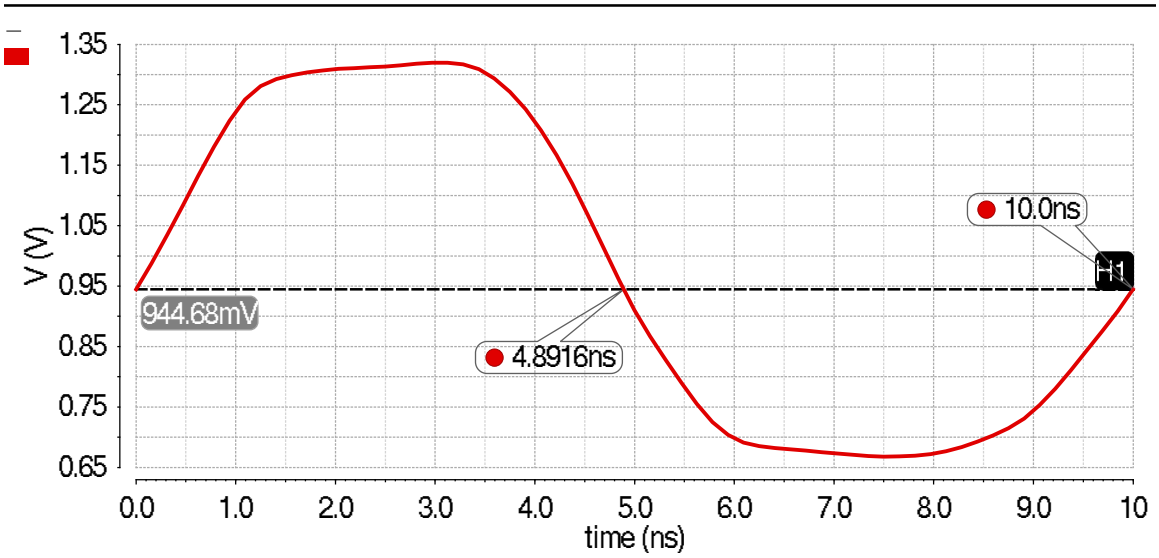

Fig. 4.5: VCO Waveform at 100 MHz

and one for quadrature components – that suppress the harmonics and output clean sine waves.

The filter consists of two second-order biquad stages [24]. The architecture of each stage is illustrated in Fig. 4.10; its transfer function is given by:

$$H(s) = \frac{\frac{g_{m1}}{g_{m4}}\frac{g_{m3}g_{m4}}{C_1C_2}}{s^2 + \frac{g_{m2}}{C_1}s + \frac{g_{m3}g_{m4}}{C_1C_2}} \tag{4.1}$$

Comparing (4.1) with a standard second-order system transfer function, we have:

$$\omega_0{}^2 = \frac{g_{m3}g_{m4}}{C_1C_2}, \tag{4.2}$$

$$\frac{\omega_0}{Q} = \frac{g_{m2}}{C_1}. \tag{4.3}$$

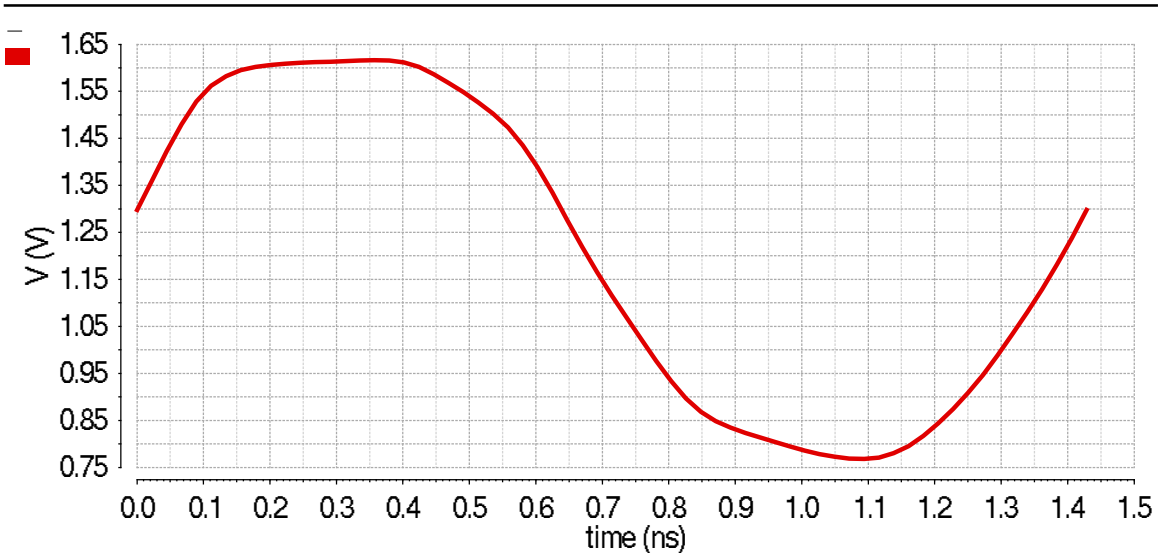

Fig. 4.6: VCO Waveform at 700 MHz

If $g_{m1} = g_{m3} = g_{m4} = g_m$ and $C_1 = C_2 = C$, then (4.1) and (4.1) simplify to:

$$\omega_0 = \frac{g_m}{C}, \tag{4.4}$$

$$Q = \frac{g_m}{g_{m2}}. \tag{4.5}$$

For a maximally-flat Butterworth frequency response, the quality factors of the first and second stages should be 1.307 and 0.541, respectively. However, for simplicity they are chosen to be 1 and 0.5, respectively. Therefore, in the first stage of the filter all four OTAs have equal sizes while in the second stage the second OTA has twice the size of the other three.

A control voltage adjusts the amount of current available to the OTAs, thereby uniformly changing their g_m's proportional to the square root of the bias current. Thus the Q of the filter stages remain constant because it is the ratio of two g_m values. But the corner frequency changes linearly with the bias current because it is proportional to ${g_m}^2$.

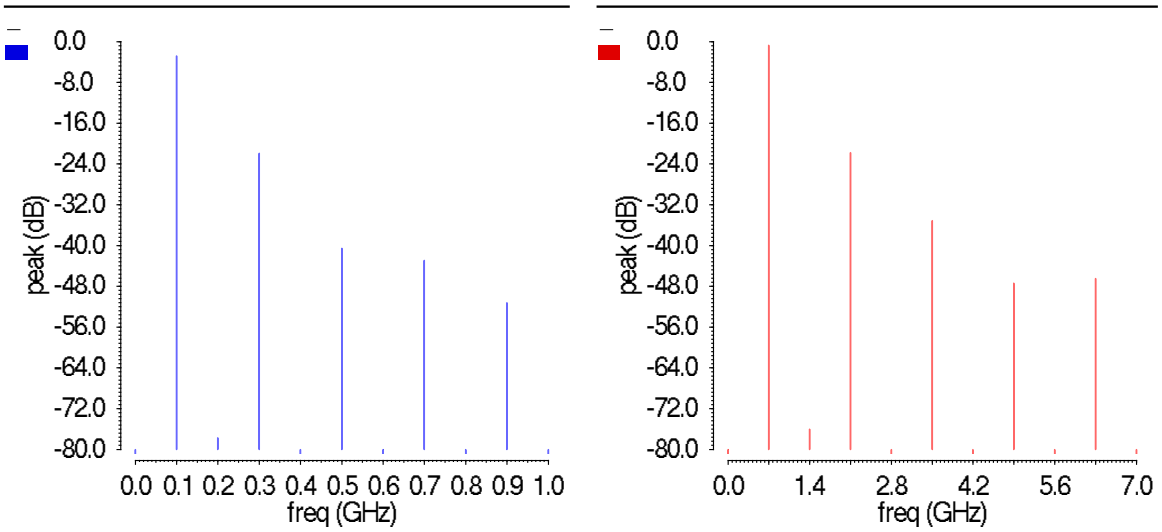

Fig. 4.7: Harmonic Content of the VCO Output at 100 MHz and 700 MHz

The OTAs are based on folded-cascode architecture depicted in Fig. 4.11. The bias circuit is depicted in Fig. 4.12. The lowpass filter bandwidth can be adjusted from below 50 MHz to above 1 GHz by varying the control voltage from 300 mV to 1.3 V. Fig. 4.13 shows the frequency response of the filter for different values of control voltage.

Fig. 4.14 and Fig. 4.15 show the input and output waveforms of the filter at 250 MHz and their harmonic contents, respectively. It can be observed that after filtering, the third harmonic is more than 40 dB below the first harmonic and the output waveform represents a single-tone sinusoidal signal, which will be buffered to modulate an external laser diode. This signal will also serve as the on-chip reference signal on the receiver side.

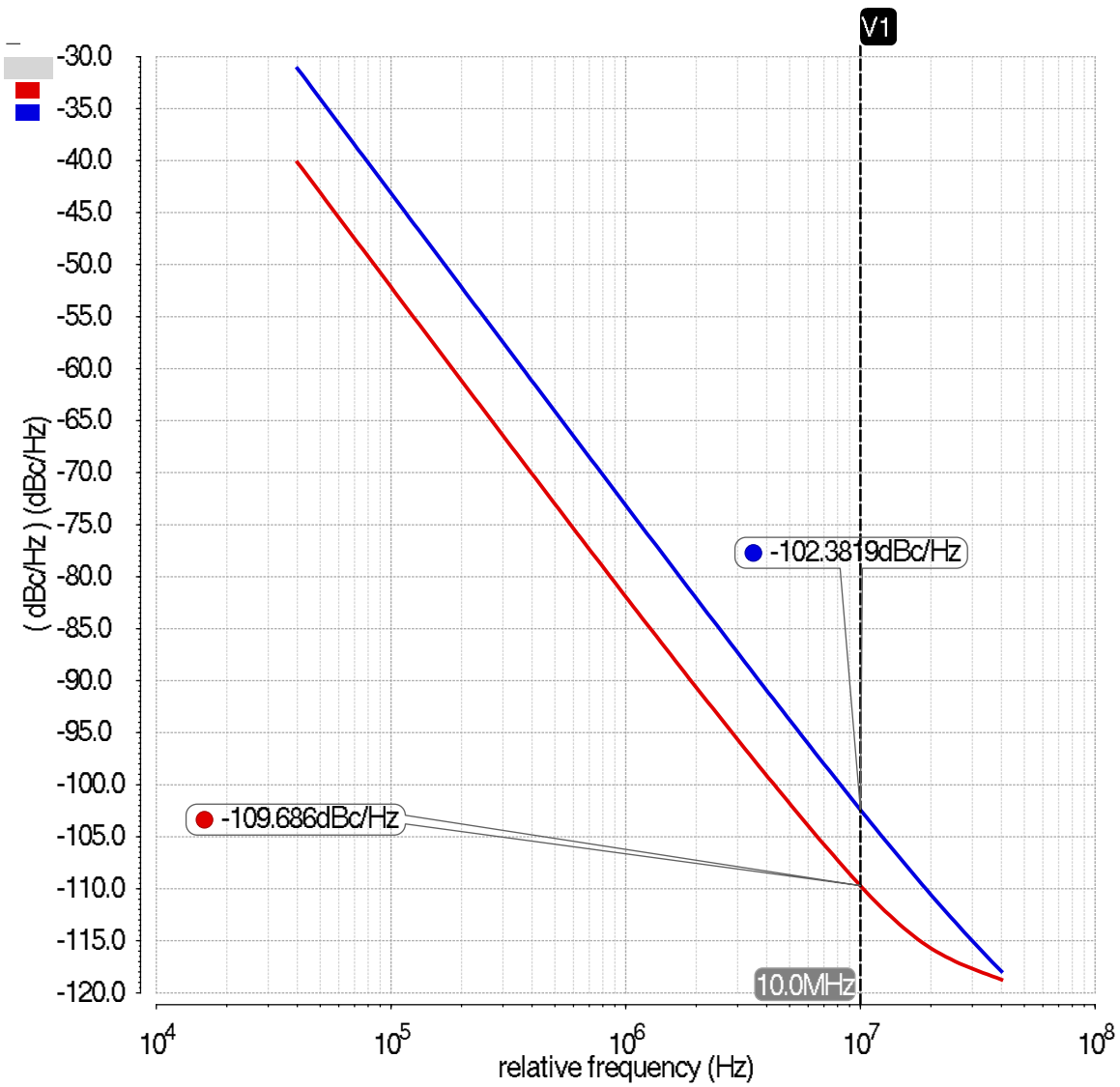

Fig. 4.8: Free-Running VCO Phase Noise at 100 MHz (red) and 700 MHz (blue)

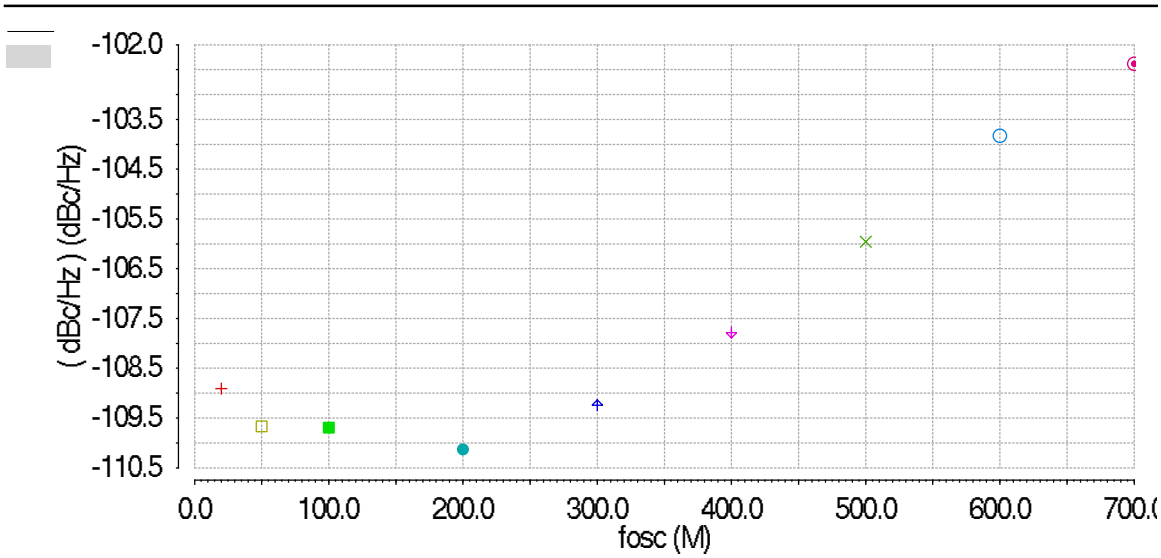

Fig. 4.9: Free-Running VCO Phase Noise at 10 MHz offset vs the oscillation frequency

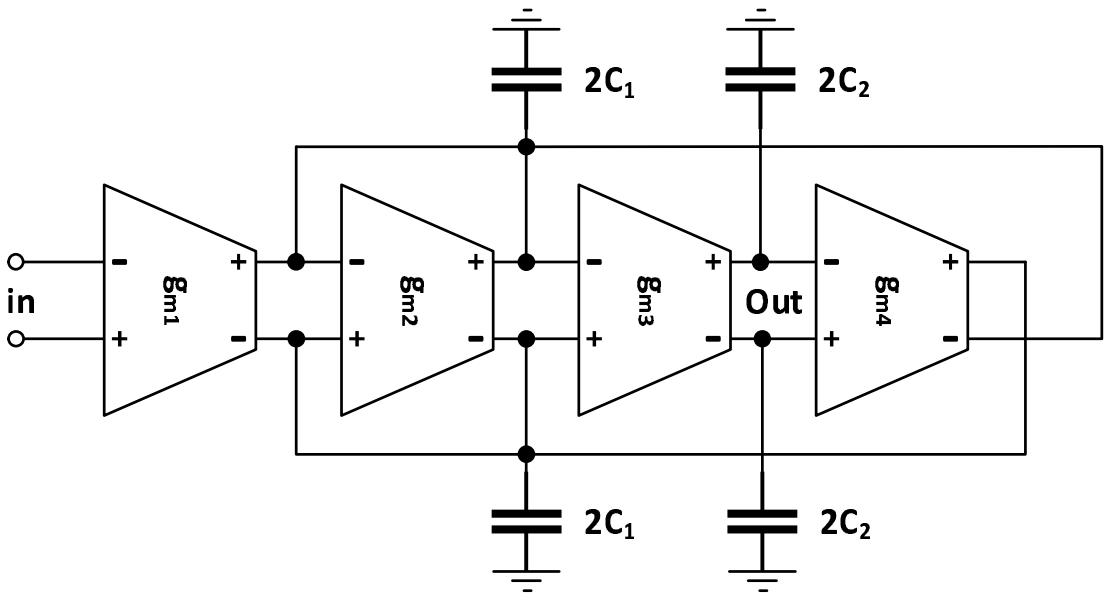

Fig. 4.10: Biquad Stage Block Diagram

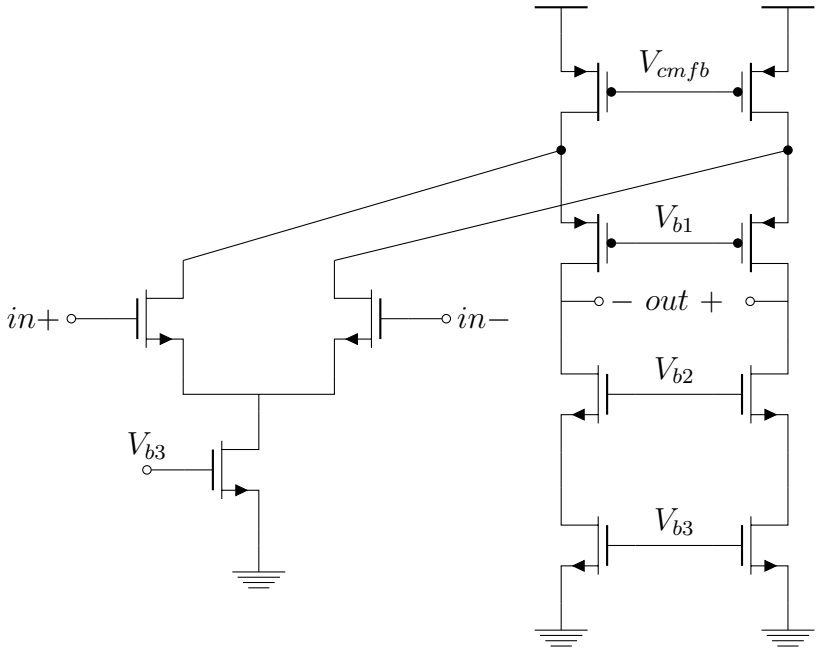

Fig. 4.11: OTA Schematics

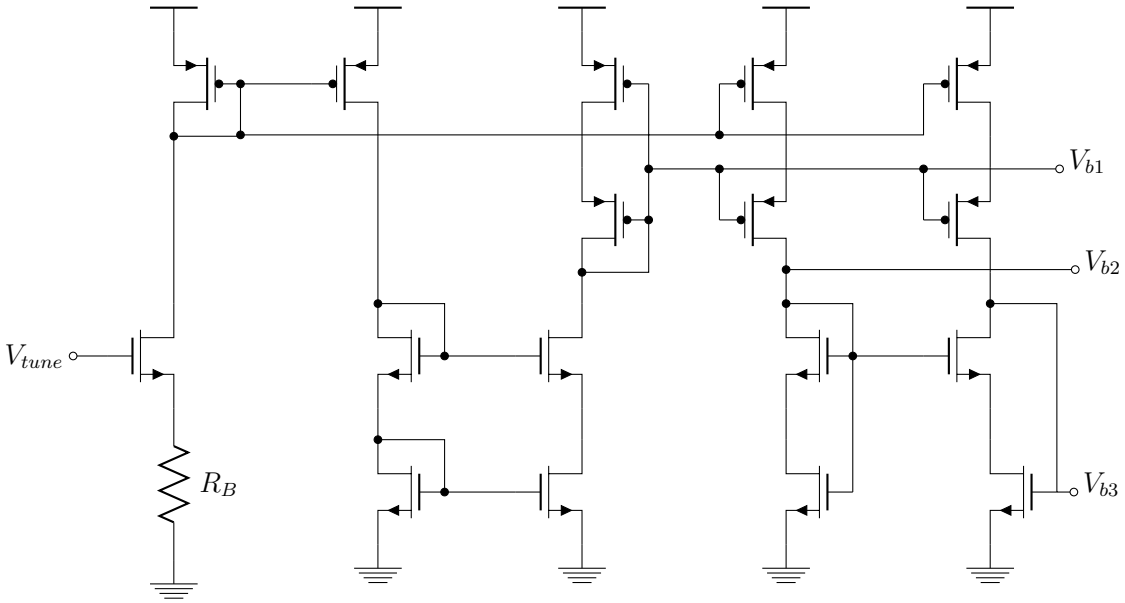

Fig. 4.12: OTA Biasing Circuit

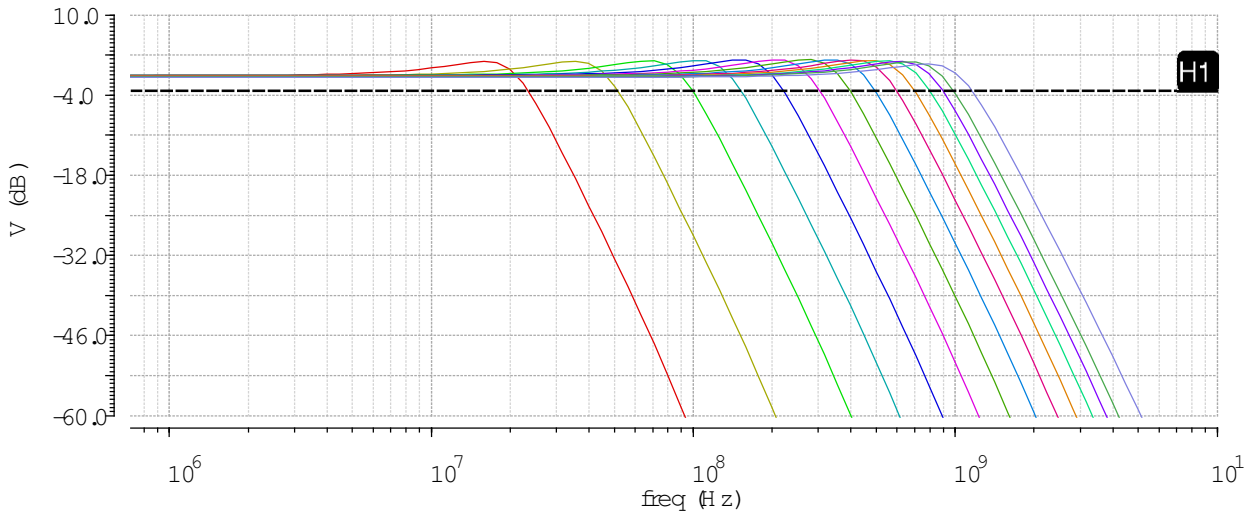

Fig. 4.13: Biquad LPF frequency response for different control voltages

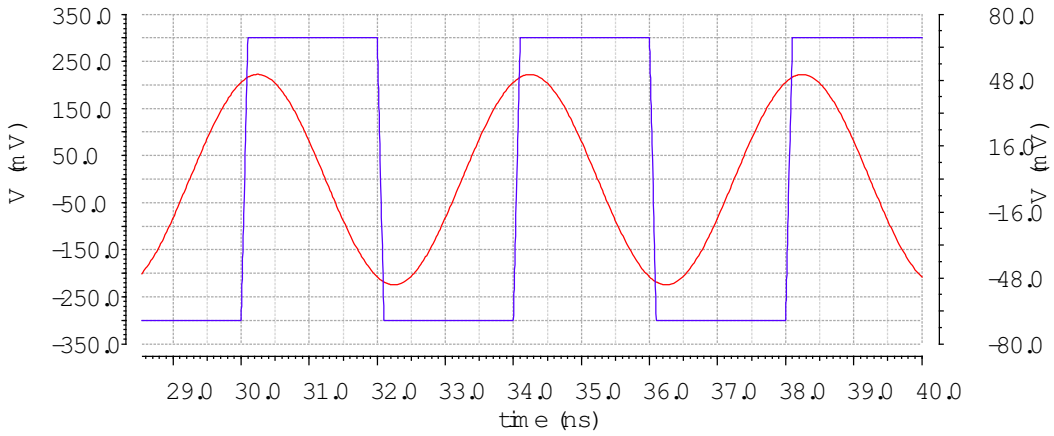

Fig. 4.14: Biquad LPF input(blue) and output(red) waveforms at 250 MHz

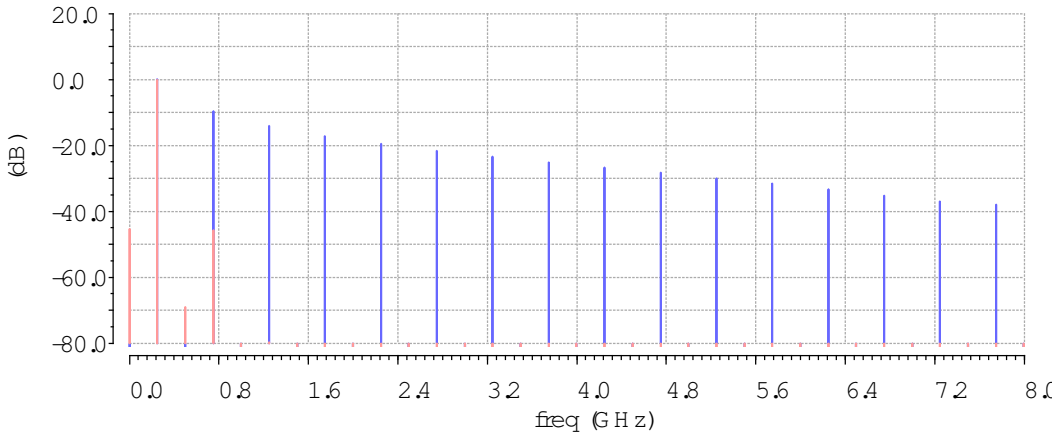

Fig. 4.15: Biquad LPF input(blue) and output(red) normalized frequency content at 250 MHz

Chapter 5

Receiver Front End

An FDPM receiver detects the light traveled through the tissue and, after signal-conditioning, measures the received data – i.e. phase shift and amplitude attenuation – of the received signal compared to the reference signal used for modulating the laser diode. The building blocks of the receiver are photodetector, transimpedance amplifier (TIA), varaiable gain amplifier (VGA), bandpass filter (BPF), phase detector, and amplitude detector. The first four blocks mentioned form the receiver front-end while the rest (phase detector and amplitude detector) are referred to as receiver baseband since they process the information on the down-converted signal. Each of the front-end blocks will be discussed in details in this section. Baseband blocks are covered in Chapter 6.

5.1 Photodetector

As the first block in the receiver, the photodetector has to convert the received light to an electrical current. The choice of the photodetector depends on many factor including but not limited to wavelength, sensitivity, speed, cost and size. The photodetectors available

at the near-infrared range of wavelengths (i.e. $600 - 950$ nm) are silicon photodiodes (Si-PD), silicon avalanche photodiodes (Si-APD) and photo-multiplier tubes (PMT). Table 5.1 compares the commercially available photodetectors at the NIR range [25].

Commercially available photodetectors at NIR			
Type	Si-APD	Si-PD	PMT
Gain	100	1	10^5
Sensitivity Range	nW	μW	fW-nW
Speed	Fastest	Moderate	Fast
Cost	Low-Moderate	Low	High
Quantom Efficiency	40-80%	40-80%	1-40%
Photosensitive Area	Medium	Large	Largest
Size	Small	Small-Medium	Bulky
Operating Voltage	10s to 100s V	few Volts	1000s Volt

Table 5.1: NIR Photodetectors Comparison

It is almost impossible to detect optical power below a μW with Si-PDs due to their low sensitivity. PMTs have the best performance in terms of sensitivity, but they are expensive, bulky, and power hungry (at least 1W); in addition they are not as fast as Si-APDs, and they require a very high dc votage for operation. Si-APDs, although requiring a large (up tp hundreds of volts) dc bias voltage, are the best compromise between performance, size, power, and speed. Therefore the Si-APD is the photodetector of choice for this application. Next we will show the equations governing the operation of an APD and how adjusting its gain can benefit SNR at low optical input levels. Considering the narrowband modulation of laser diode, the received signal at the APD can be represented as:

$$P(t) = P_0(1 + m \times \sin(\omega_0 t)) \tag{5.1}$$

where P_0 is the average optical power incident on APD, $m \in (0, 1]$ is the modulation index, and ω_0 is the angular modulation frequency. If the modulation frequency is within the operating bandwidth of the APD, the current generated in the APD in response to this

incident power is:

$$i_{APD}(t) = M\Re_0 P_0(1 + m \times sin(\omega_0 t)) \tag{5.2}$$

where M is the internal gain of the APD, and $\Re_0$ is the intrinsic responsivity of the photodiode (i.e. when there is no internal multiplication (when $M = 1$)) and is given by:

$$\Re_0 = \frac{\eta q}{h\nu} \tag{5.3}$$

where η is the quantum efficiency, q is the charge of an electron, h is the Planck's constant and ν is the optical frequency of the incident light. In (5.3) the term $\frac{q}{h\nu}$ states that for each photon (having an energy of $h\nu$) absorbed, an electron-hole pair is generated at the APD (having a charge equal to q) and quantum efficiency $\eta(\nu)$ determines what percentage of the incident photons are absorbed and generate electron-hole pairs in the APD. Quantum efficiency is a function of wavelength as well as the material used to fabricate the APD. To calculate the SNR at the APD output we have to calculate the signal power and noise power. The signal power of the modulating current is given by:

$${\sigma_s}^2 = \langle (i_{APD} - \overline{i_{APD}})^2 \rangle = \langle (i_{APD} - MI_p)^2 \rangle = \frac{1}{2}(mMI_p)^2 \tag{5.4}$$

where $I_p = \Re_0 P_0$ is called primary photocurrent.

The noise current consists of the following components:

$$\langle {i_n}^2 \rangle = \langle {i_{sh}}^2 \rangle + \langle {i_{DP}}^2 \rangle + \langle {i_{DS}}^2 \rangle + \langle {i_{TIA}}^2 \rangle \tag{5.5}$$

where i_{sh} is the shot noise of the APD, which is due to the statistical nature of electron generation and collection in presence of light; i_{DP} is the bulk dark current generated due to thermal generation of electron and holes in the bulk; i_{DS} is the surface dark current due to

the surface defects; and i_{TIA} is the input-referred noise current of the TIA. The first three terms can be written as:

$$\begin{aligned}\langle i_{sh}^2 \rangle &= 2qI_pBM^2F(M), \\ \langle i_{DP}^2 \rangle &= 2qI_{DP}BM^2F(M), \\ \langle i_{DS}^2 \rangle &= 2qI_{DS}B.\end{aligned}$$

where I_p, I_{DP}, and I_{DS} are the average primary photocurrent, average dark current in the bulk, and average surface dark current, respectively, and B is the equivalent noise bandwidth of the system. The first two noise currents are multiplied by the gain because they experience the multiplication factor of the APD in the bulk; however the surface dark current does not experience multiplication. The term $F(M)$ is the noise figure of the APD and is generally in the form of M^x where $0 < x < 1$. Considering the noise from the following TIA is white, it can be represented as:

$$\langle {i_{TIA}}^2 \rangle = \frac{4kTB}{R_e} \tag{5.6}$$

where R_e is the equivalent noise resistor for the TIA. Using (5.4) - (5.6), the SNR at the output of APD can be written as:

$$\frac{S}{N} = \frac{\frac{m^2M^2{I_p}^2}{2}}{2qI_pBM^2F(M) + 2qI_{DP}BM^2F(M) + 2qI_{DS}B + \frac{4kTB}{R_e}} \tag{5.7}$$

There exists a value for M that maximizes the SNR. This value of M can easily be calculated

and is given by:

$$M^{2+x} = \frac{2qI_{DS}B + \frac{4kTB}{R_e}}{xq(Ip + I_{DP})} \tag{5.8}$$

As shown in (5.8), the optimum M is independent of modulation index (m) and bandwidth and depends only on noise parameters of the system (i.e. surface and bulk dark current and noise factor of the APD and noise of the TIA) and input signal strength I_p. By substituting (5.8) in (5.7) and equating $SNR = 1$, the best achievable sensitivity of the system given the noise parameters of the APD and the noise contribution of the following circuitry can be calculated. The two equations are coupled together and there is no simple closed-form solution for I_p. However in most practical cases:

$$\begin{aligned} 2qI_{DS} &\ll \frac{4kT}{R_e}, \\ I_{DP} &\ll I_p. \end{aligned}$$

With these approximations the best achievable sensitivity can be approximated as:

$$I_{psens} = \frac{2}{m^2}(xq)^{\frac{2}{2+2x}} \times (\frac{4kT}{R_e})^{\frac{x}{2+2x}} \times \Big((1 + \frac{2}{x})B\Big)^{\frac{2+x}{2+2x}} \tag{5.9}$$

As an example, considering the use of Hamamatsu S12051 Si-APD with $\lambda = 800$nm [26], the following parameters can be extracted from its data sheet:

$$
\begin{aligned}
M &= 100, \\
x &= 0.3, \\
I_D &= 0.1 \text{ nA (Typ.) at } M = 100, \\
f_c &= 900 \text{ MHz for } \mathrm{R_L} = 50\ \Omega, \\
\Re_0 &= 0.5.
\end{aligned}
$$

Assuming the noise of the TIA and its following circuitry can be represented with a noise resistor of 1.5 kΩ, the best achievable sensitivity of the system in terms of primary current I_p can be calculated from (5.9) and is approximately 3.1 nA, which is equivalent to an optical power sensitivity of 6.2 nW. However the required gain (M) for this sensitivity is too large to be realized (more than 10^6), and even if such a gain can be reached, it is almost impossible to maintain such a large gain in APD across temperature and voltage variations. For this reason, to achieve nW range of sensitivity with acceptable values of M additional filtering is required which is discussed later in the chapter.

5.2 TIA

A transimpedance amplifier (TIA) is the first block on the chip and follows the photodetector. Therefore it has to provide enough gain to suppress the noise of the following circuitry, while its noise performance determines the sensitivity of the receiver. The commercial Si-APDs discussed earlier usually have a big capacitor with a value ranging from hundreds of fF to a few pF depending on their photosensitive area [26]. Therefore the designed TIA should have a

low input resistance to allow the bandwidth of the system to accommodate operation up to 1 GHz. Among the known CMOS TIA architectures, the regulated cascode (RGC) architecture is a good compromise between the low input resistance of op-amp based architectures and simplicity and low-noise performance of single-transistor TIAs [27]. The schematic of the TIA input stage is shown in Fig. 5.1. The input resistance (R_{in}) and transimpedance gain ($R_T = \frac{v_{out}}{i_{in}}$) at low frequencies can be calculated as:

$$R_{in} \approx \frac{1}{g_{m1}(1 + g_{mB}R_B)}. \tag{5.10}$$

$$R_T \approx R_1. \tag{5.11}$$

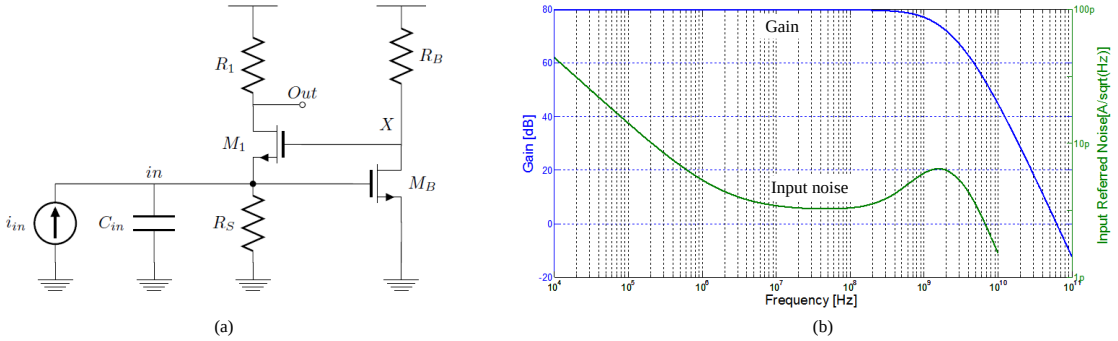

Fig. 5.1: (a) Regulated cascode transimpedance amplifier; (b) simulated gain and input-referred spot noise.

In Fig. 5.1, there is a tight trade-off in choosing the value of R_1. It is desirable to increase the value of R_1 in order to increase the gain and reduce the noise contribution of R_1 and the following stages. However R_1 has a limited voltage headroom, and increasing its value corresponds to a lower bias current for M_1, which in turn increases the input resistance and decreases the bandwidth. In addition, due to the large input capacitor there is a dominant pole at the input node; increasing the value of R_1 will reduce the output pole frequency, and

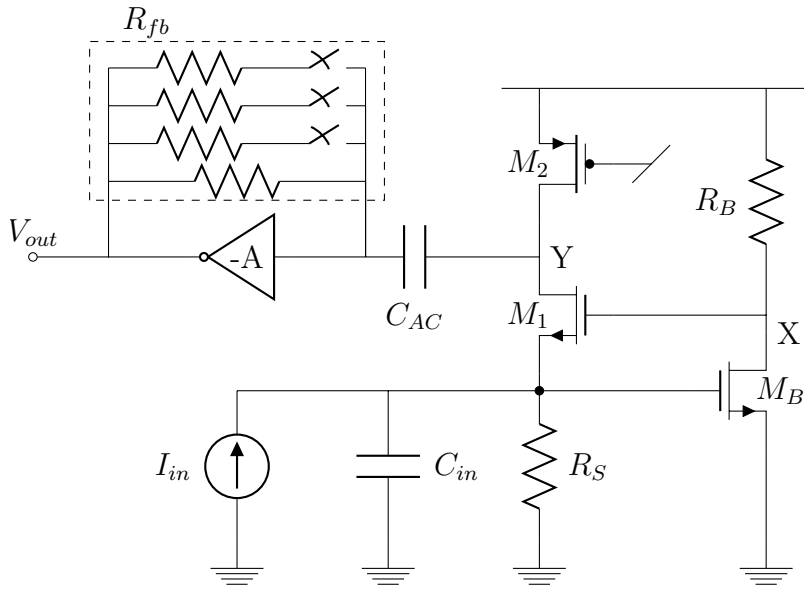

Fig. 5.2: TIA schematic

can compromise the stability of the TIA. Large R_1 can also mean large swing at the output node, which forces M_1 to enter the triode region during part of the signal swing, reducing the linearity of the system. In order to relax this design trade-off, usually a simple feedback TIA follows this stage as shown in Fig. 5.2. The use of this additional stage lowers the total resistance seen at node Y and also allows for gain adjustment by utilizing a resistor bank for the feedback resistor. In the Fig. 5.2, the inverting gain stage is realized by a simple CMOS inverter. The two stages are ac-coupled using a large on-chip metal-oxide-metal (MOM) capacitor to separate their biasing. In order to achieve a more robust biasing and increase the value of R_1 with the limited voltage headroom it has been replaced with an active load (M_2) which is replica biased. The output resistance of the M_2 does not control the gain as long as it is large compared to the input resistance of the feedback TIA (i.e. $\frac{R_{fb}}{1+A}$) and it does not have to be carefully controlled. Since in the new architecture the resistance at node Y is reduced, there would be a limited swing at this node and non-linearity of the transistors are negligible. Also, the decreased resistance improves the stability by pushing the second pole to higher frequencies. The input resistance is similar to (5.10), and the transimpedance

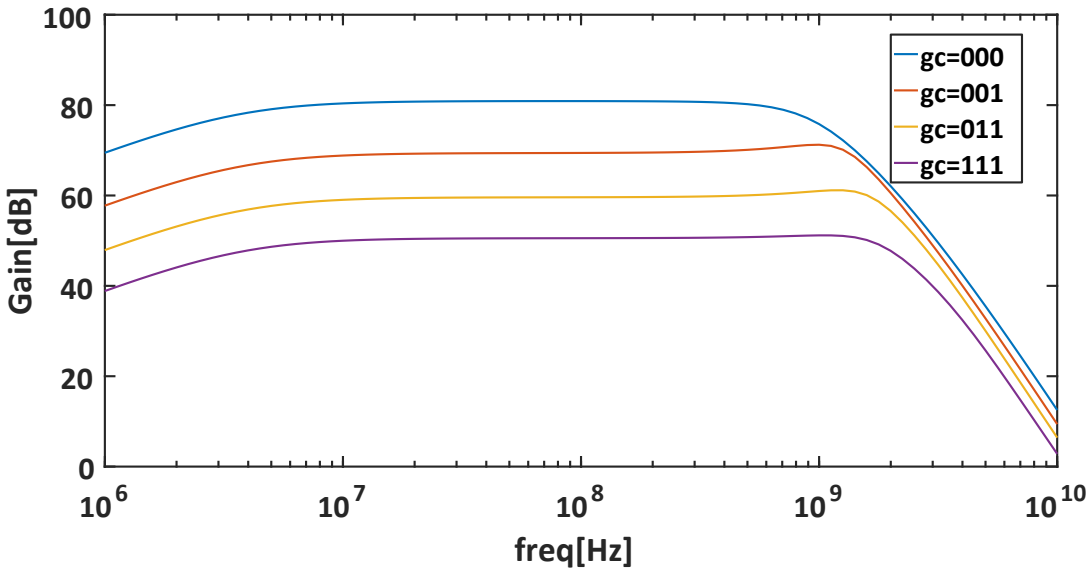

Fig. 5.3: TIA gain for different gain settings.

gain is equal to R_{fb}, the value of the resistor tank which is adjusted by three MOS switches which themselves are controlled by decoding two external control bits. Fig. 5.3 illustrates the TIA frequency response vs. gain control bits. Fig. 5.4 shows the input-referred current spot noise of the TIA for the highest gain setting ($R_{fb} = 10$ kΩ).

5.3 VGA

In order to attain the wide dynamic range and low sensitivity required for the FDPM system, additional gain is required following the TIA to bring the detected signal level to appropriate levels for amplitude and phase measurement. Thus a VGA follows the TIA with a variable gain between 8 dB and 32 dB that can be adjusted by two external control bits in 8 dB steps.

The block diagram of the VGA is shown in Fig. 5.5. It includes a low-pass RC filter at its input, which provides equal dc voltages at the differential inputs of the VGA for proper single-ended to differential conversion. It also includes an offset-cancellation feedback loop

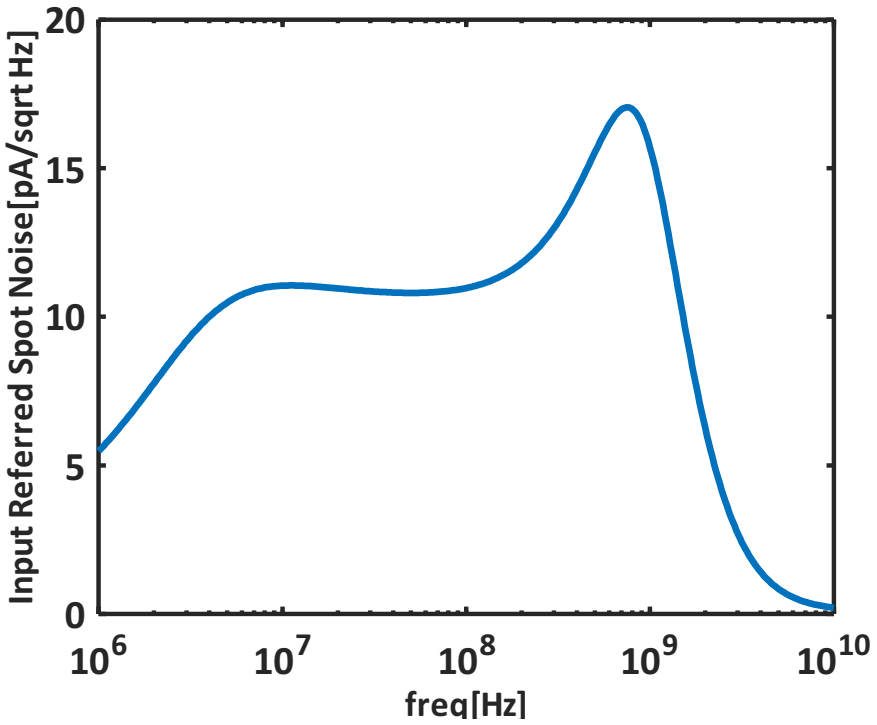

Fig. 5.4: Input-referred current spot noise of the TIA for the highest gain setting.

formed by a low-pass filter and a feedback gain stage. The offset cancellation loop is part of the designed VGA's first stage, and three similar gain stages follow this stage in the VGA. The schematic of the first stage is illustrated in Fig. 5.7. The schematic of each gain stage is shown in Fig. 5.8. Each stage has a control bit that sets its gain to either 0 or 8 dB. At low gain settings all three gain stages are set to their low-gain mode. As the gain requirements increase, the last stage will be switched into high-gain mode. To increase the gain further, more stages toward the end of the path will be turned on. The value of gain control settings for each gain configuration are shown in Table 5.2. This configuration results in worse input-referred noise but better linearity for the VGA. Since enough gain is provided by the TIA to suppress the noise of the VGA, this gain configuration is chosen to achieve better linearity for large input amplitudes. Fig. 5.6 shows the frequency response of the VGA for different gain settings.

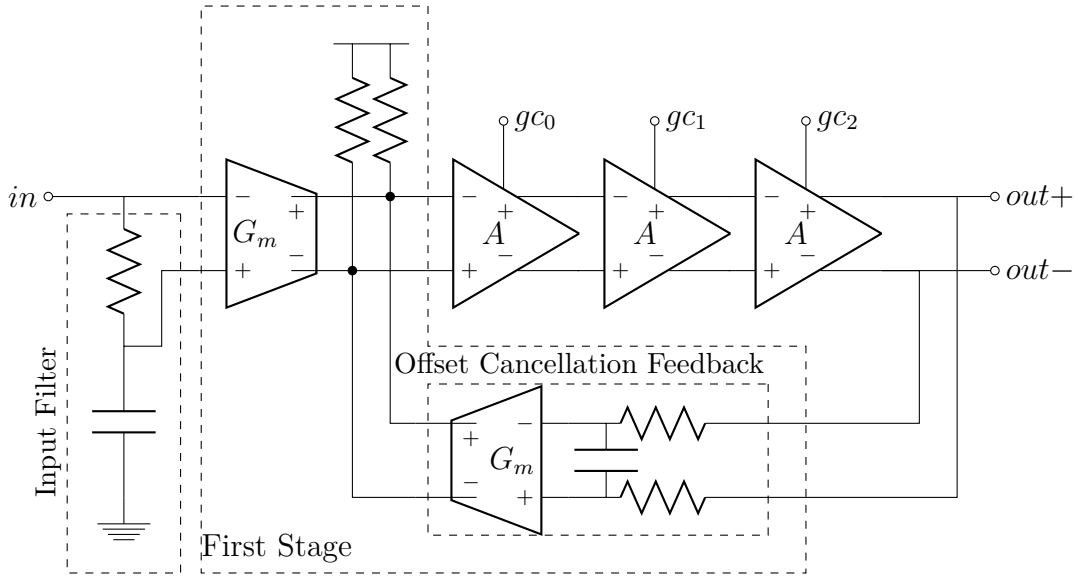

Fig. 5.5: VGA Block Diagram

Gain (dB)	gc_0	gc_1	gc_2
8 dB	0	0	0
16 dB	0	0	1
24 dB	0	1	1
32 dB	1	1	1

Table 5.2: Gain Settings for the VGA

5.4 N-path Filter

Since the modulation of the optical signal is a single tone, a highly selective bandpass filter can be used to filter the noise and improve the sensitivity of the receiver. A conventional analog bandpass filter raises challenges in precisely matching its center frequency with the generated modulation frequency. As an alternative, we will design the bandpass filter using the "N-path filter" technique. As described in [28], this technique allows for setting the filter center frequency at exactly the desired value as long as there is a clock signal available. Although such filters are typically used for wireless communications circuits, their characteristics are nearly ideal for this application. In addition to their high frequency selectivity,

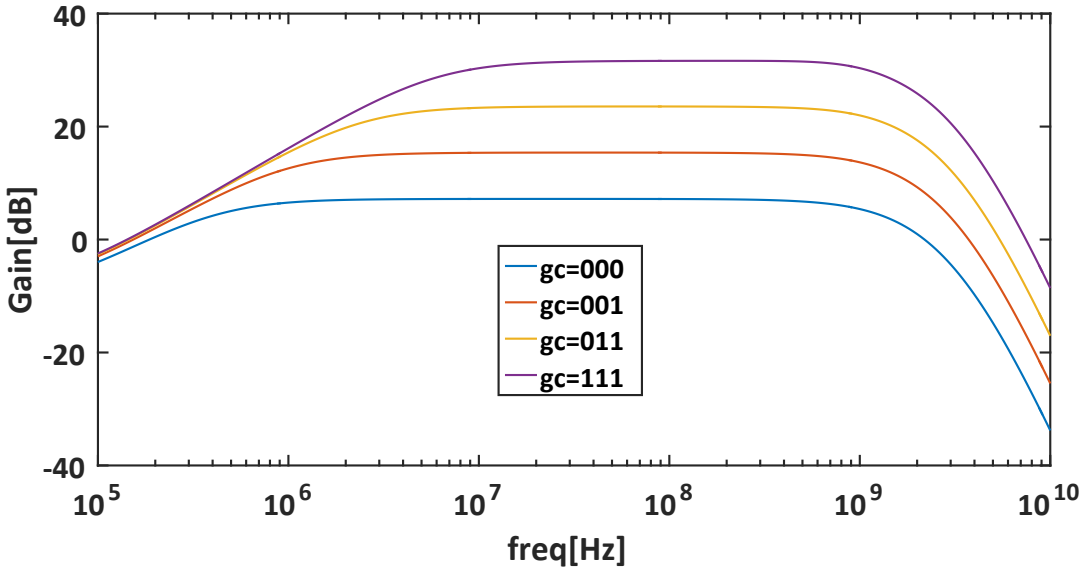

Fig. 5.6: VGA gain for different gain settings.

their center frequency is set by the frequency of the multi-phase clock signal applied to it. Therefore if the same signal generator that generates the input signal also generates the multi-phase clock signals for the filter, it is assured that the detected signal is always within the passband of the filter and therefore no extra circuitry is required to fine-tune the filter.

The schematic of a differential 4-path filter is shown in Fig. 5.9(a). Its operation requires the four non-overlapping clock phases shown in Fig. 5.9(b), realized by the circuit shown in Fig. 5.9(c), which requires two quadrature input signals for its operation. In this circuit, NMOS switches connect capacitor C_{f0} to V_{out} for the first clock phase ck0; at the next clock phase ck90, capacitor C_{f1} is connected to V_{out}. During the next two phases (ck180 and ck270) the process is repeated, but with the connections to V_{out} inverted. Therefore if V_{in} and the clock have the same frequency, the filter capacitors will always experience the same portion of the input waveform, the charge will accumulate on the capacitors, and the output voltage V_{out} will be a sampled version of the input signal. Any input signal components that are different from the clock frequency, including noise, will be attenuated since the average charge across the capacitors will be close to zero over multiple cycles of clock.

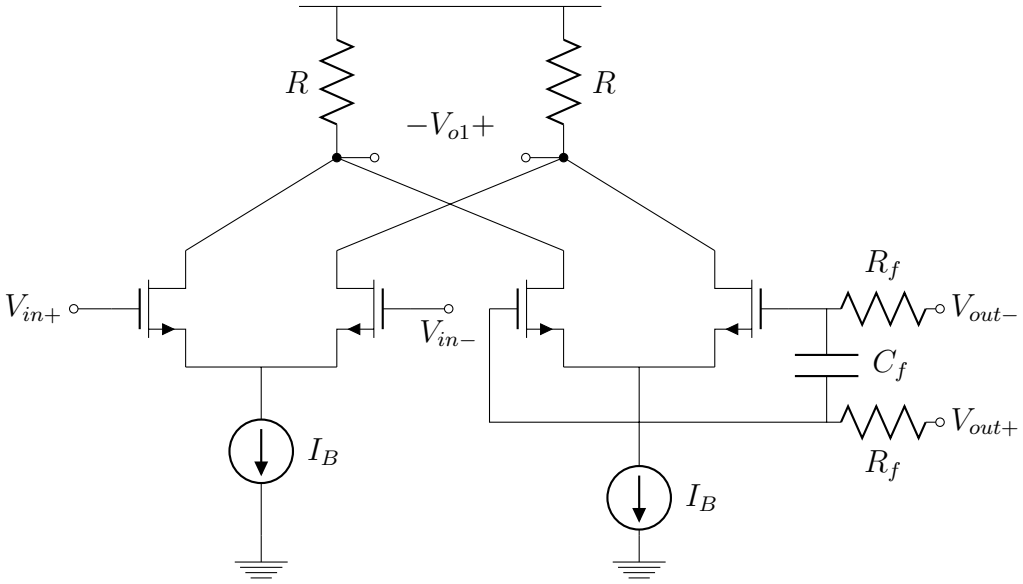

Fig. 5.7: VGA input stage

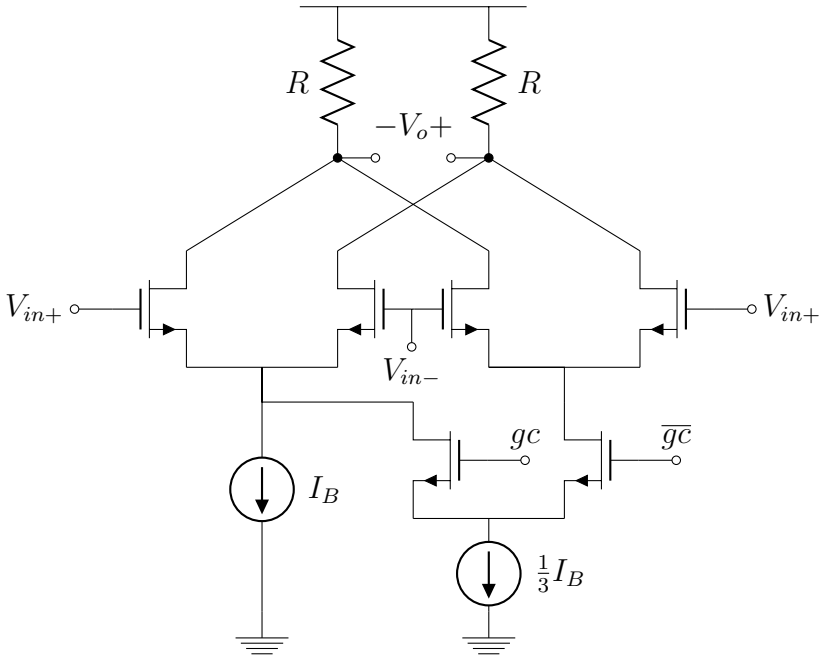

Fig. 5.8: VGA gain stage

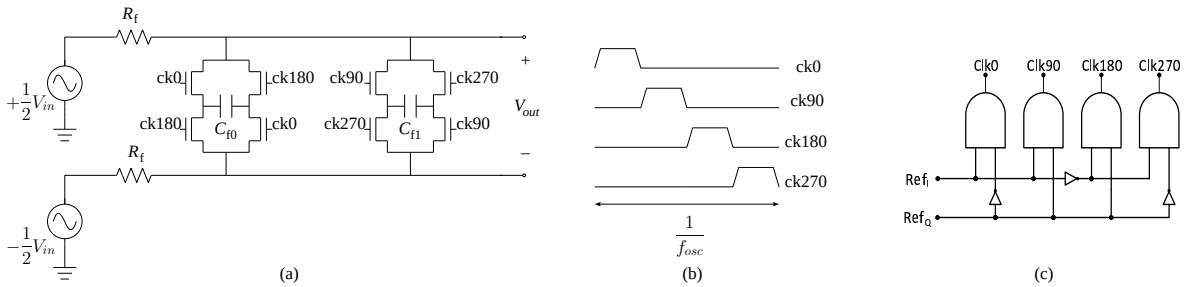

Fig. 5.9: Differential four-path filter: (a) schematic; (b) multiphase clock signals; (c) four-phase non-overlapping clock generator.

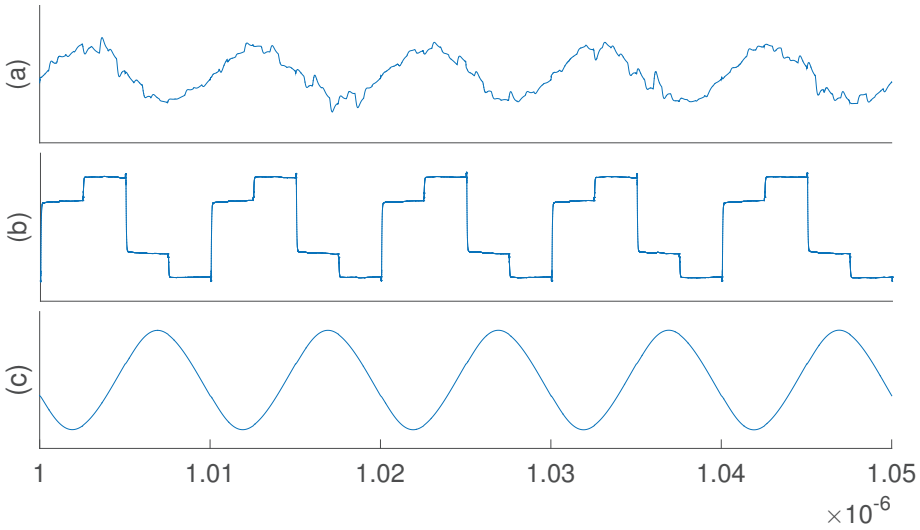

Fig. 5.10: 4-path filter waveforms: (a) input; (b) output; (c) output after LPF.

In order to achieve the required filtering, two or more of these N-path filters can be combined to make higher-order filters as described in [29]. Transient simulation results of the input and output of a 4th-order 4-path filter are shown in Fig. 5.10(a) and (b), respectively, where white noise has been superimposed on the input 100 MHz sine wave. It can be observed that use of this sampled-data filter creates harmonics at the output signal. In the differential architecture, the even-order harmonics are suppressed due to the symmetry but the odd-order harmonics remain. Therefore a lowpass filter is necessary to suppress the higher harmonics. Fig. 5.10(c) shows the output of the 4-path filter after passing through a second-order lowpass active filter that effectively removes the higher-order harmonics from the waveform.

The frequency response of the bandpass filter is shown in Fig. 5.11. The quality factor of

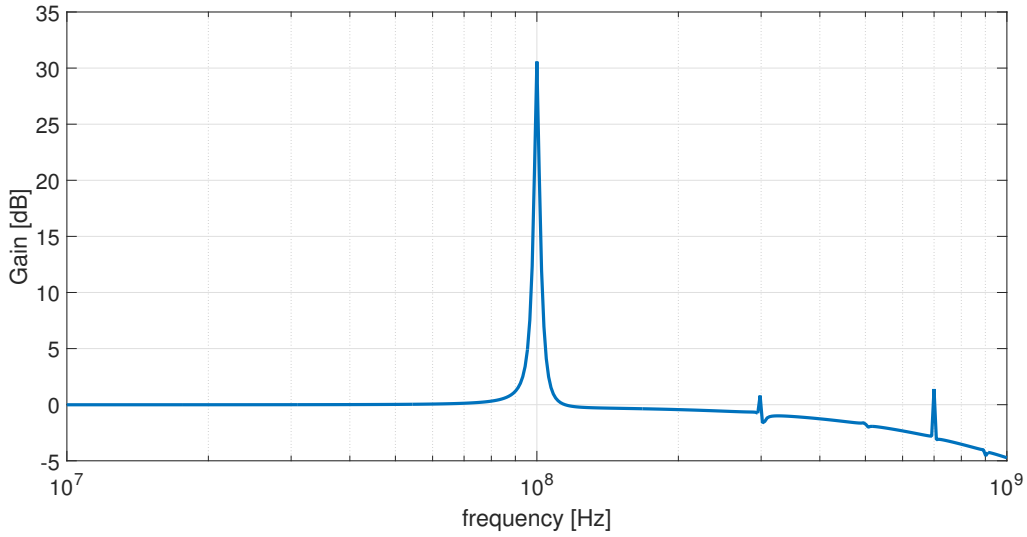

Fig. 5.11: 4-path filter frequency response.

this filter is about 70 and the effective bandwidth is 1.5 MHz around the 100 MHz center frequency.

5.5 Performance Simulations

In this section the simulation results for the receiver front-end are presented and the details are discussed. The input of the receiver chain is the current generated by the APD and the output is at the output of the N-path filter. Since the N-path filter is clocked by periodic waveforms, Periodic Steady-State (PSS), PAC, and PNoise simulations are performed to simulate the frequency response and noise performance of the complete receiver front-end.

Fig. 5.12 shows the frequency response of the front-end for highest and lowest gain settings in the chain. Fig. 5.13 shows the output noise of the front-end for the highest gain settings (worst-case), corresponding to the signal being at its lowest amplitude and the SNR at its lowest. For lower gain settings, although input-referred noise will increase, the SNR will improve, making its noise performance less critical. Total integrated noise at the input of the TIA is 40 nA_{rms}. With the internal gain of the APD set to 100, based on the Hamamatsu

S12023 series Si-APD datasheet, this current sensitivity translates into an optical sensitivity of better than 1.6 nW_{rms} for any wavelength between 600-950 nm.

The linearity of this system is not very critical since we can always reduce the input power by adjusting the laser diode current in case the received signal is too strong.

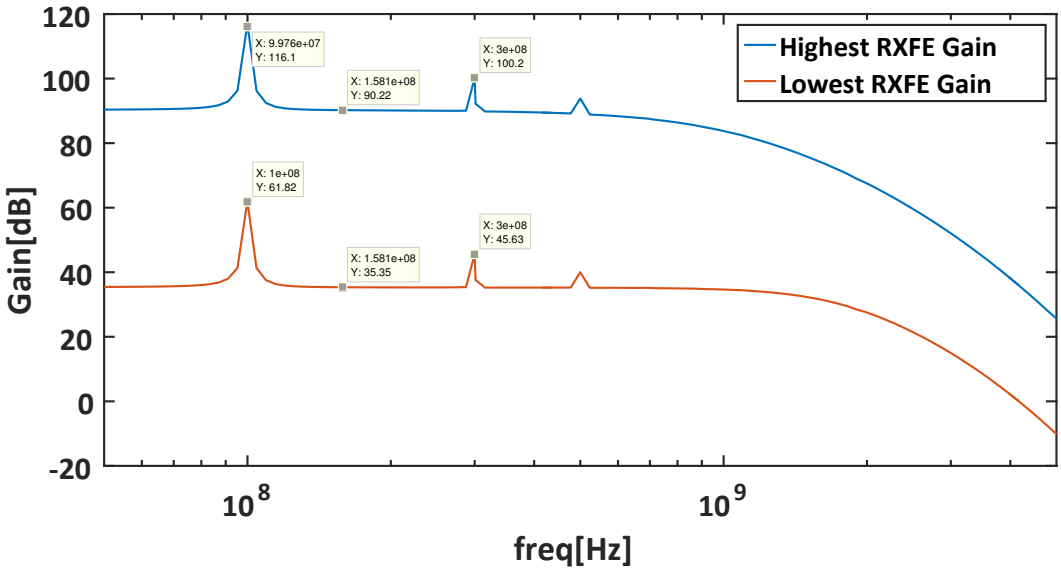

Fig. 5.12: RXFE gain for highest- and lowest-gain modes.

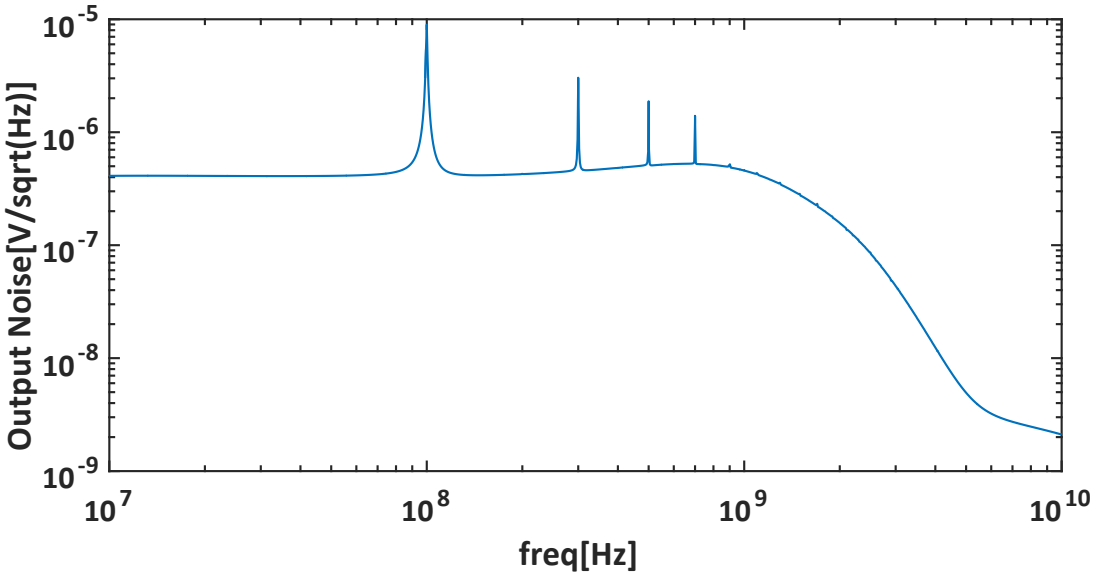

Fig. 5.13: Pnoise Simulation for the highest-gain mode.

Chapter 6

Receiver Baseband

Following the receiver front-end, the baseband signal at the output of the N-path filter can be used for further processing; however an N-path filter is essentially a multi-phase mixer with the subtle difference of where the output is taken. In this design the output of the N-path filter is monitored for testing the quality of the signal. At the same time the baseband voltage on the capacitors of such a filter can be used for processing of the data. In this sense the N-path filter acts like a down-conversion mixer and the receiver acts like a homodyne receiver with direct conversion of the output to zero frequency. The baseband process is implemented in the analog domain which directly measures the phase shift and amplitude of the received signal. These measured values can be probed with an oscilloscope during the testing of the chip and can be digitized by the ADC of the micro-controller for post-processing of the data. The two parts of the receiver baseband – the Phase Measurement Unit and the Amplitude Measurement unit – are described next.

6.1 Phase Measurement Unit

In FDPM, the received optical signal strength emanating from the tissue under test can change orders of magnitude, depending on the separation between the light source and the photo-detector as well as the modulation frequency. Conventional phase detectors are usually based on XOR (or XNOR) operation. XOR gates are logic gates and require amplitude-limited square waves for proper operation. Therefore, in a conventional phase detector usually a multi-stage limiting amplifier is used to amplify the received signal to an amplitude-limited square wave.

The large-signal and small-signal delay of gain stages are generally different because the former is determined by the slew-rate behavior of the stage, while the latter is a function of the RC time constant of the stage. For a higher input amplitude more of the stages will show large-signal behavior; thus the delay would change with input amplitude. This makes it difficult to design a limiting amplifier with fixed delay over the multiple-decade range of input amplitudes that is needed for this application. Moreover, limiting amplifiers, typically consisting of four to six gain stages, are very power hungry. To alleviate these issues, a new phase detection approach based on the N-path filter is introduced that decreases the power consumption significantly and introduces negligible error over 40 dB variation in input amplitude. This two-decade range does not eliminate the need for gain adjustment in the TIA and VGA, but considerably simplifies it since there is no longer a need for fine gain-tuning, which can become complex over PVT variations.

6.1.1 Behavior of N-path Filter

The low-amplitude detected signal requires high-Q filtering to reduce the superimposed noise before its amplitude and phase can be measured. This system is designed to operate over

the frequency range of 100 MHz to 1 GHz. Since a clock signal is readily available, an N-path filter is a viable option due to its high Q and center frequency adjustability [28]. Moreover, the voltage stored on the capacitors of the N-path filter can be used to generate a square-wave signal in phase with the detected signal, and the voltages on these capacitors gives precise information about the phase difference between the clock and input signals. An example of a 4-path filter is shown in Fig. 6.1(a), where the switches turn on sequentially and connect each corresponding capacitor to the output node for a quarter of the clock period. If the input frequency is a multiple of the switching clock, then each time a switch turns on its corresponding capacitor experiences the same portion of the sine wave and over time its voltage converges to the average voltage of that portion. Otherwise each capacitor experiences a different portion of the sine wave each cycle and over a long time the average voltage on the cap will not reach a constant value, making the output an attenuated version of the input. The farther the input frequency is from a multiple of the switching frequency, the higher the attenuation will be. As described in [28], it is this behavior that results in a bandpass filter characteristic with a center frequency identical to the clock frequency.

For the case where the the input and clock frequencies are identical, the phase difference between them can be measured by observing the steady-state voltage on each of the capacitors as illustrated in Fig. 6.1(c). In this figure the steady-state voltages on each of the four capacitors are shown for three different phase differences. The difference between the voltages across C_{90} and C_0 vs. input phase difference is shown in Fig. 6.1(b), and it is this characteristic that is exploited in designing a precise phase detector.

6.1.2 Proposed Architecture

The architecture of the proposed phase detector [30] is illustrated in Fig. 6.2(a). The signal generator, based on a four-stage ring oscillator, provides four quadrature clock signals *ref0*,

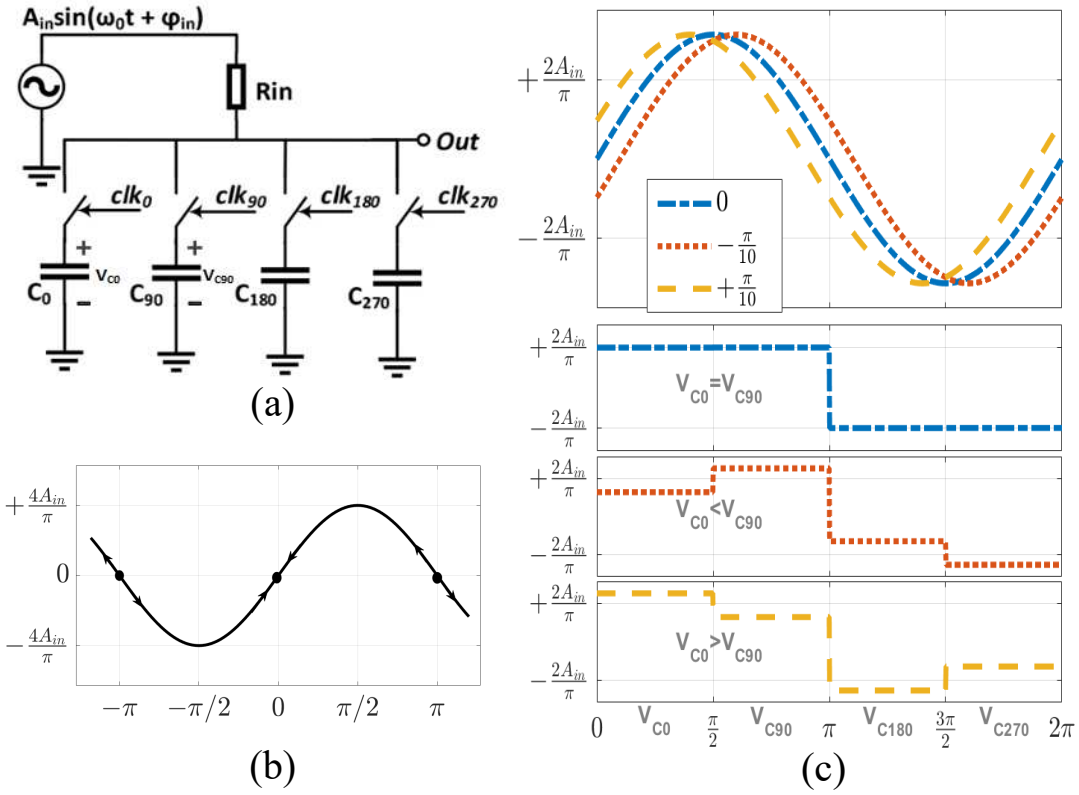

Fig. 6.1: (a) Simplified schematic showing behavior of 4-path filter; (b) characteristic showing average voltage difference across C90 and C0 ($V_{C0} - V_{C90}$) vs. phase shift; (c) illustration of steady-state output (bottom three) for input (top) and clock (not shown) signals of identical frequency but with different phase difference.

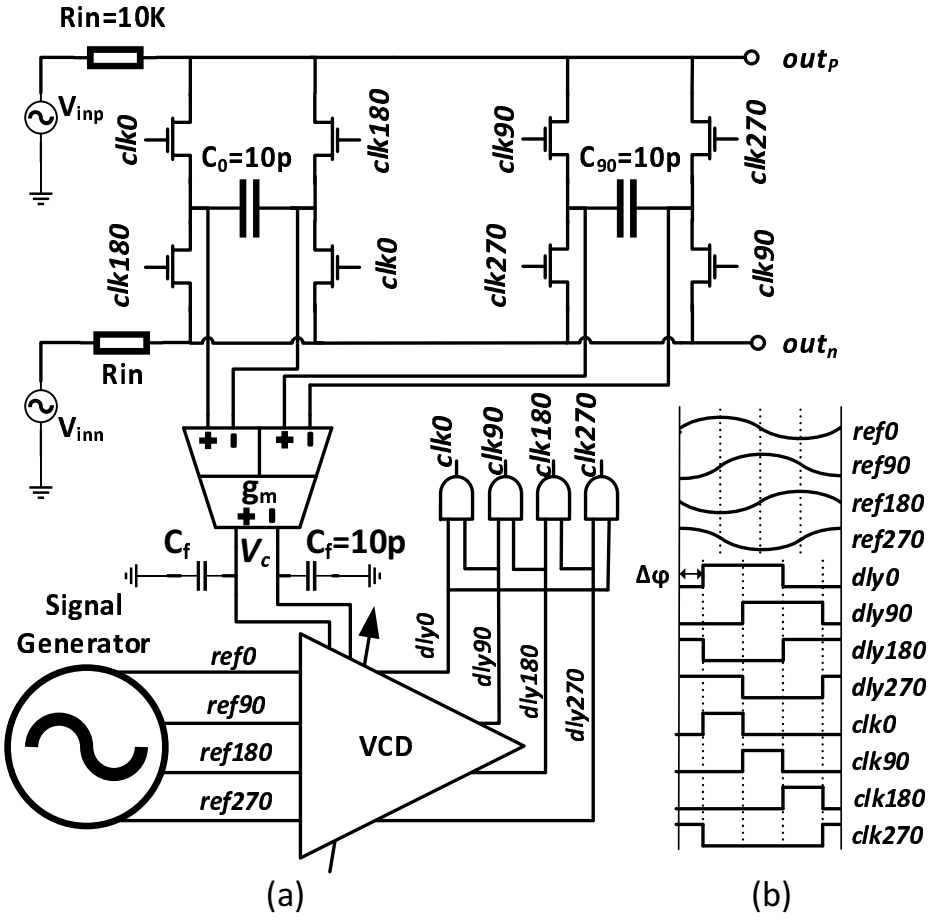

Fig. 6.2: (a) Proposed system diagram; and its (b) Clock and pulse signals.

ref90, *ref180*, and *ref270*, all with 200 mV amplitude. The signal *ref0* is also used to drive the modulation of the laser that is applied to the tissue under test. These four clock signals are applied to a variable delay circuit, whose delay is controlled by differential voltage V_C; its output signals *dly0*, *dly90*, *dly180*, and *dly270*, which have rail-to-rail swings, are then applied to a set of AND gates in order to generate four non-overlapping clock pulses *clk0*, *clk90*, *clk180*, and *clk270* that are applied to the NMOS switches of the 4-path filter. Here a differential 4-path filter, consisting of two capacitors and eight switches, is implemented to suppress even-order harmonics.

The clock and pulse signals are shown in Fig. 6.2(b). The input signal V_{in} is derived from the modulated light emanating from the tissue. The feedback portion of the circuit consists of the differential difference transconductance block, capacitor C_f, and the differential control voltage V_C of the variable delay circuit. The action of the feedback loop is to bring the average difference between the two pairs of input voltages of the transconductance block to zero, which occurs when the average voltages across capacitors C_0 and C_{90} are the same. As illustrated in Fig. 6.1(b), this can happen only when the phase difference between the input and delayed clock waveforms is either 0° or 180°. However, it can be shown that the only stable equilibrium corresponds to 0° phase difference. Given this condition at equilibrium, the phase difference between *ref0* and $V_{inp/n}$ must be the same as that between *ref0* and *clk0*. Furthermore, if the relationship between control voltage V_C and the delay of the voltage-controlled delay cell (VCD) is known, then V_C will provide a precise measurement of this phase shift.

We now consider the dynamics of the Fig. 6.2 feedback circuit. Assuming that the 4-path filter operates in its linear region and that $R_{in} \times C_{0,90} \gg T_{in}$, where T_{in} is the period of the

input and clock signals, the closed-loop transfer function after the loop is locked is given by:

$$\frac{\phi_{clk}(s)}{\phi_{in}(s)} = \frac{1}{1+s\tau}$$
$$\text{where } \tau \equiv \frac{\pi}{4} \cdot \frac{C_f}{g_m K_{VCD} A_{in}} \tag{6.1}$$

In (6.1), K_{VCD} is the coefficient of the voltage-controlled delay cell around the lock point with units of rad/V; g_m is the transconductance value; C_f is the integration capacitance at the output of the transconductance block; and A_{in} is the amplitude of V_{in}. This first-order approximation is accurate as long as $\tau \gg R_{in} \times C_{0,90}$. Note that the expression for τ indicates that the loop dynamics are slower for lower input signal amplitudes. This is an inherent advantage of this design, since signals with lower amplitude suffer more from the noise and more filtering of the phase noise is desirable. However this comes at the cost of longer locking times. In addition, nonidealities – e.g., input-referred offset of the transconductance block and the delay of the AND-gates that are used to generate non-overlapping clock signals – will introduce deterministic errors that should be removed by means of calibration elsewhere in the system. Although the delay of the AND-gates can always be compensated, the input-referred offset of the g_m cell becomes problematic if the input amplitude becomes comparable to this offset voltage. Therefore a switched-capacitor offset cancellation feedback loop is implemented, which is discussed later in this section.

Delay Cell

As shown in Fig. 6.3, the voltage-controlled delay cell (VCD) takes as inputs the four phases of the clock signals generated by a quadrature oscillator and provides four outputs that are delayed versions of each of the inputs. The delay, which can vary over an entire clock period, is set by the differential control voltage $V_{C+} - V_{C-}$.

The delay cell is based on the interpolating circuit shown in Fig. 6.3(a). This circuit will have

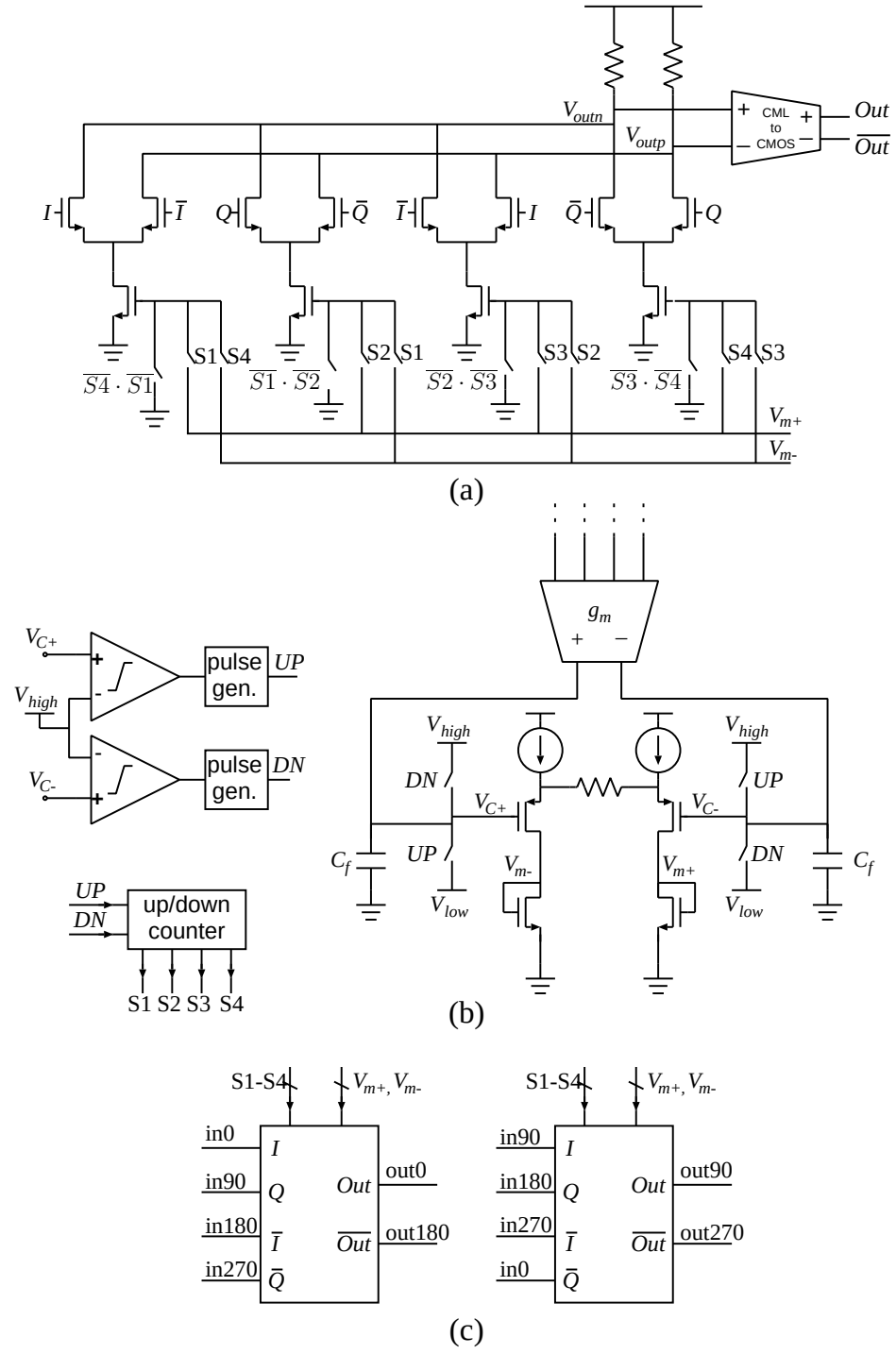

Fig. 6.3: (a) Interpolating cell; (b) Biasing and control circuitry; (c) VCD block diagram.

at any given time two switches closed, corresponding to two of the differential pairs turned on, with the other two turned off. For the two differential pairs that are turned on, the tail currents are set by the circuit shown in Fig. 6.3(b). The output phase of the Fig. 6.3(a) circuit is an interpolation between the phases of the inputs of the two differential pairs that are turned on. For example, if S1 is closed and all other switches are open, the phase of the output will be interpolated between the phases of the I and Q signals, according to the value of $V_{C+} - V_{C-}$. In particular, this switch setting allows for phases between 0° and 90° relative to the I input. Likewise, closing switch S2 allows for phases between 90° and 180°; closing switch S3 allows for phases between 180° and 270°; and closing switch S4 allows for phases between 270° and 360°. In this way, by appropriate selection of the switches and $V_{C+} - V_{C-}$ any delay between the I input and Out output over a full clock cycle can be achieved.

In order to provide four phases of the output, two of the Fig. 6.3(a) interpolating blocks are implemented as shown in Fig. 6.3(c).

g_m Cell

The differential difference transconductance block used in the design of the gm-C integrator is shown in Fig. 6.4. The currents conducted through the diode-connected transistors are proportional to the input difference. These currents are mirrored to the outputs, which are used to charge the capacitors at the output nodes. The transistors of the output stage are designed with length of 1 μm for higher output resistance. The OTA consumes 80 μA, has a gain of 80 dB, and a 3-dB bandwidth of 320 Hz with an integrating capacitor of 10 pF.

Since this circuit is a fully differential block, common-mode feedback is required in order to set up the bias voltages at the output nodes. As mentioned earlier, offset cancellation is necessary to improve the accuracy of the loop for small input signals. Auto-zeroing technique is utilized in the gm cell to cancel the offset. Common-mode feedback and autozeroing

operation are implemented in a feedback loop as shown in Fig. 6.5. The offset cancellation can be enabled or disabled by a control bit. When offset cancellation is enabled, the feedback loop is clocked with a pulse train that resets the offset before each measurement. During the reset phase all the N-path switches turn on to connect the inputs of the g_m cell together, hence making the input voltage zero. Then the offset-cancellation feedback charges the capacitors to appropriate values that makes the two output voltages equal, hence canceling the offset at the output. The capacitors are chosen large enough to keep the voltage almost constant during the measurement time. The leakage current of the switches will change the cap voltages during the measurement; if this change is not kept small, it can introduce large errors and can even push the loop out of lock. Since each measurement takes less than 300 μs and the switch is connected between the capacitor and a high impedance node, the leakage current through the switch is very small and simulations show that a capacitor of 1 pF suffice. In addition to offset cancellation, this loop also makes the two outputs equal for the next measurement. During the measurement phase, the offset cancellation loop will be switched off and only the common-mode loop will function to keep the common-mode output voltages equal to around 0.9 V, which prohibits the transistors from going into triode. In a simple common-mode feedback, usually two large resistors are inserted between the two outputs and the common-mode voltage would be measured at the middle point. The output resistance of the gm cell is very high and in order to avoid the use of very large resistors for the common-mode feedback, two buffers are inserted between the outputs and the resistors. Since the voltage at the outputs of the gm cell can vary between $2V_{ov}$ and $V_{dd}-2V_{ov}$ (about 1 V), the buffers should be able to operate with this range of voltages and therefore push-pull buffers are utilized (as depicted in Fig. 6.5).

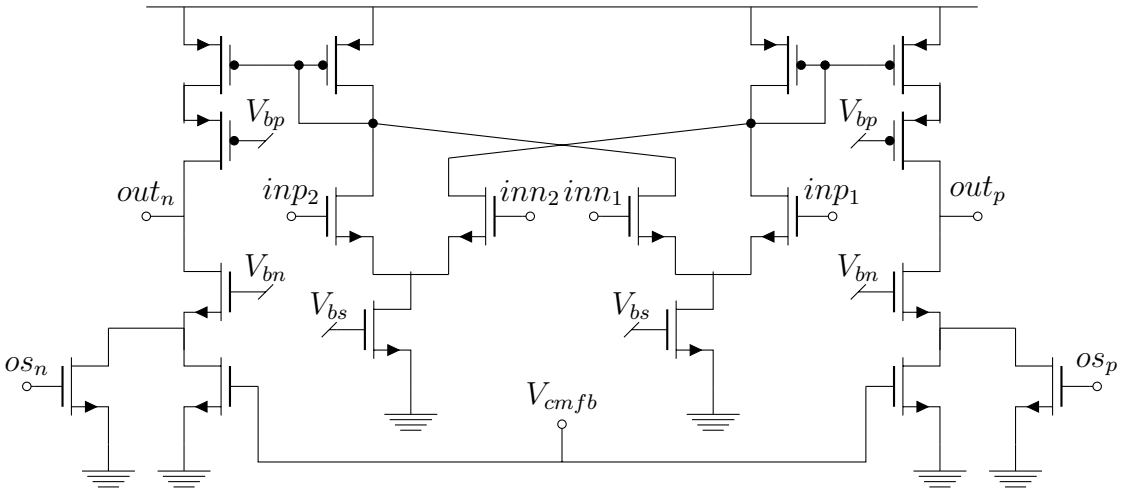

Fig. 6.4: OTA (g_m cell) schematic

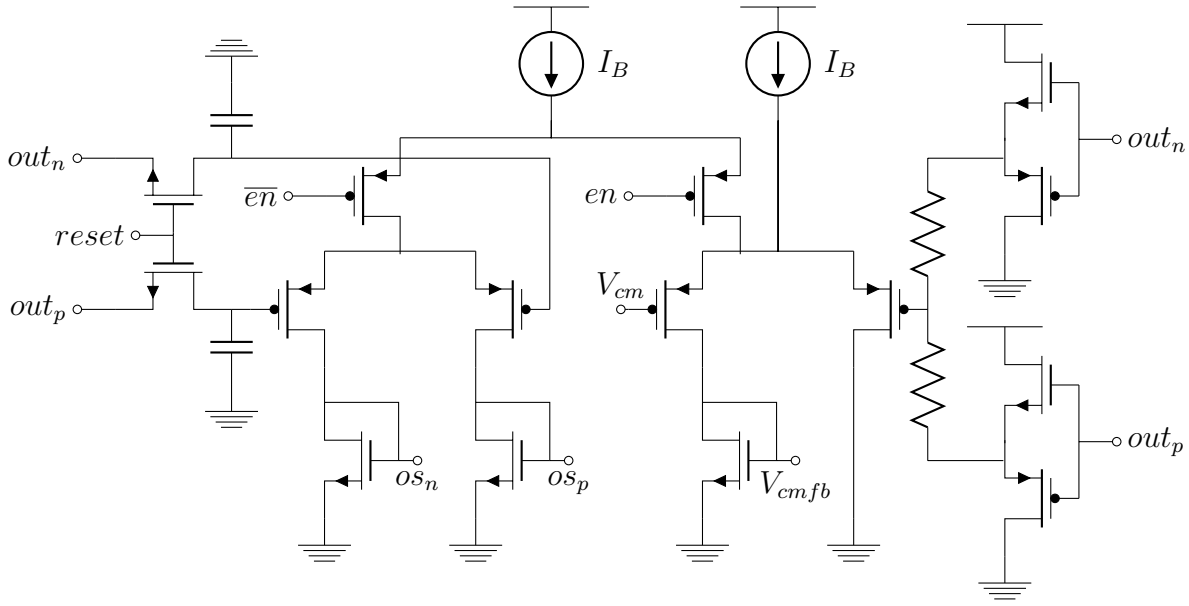

Fig. 6.5: g_m-cell offset and common-mode feedback.

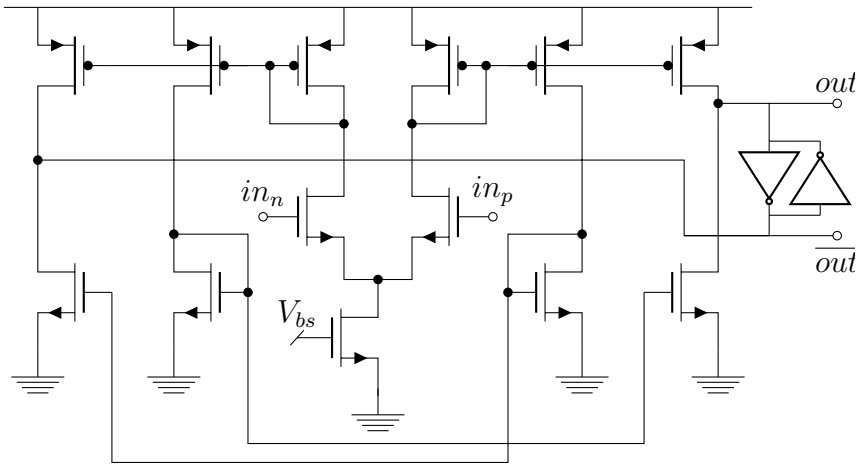

Fig. 6.6: CML-to-CMOS converter schematic.

CML-to-CMOS converter

The schematic of the CML-to-CMOS converter is shown in Fig. 6.6. An OTA converts the differential input to two complementary CMOS rail-to-rail outputs *out* and $\overline{out}$. The addition of back-to-back CMOS inverters at the output adds some positive feedback, thereby making the output rail-to-rail transitions sharper.

6.1.3 Simulation Results

In order to verify the performance of the proposed system, simulations were performed using the TowerJazz CA18 0.18μm CMOS process. Transient simulations at 100 MHz frequency with different input phase shifts and three different input amplitudes were performed for the Fig. 6.2(a) circuit with $K_{VCD} = \frac{\pi}{4}$ rad/v and $g_m = 200$ μS. Fig. 6.7(a) shows the normalized control voltage (V_c) vs. input phase (between $ref0$ and $V_{inp/n}$) corresponding to each of the four switch states. As illustrated in this figure, each quadrant of the 2π range is covered by one of the four states of the VCD. Also shown in this figure is a systematic offset $\Delta\phi$ of approximately 7°. This offset is primarily due to the parasitic capacitances of the switches

and the delays of the AND gates.

In Fig. 6.7(b) output phase (between *ref0* and *dly0*) vs. input phase (between $ref0$ and in) for one of the four quadrants (corresponding to S1) is shown for three different input amplitudes: 3 mV, 30 mV and 300 mV. The other three quadrants behave similarly. Fig. 6.7(c) shows the error of the simulated points compared to an ideal linear characteristic with the same phase offset. It can be seen that the input amplitude has a very small effect on the characteristic. The absolute error is less than 0.1° for $A_{in} = 30$ mV and $A_{in} = 300$ mV and less than 1.3° for $A_{in} = 3$ mV. A linear phase detector circuit, such as one based on an XNOR [31], would still be required to measure the phase between *ref0* and *dly0* accurately, but since these signals are both large amplitude, a limiting amplifier would not be necessary. Moreover, if somewhat less linearity (approx. ±2°) were required, V_C itself along with quadrant signals (S1-S4) could serve as a direct measure of the phase difference.

The worst-case locking time is approximately 250 μs, which is sufficiently fast for FDPM applications. Fig. 6.8 shows the transient behavior of the control voltage during the locking process for two different input amplitudes. It is evident in these simulations that the settling time increases with decreasing input amplitude. The entire phase measurement unit, excluding the signal generator, consumes 7 mA from a 1.8 V supply voltage.

6.2 Amplitude Measurement Unit

In order to take a precise measurement of the amplitude of the modulation signal from the tissue sample, it is necessary to first convert the amplitude to a dc level by rectifying the waveform, as described in [32]. Since the amplitude varies exponentially with the path length of the sample, a logarithmic amplifier whose output is proportional to the log of the input, such as that described in [33], can be used. On the other hand, when the phase

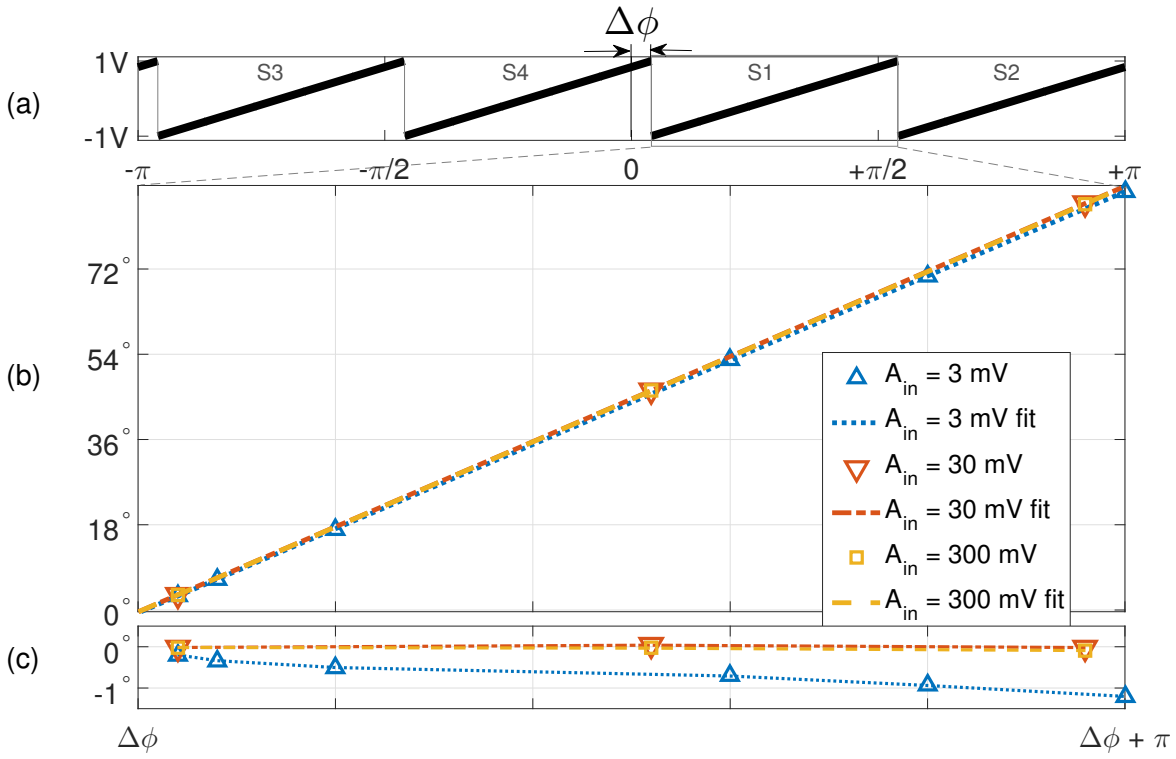

Fig. 6.7: (a) Normalized V_c vs. $\phi_{in}(rad)$;(b) $\phi_{out}(degrees)$ vs. $\phi_{in}(rad)$ of one of the four quadrants for three different input amplitudes; (c) deviation from linearity for the output phase (degrees) vs. input phase (rad).

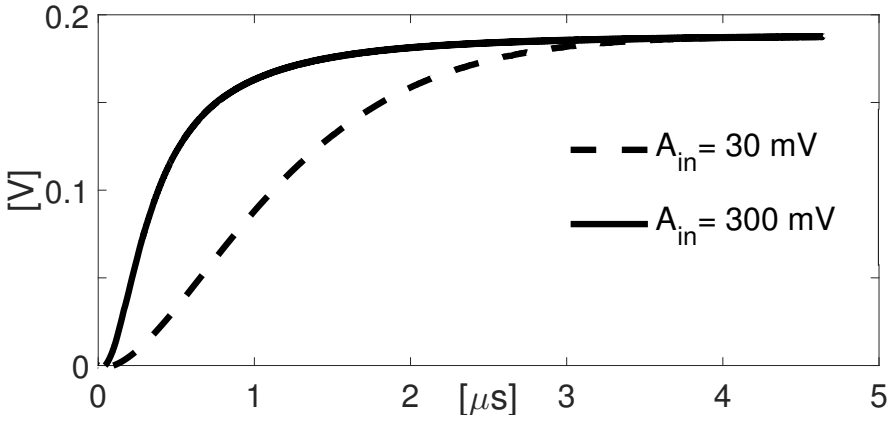

Fig. 6.8: Control voltage transient during locking process.

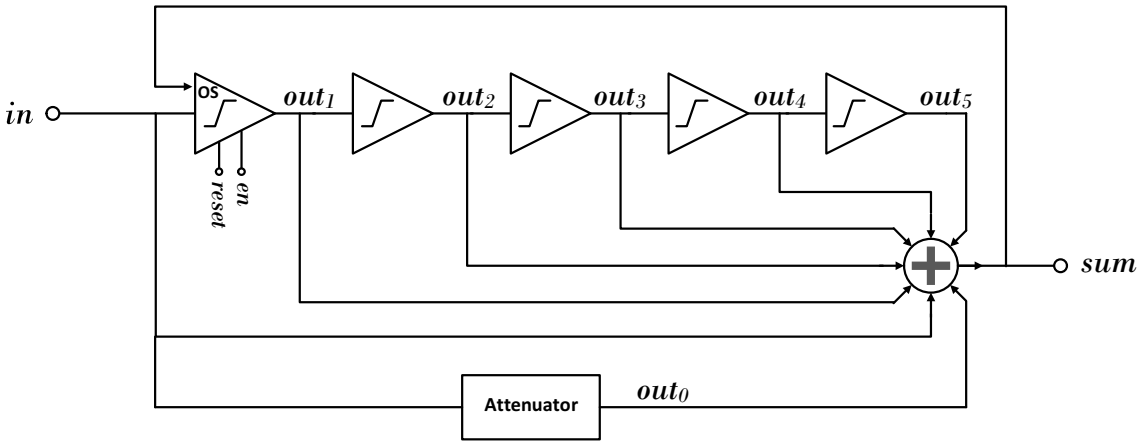

Fig. 6.9: Pseudo-logarithmic Amplifier Block Diagram

detector loop converges, the voltage on the N-path filter capacitors will be equal, positive, and proportional to the input amplitude. Therefore one of these voltages can be used as a rectified version of the input signal, which eliminates the need for a separate rectifier.

A pseudo-logarithmic amplifier can be implemented in a CMOS process by using multiple similar gain stages with saturation and adding their outputs together [33] as illustrated in Fig. 6.9. In order to extend the dynamic range of this block and enable measurement of strong inputs, an attenuator stage, which saturates after all the other blocks are saturated, is added. The gain and attenuator schematics are illustrated in Fig. 6.10. The summer circuit implementation is shown in Fig. 6.11.

As depicted in Fig. 6.12, the characteristic of the pseudo-log amplifier is very well defined for amplitudes as small as 300 μV and as large as 400 mV, providing a detection range of more than 60 dB. An auto-zeroing scheme similar to the offset-cancellation scheme used for the gm cell is also employed to reduce the offset of the amplifiers chain.

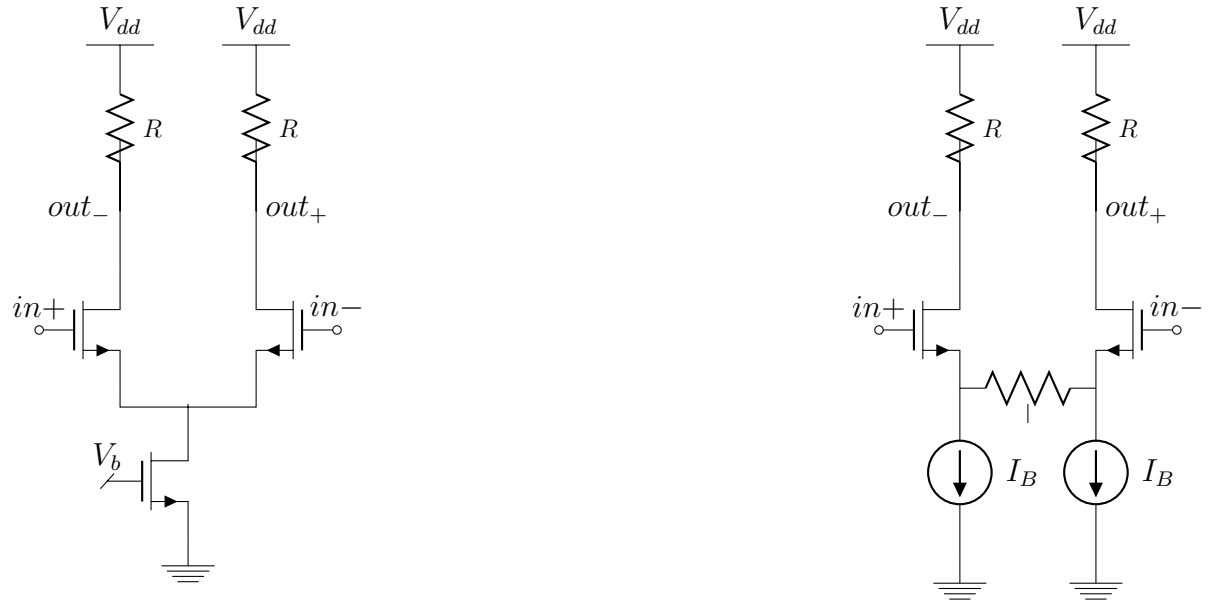

Fig. 6.10: Gain Stage (left); and Attenuating Stage (right) used in Pseudo-log Amplitude Detector.

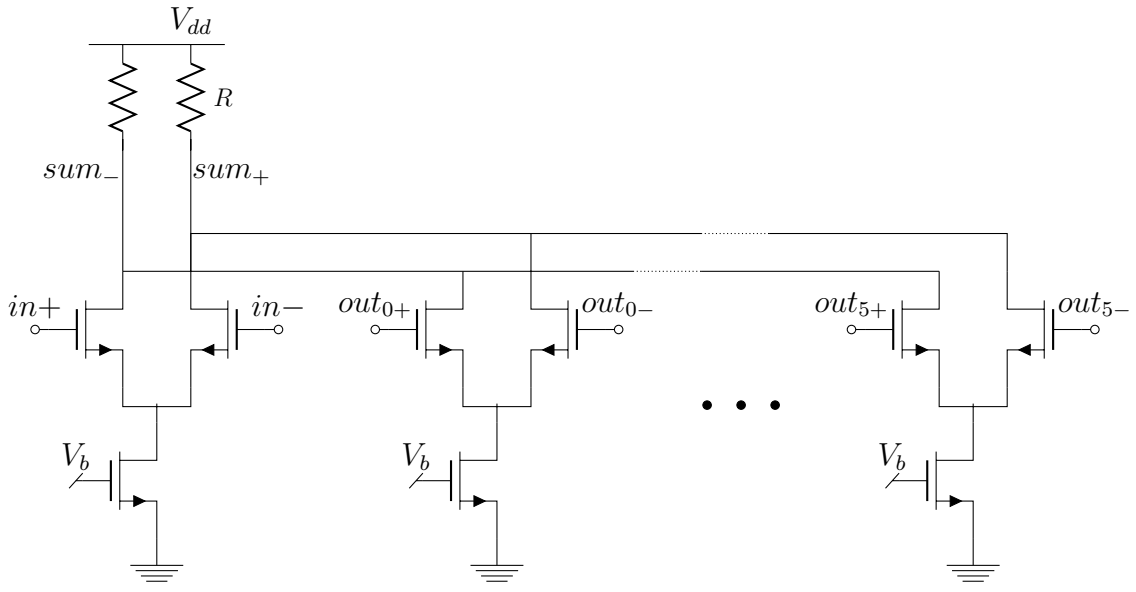

Fig. 6.11: Summer Circuit Schematic used in Pseudo-log Amplitude Detector.

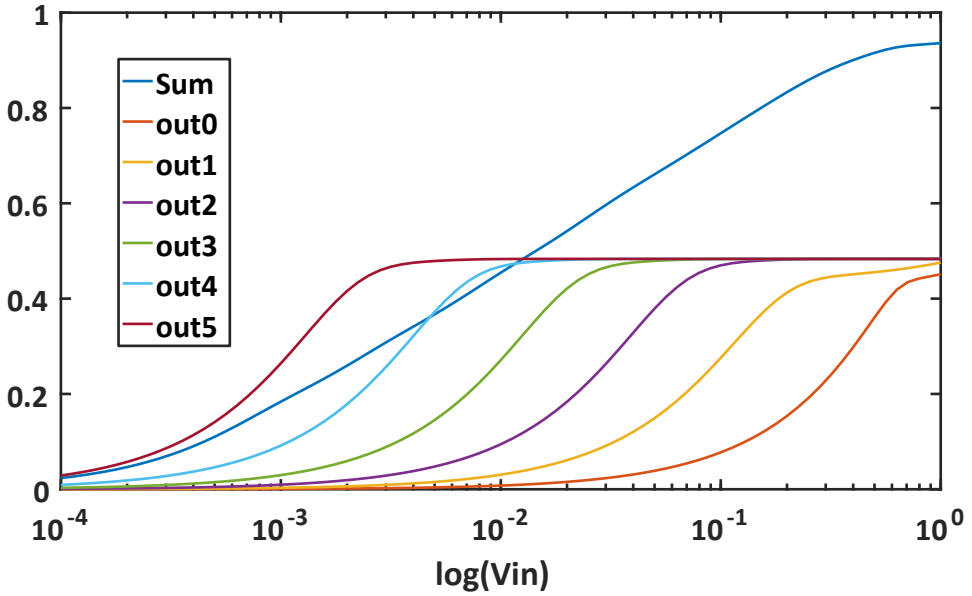

Fig. 6.12: Pseudo-logarithmic Amplifier Characteristic

Chapter 7

Transmitter

The transmitter architecture for the FDPM system is fairly simple. The output of the frequency synthesizer is taken off-chip and applied to a laser driver. The laser driver generates the required current for driving the laser and keeps its power regulated over time. There are four laser diodes generating light at four different wavelengths: 660, 690, 780, and 980 nm. A set of switches controlled by the micro-controller turn on the selected laser diode while turning the others off. The output of the laser driver is applied to the selected laser diode. The details of the off-chip laser driver and laser diodes are described in this chapter.

7.1 Laser Diodes

The detail of the chosen laser diodes are shown in Table 7.1.

Laser Diode	BlueSky Research VPSL0690-035X5A	Thorlab L785P090	BlueSky Research VPSL0830-050X5A	Qphotonics QLD-980-150S
Wavelength (nm)	690	785	830	980
Optical Power (mW)	35	90	50	150
Threshold Current (mA)	45	35	20	19
Slope Efficiency (W/A)	0.7	1.1	0.9	1
Operating Current (mA) at Max Power	-	120	75	170
Monitor Current (mA)	0.1	0.5	0.25	0.19

Table 7.1: Laser Diodes

7.2 Laser Driver

The schematic of the laser driver is illustrated in Fig. 7.1. A bias-tee network at the base of the high-ft NPN transistor combines the dc current and the modulating ac current. This current is then amplified by the npn transistor. The emitter current of the transistor is used to modulate the laser diode. A monitoring diode (MD) packaged with the laser diode (LD) monitors its average power. The current of the MD is proportional to the average power of the LD. This current is converted to a voltage by means of a resistor chosen appropriately for the given laser diode. This voltage is buffered by an op-amp-based unity-gain buffer. It is then integrated and compared with a reference voltage that is controlled by a digitally controlled potentiometer. The output of the integrator generates the dc component of the npn base current. This feedback network ensures the average output power of the laser diode remains constant over temperature variations.

The modulating signal is fed into the laser driver from the FDPM chip. The output of the chip can be modeled as an 80 mV_{pp} differential signal source with a 100 Ω differential source resistance. This signal is amplified by a high-bandwidth instrumentation amplifier and then passed through a resistor to set the current. The gain of the amplifier and the resistor value are adjusted for a modulation index of close to unity, thereby delivering maximum available ac power while keeping the average power below the threshold set by medical regulations – typically 20 mW.

In the complete implementation, there are four laser diodes, each at a different wavelength. At any given time only one of the laser diodes is illuminated. Therefore, the output of the instrumentation amplifier passes through a 1-to-4 switch that connects the modulating signal to one of the laser diodes. The power of the selected laser diode will be adjusted to about 20 mW by choosing the appropriate value on the potentiometer. The current of the other laser diodes will be brought down under their threshold current to minimize their optical output

power, but are not fully turned off in order to avoid long start-up times in transition from one diode to the next.

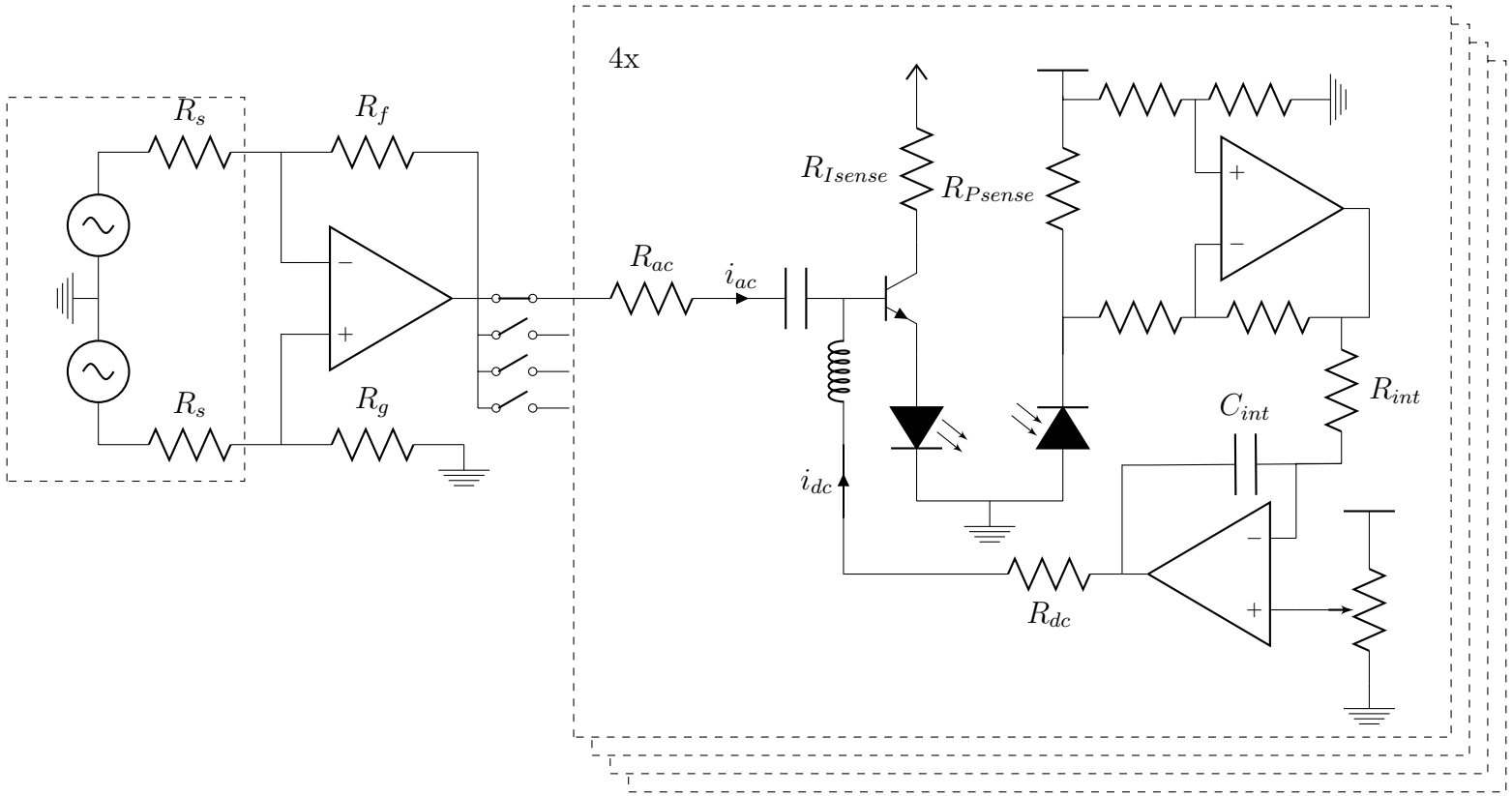

Fig. 7.1: Laser Driver Circuit with Power Control Loop

Chapter 8

Test Setup and Measurement

The FDPM chip has been fabricated in the TowerJazz SBC18H3 BiCMOS process which includes SiGe bipolar transistors and 180nm CMOS transistors; only the CMOS transistors are employed. Fig. 8.1 shows the top level layout of the chip including the pads. Different blocks are tagged on the layout. The chip has three different power domains: (1) for receiver front-end, (2) for receiver baseband and output buffer, and (3) for VCO and the $g_m - C$ lowpass filter; all operate from a 1.8 V supply.

The FDPM chip is packaged in a sealed 40-pin QFN package. Each pad on the chip excluding the ground pads is connected to one pin in the package through 25 μm gold bondwires. The four extra pins and all the ground pads (except the domain 2 ground) are down-bonded to the ground paddle at the bottom of the package. Fig. 8.2(a) and (b) show pictures of the die inside the QFN package and the stand-alone die, respectively. Table 8.1 shows the name, type and function of each of the pins on the package.

For evaluating the performance and characteristics of the fabricated chip, a round of electrical tests are performed on the chip to measure its sensitivity, phase and amplitude resolution, dynamic range and transient behavior. These test are described next.

Pin	Pin Name	Type	Function
1	amp_{2p}	AO	Amp. Det. 2 positive output
2	amp_{2n}	AO	Amp. Det. 2 negative output
3	amp_{1p}	AO	Amp. Det. 1 positive output
4	amp_{1p}	AO	Amp. Det. 1 negative output
5	TIA_{in}	AI	Input signal from the APD
6	TIA_Gain<1 >	DI	TIA gain control bit 1
7	TIA_Gain<0 >	DI	TIA gain control bit 0
8	$\overline{\text{VGA\_Gain}}$<1 >	DI	VGA gain control bit 1
9	$\overline{\text{VGA\_Gain}}$<0 >	DI	VGA gain control bit 0
11	VDD1	PWR	Supply for Domain 1
12	en_VGA_OC	DI	Enable/Disable VGA Offset Canc.
13	I_p	AO	I Phase Det. Positive Output
14	I_n	AO	I Phase Det. Negative Output
15	Q_p	AO	Q Phase Det. Positive Output
16	Q_n	AO	Q Phase Det. Negative Output
17	VDD3	PWR	Supply for Domain 3
18	en_VCO	DI	Enable/Disabel VCO
19	V_c_VCO	AI	Controls VCO Freq.
22	V_c_LPF	AI	Controls gmC LPF Corner Freq.
23	I_B_CML2CMOS	AI	CML2CMOS Bias Current
24	GND2	PWR	Ground for Domain 2
25	VDD2	PWR	Supply for Domain 2
26	IO_{270}	AIO	Ref_{270}
27	IO_{90}	AIO	Ref_{90}
28	IN_{180}	AI	Ref_{180}
29	IN_0	AI	Ref_0
31	q_0	DO	Quadrant Specifier Bit 0
32	q_1	DO	Quadrant Specifier Bit 1
33	VDD1	PWR	Supply for Domain 1
34	V_{fbp}	AO	Phase Meas. Feedback Signal (+)
35	V_{fbn}	DI	Phase Meas. Feedback Signal (-)
36	VhighThresh	AI	Quadrant Switching Threshold
37	reset	DI	reset
38	en_OC	DI	Enable/Disable Offset Cancellation
10, 20, 21, 30, 39, 40	GND	PWR	Ground for Domain 1 & 3

Table 8.1: Pin List for the Packaged Chip

For the electrical testing a PCB board was designed that includes all the connectors required to operate the chip stand-alone. The SMA connectors on the board can be used to directly connect the input and output pins of the chip to RF signal generators, oscilloscope and spectrum analyzer. The analog input voltages can be controlled using on-board potentiometers. All the digital inputs are connected to an array of pin headers for flexibility in connecting to a data acquisition system, or a logic analyzer, etc. All the outputs are connected to the test point hooks for easy probing. The fabricated board is shown in Fig. 8.3(a). The assembled board is shown in Fig. 8.3(b).

Before testing the receiver performance, in order to test the frequency synthesizer (i.e. VCO + LPF), the frequency synthesizer's output is fed into a spectrum analyzer and its spec are measured. The measured frequency vs. the VCO control voltage is shown in Fig. 8.4. These results are used in the next steps of the measurement to adjust the frequency of the frequency synthesizer. During these measurements, the control voltage of the LPF is adjusted for each frequency to keep the output swing at 80 mV_{pp} differentially. However at frequencies above 500 MHz the $g_m - C$ filter fails to adjust its corner frequency and the amplitude starts to drop. At frequencies above 800 MHz the output swing is halved, and above 1 GHz it drops below 27 mV_{pp}. This can be alleviated to some extent by increasing the power supply from 1.8 V. At 2 V supply voltage the output swing can be kept at 80 mV_{pp} up to 750 MHz and the amplitude is above 40 mV_{pp} up to 1.1 GHz. In brief, although the frequency synthesizer frequency can be adjusted anywhere from 5 MHz up to 1.1 GHz, its usable range that provides acceptable signal level and phase noise is limited to 50-800 MHz.

After characterizing the on-chip signal generator, a test as shown in Fig. 8.5 is set up for testing the complete system. In this setup, the output of the on-chip signal generator is amplified (by ZFL-2000GH+ from Mini-Circuits) to 8 dBm and applied to a quadrature modulator (TRF370417 evaluation board from TI) followed by a combination of attenuators (VAT-20+ and ZFAT-51020 from Mini-Circuits). The quadrature modulator can be used

to phase shift the signal by an arbitrary amount by varying the weight of the in-phase and quadrature arms. The output of the modulator will be around 6 dBm and the attenuator combination can provide any attenuation from 0-55 dB in 5 dB steps. The output of the attenuator is then applied to one side of a 10 kΩ resistor, with its other side is connected to the input of the TIA. By using this setup, the input current amplitude of TIA can be adjusted from 100 nA to 63 μA.

By applying the output of the signal generator to the LO port of the quadrature modulator and applying two baseband signals (I_{BB} and Q_{BB}) to its baseband ports, the output RF signal can be written as:

$$V_{RF} = I_{BB}(t).V_p \sin(2\pi f_{LO}) + Q_{BB}(t).V_p \cos(2\pi f_{LO}) \tag{8.1}$$

By applying different baseband signals to the modulator, different tests can be performed. Two of these tests are described here:

8.1 Constant Amplitude Test

This test is performed to evaluate the accuracy and linearity of the phase measurement unit. If the two baseband signals of the modulator are chosen to be $\cos(2\pi f_{BB})$ and $-\sin(2\pi f_{BB})$, respectively, the output of the modulator will be:

$$V_{RF} = -\sin(2\pi f_{BB}).V_p \sin(2\pi f_{LO}) + \cos(2\pi f_{BB}).V_p \cos(2\pi f_{LO}) = V_p \cos(2\pi(f_{LO} + f_{BB})) \tag{8.2}$$

Therefore the output will have a constant amplitude and a frequency of $f_{LO} + f_{BB}$. After passing this signal through the attenuators and a 10 kΩ resistor, the generated current will

be fed as the input to the TIA. The test is performed at 400 MHz modulation frequency with a constant input amplitude of 3.5 μA_{pp} and baseband frequency of 1 Hz, which causes a phase difference between the input and reference signals that varies linearly from 0 to 360 degrees every 1 s; therefore it is expected to measure a linearly varying phase and a constant amplitude at the output of the chip. The measured phase, amplitude, feedback voltage, and the quadrant bits (q_0 and q_1) are recorded from the oscilloscope as shown in Fig. 8.6. As expected the amplitude is constant while the two phase measurements vary linearly in quadrature. Using the method in [34], the phase is reconstructed from the measured outputs of the XNOR-based I and Q phase detectors. This final phase is shown in Fig. 8.7. Without any kind of post-processing, the rms phase error and maximum phase error are calculated to be 2° and 6.3°, respectively. Part of this error ($1.7°RMS$) is due to non-linearity and part ($1°RMS$) due to noise. The measured amplitude is 1.75 $\mu A \pm 10\%$. The amplitude measurement error is 6.5% rms. This error is partly due to offset as discussed in the next section and partly due to the noise.

8.2 Constant Phase Test

In order to test the amplitude detector response, in the second test Q_{BB} is set to zero and I_{BB} is a triangle waveform varying from -1 V to +1 V. By applying this waveform, the phase should remain constant while I_{BB} is either positive or negative. During the transition from positive to negative or vice versa a phase jump of 180° is expected. The amplitude is expected to vary linearly in this test. The waveforms recorded from this test are shown in Fig. 8.8. It can be observed that the phase measurement loop feedback voltage is almost constant while the input amplitude is large. As the input amplitude becomes too small, the feedback voltage starts to diverge and the phase detectors start to fail, but as the amplitude rises again with the opposite polarity, the quadrant bits change from 01 to 11 and the feedback voltage

converges to its previous value indicating a 180° phase shift in the signal. In this case, the I and Q phase detectors output voltages are negative of their previous value indicating a 180° phase shift.

As explained before, the amplitude detector is realized as a pseudo-log amplifier. Since the amplitude detector measures the log of the voltage across the capacitor of the N-path filter, the actual input amplitude should be calculated from the measured amplitude using:

$$amp_{in} = \frac{\pi}{2} \times (0.07\text{mV} \times 10^{\frac{amp_{meas}}{190\ \text{mV}}})/gain_{FE} \tag{8.3}$$

where the $\frac{\pi}{2}$ factor is due to the averaging of the signal in the N-path; the expression in the parenthesis is calculated by curve fitting to the characteristic of the pseudo-log amplifier as shown in Fig. 8.9; and $gain_{FE}$ is the receiver front-end gain. The input amplitude calculated using this equation is plotted in Fig. 8.10. The two peaks of the calculated amplitude should theoretically be equal, however the offset caused by the mismatch in the VGA (about 2 mV) amplified by its gain introduces around 60 mV offset into the N-path filter, which results in the imbalance of the two peaks. By knowing this offset we can correct our measurements in the post-processing; however this offset limits the sensitivity of the system. These measurements are captured without any offset cancellation mechanism.

After correcting for the effect of offset, the amplitude measurement maximum and rms errors are calculated as 130 nA and 50 nA, respectively. These errors result from the noise and nonlinearity of the system. With averaging multiple measurements the effect of noise can be reduced; with more measurements the nonlinearity can be characterized and compensated as long as the characteristic is monotonic. A similar test, but with a sinusoidally varying amplitude, is also performed and the calculated input amplitude is plotted in Fig. 8.11 for

comparison.

The measured errors are a combination of non-linearity and noise of multiple components including the receiver, signal generator, external amplifier, modulator, attenuator, and the resistor used to convert voltage to current. Measuring the performance of the receiver alone requires four phase coherent RF signal generators which was not available during these measurements.

The total current consumption of the chip at 400 MHz is 61 mA, half of which is consumed by the $g_m - C$ filter.

The suggested tests were performed for multiple input amplitude showing consistent behavior. The summary of the results are shown in Table 8.2.

Power Consumption	61 mA at 400 MHz
Phase Gain	4.5 mV/°
Receiver Sensitivity	70 nA_{rms}
Calculated Optical Sensitivity (with a photo-sensitivity of 30 over 600-950nm)	-57 dBm
Phase Measurement Noise	1°
Phase Measurement Non-linearity	<0.5 %
Amplitude Gain	300 mV/decade
Amplitude Measurement Error	6 %

Table 8.2: Chip Performance Summary

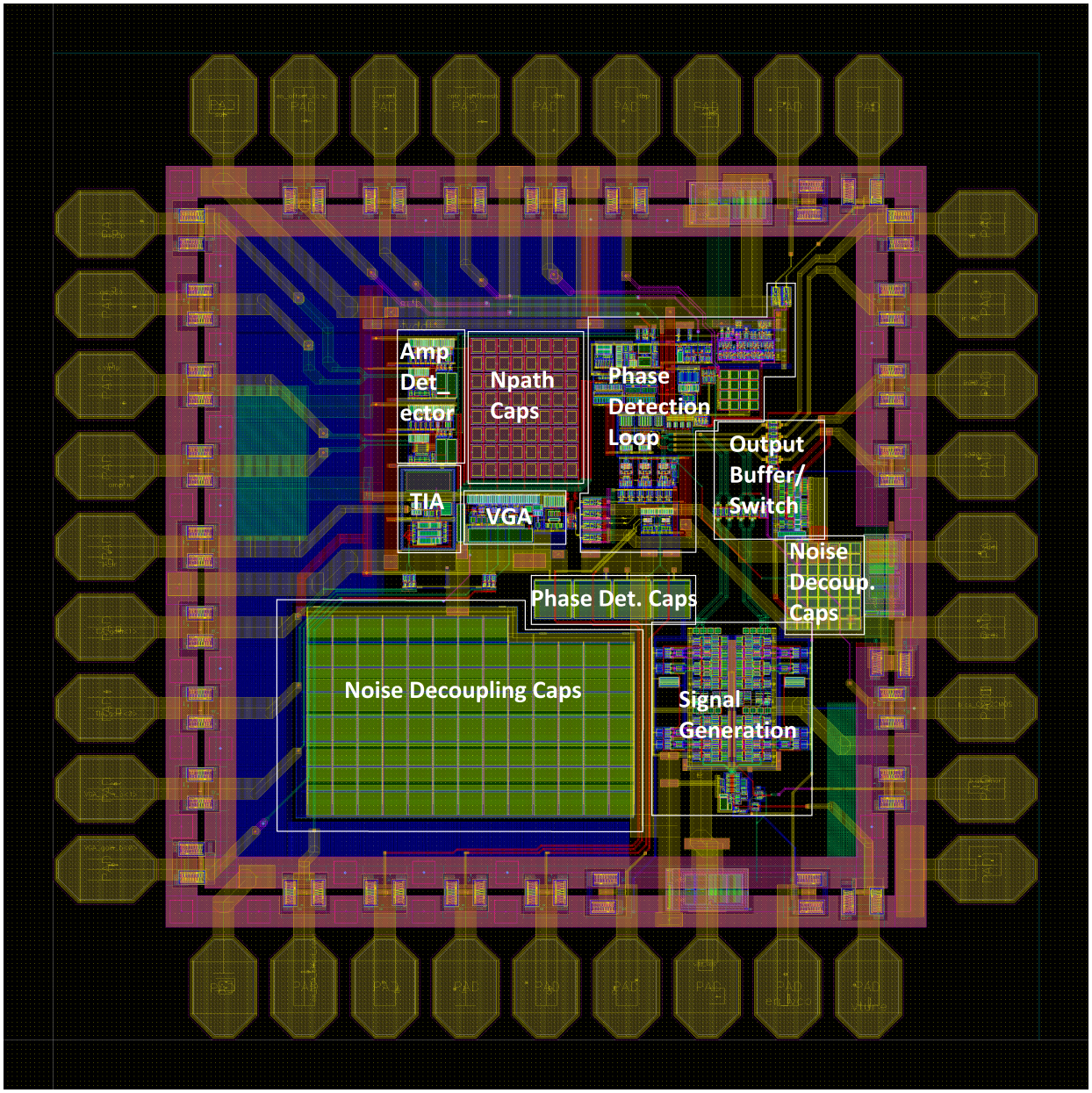

Fig. 8.1: FDPM Chip Layout

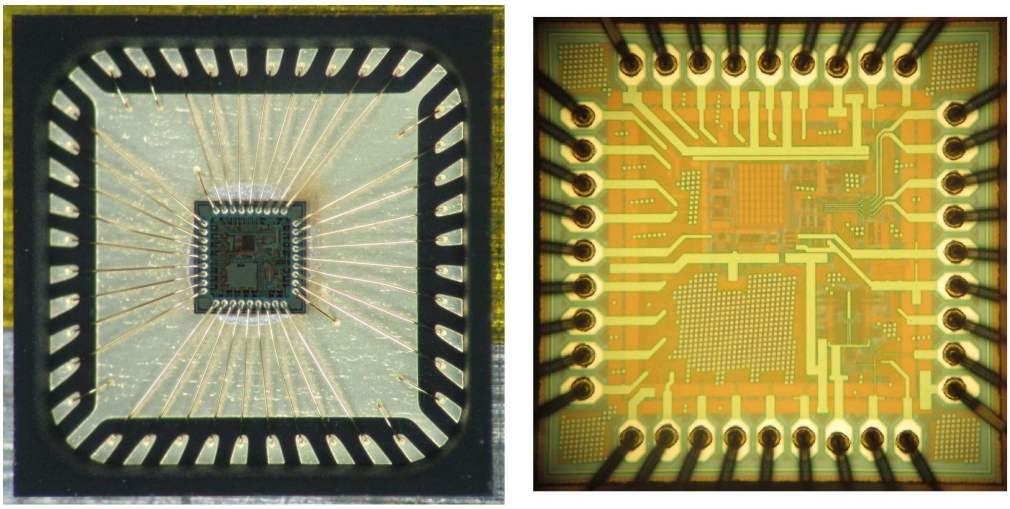

Fig. 8.2: (a) Photograph of the Chip Bondwired to the QFN package; (b) Chip photograph.

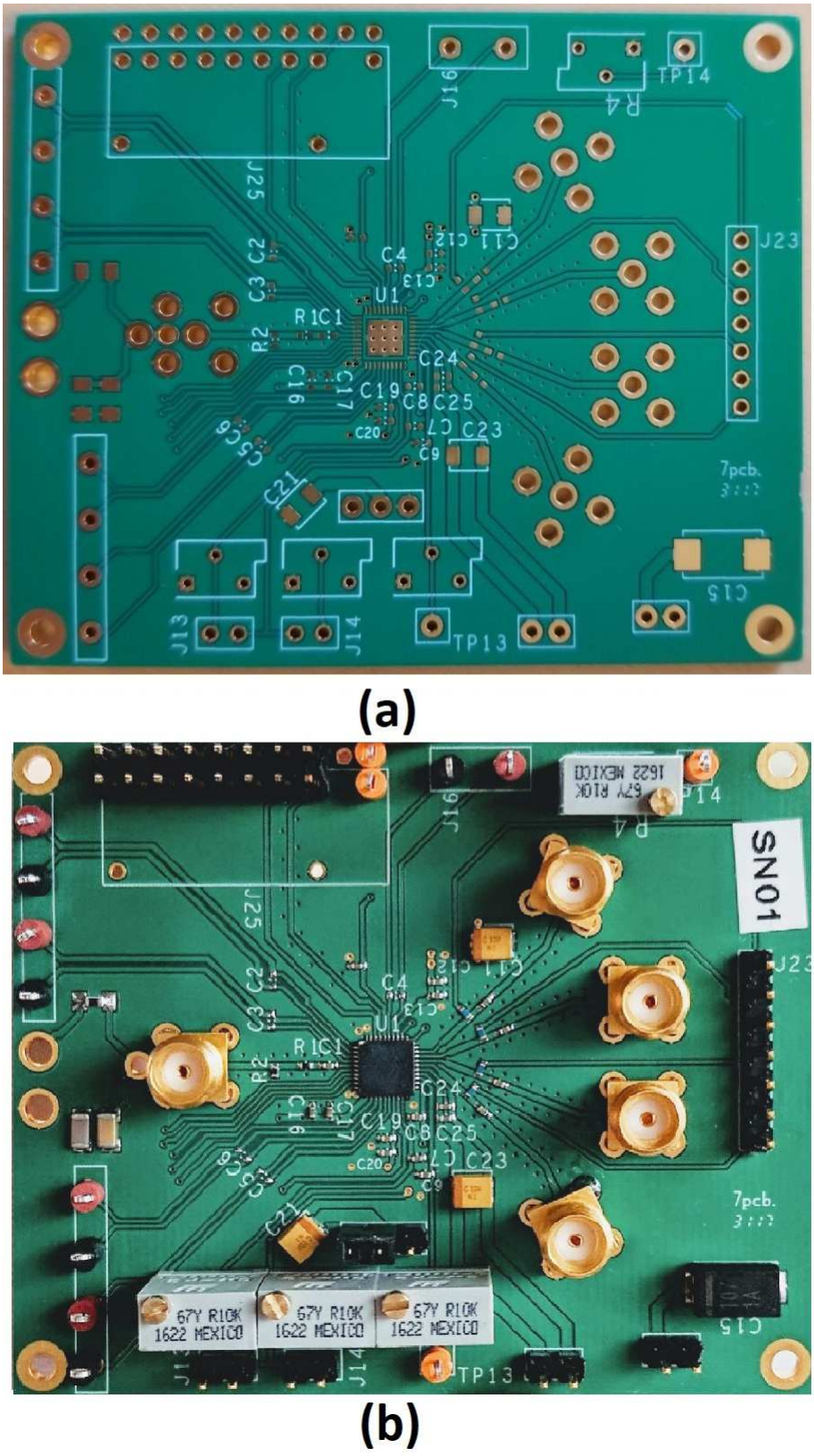

Fig. 8.3: Printed Circuit Board: (a) by itself (b) populated with components.

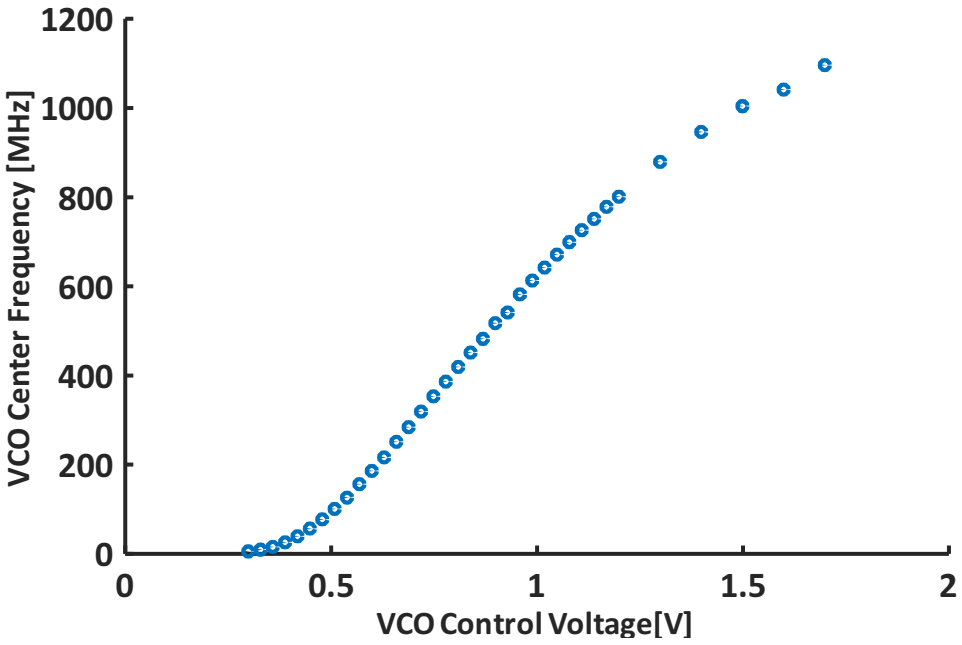

Fig. 8.4: Measured VCO Characteristic

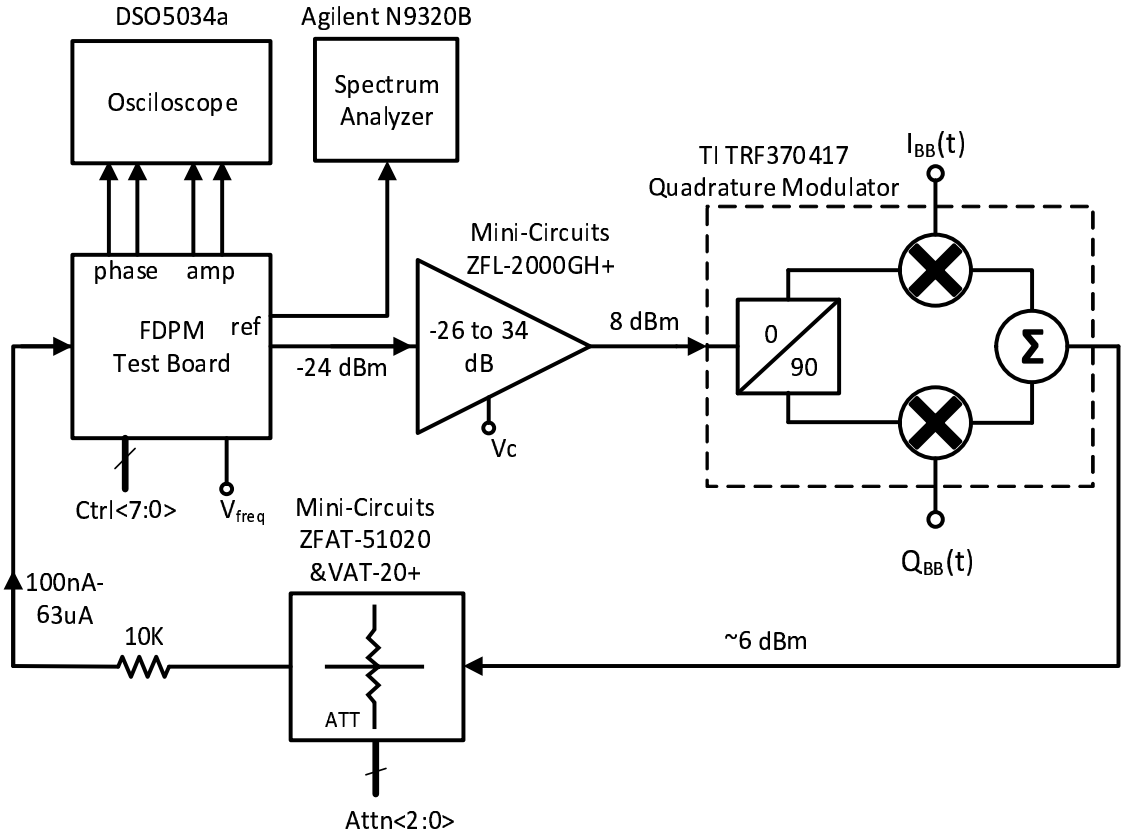

Fig. 8.5: Electrical Test Setup

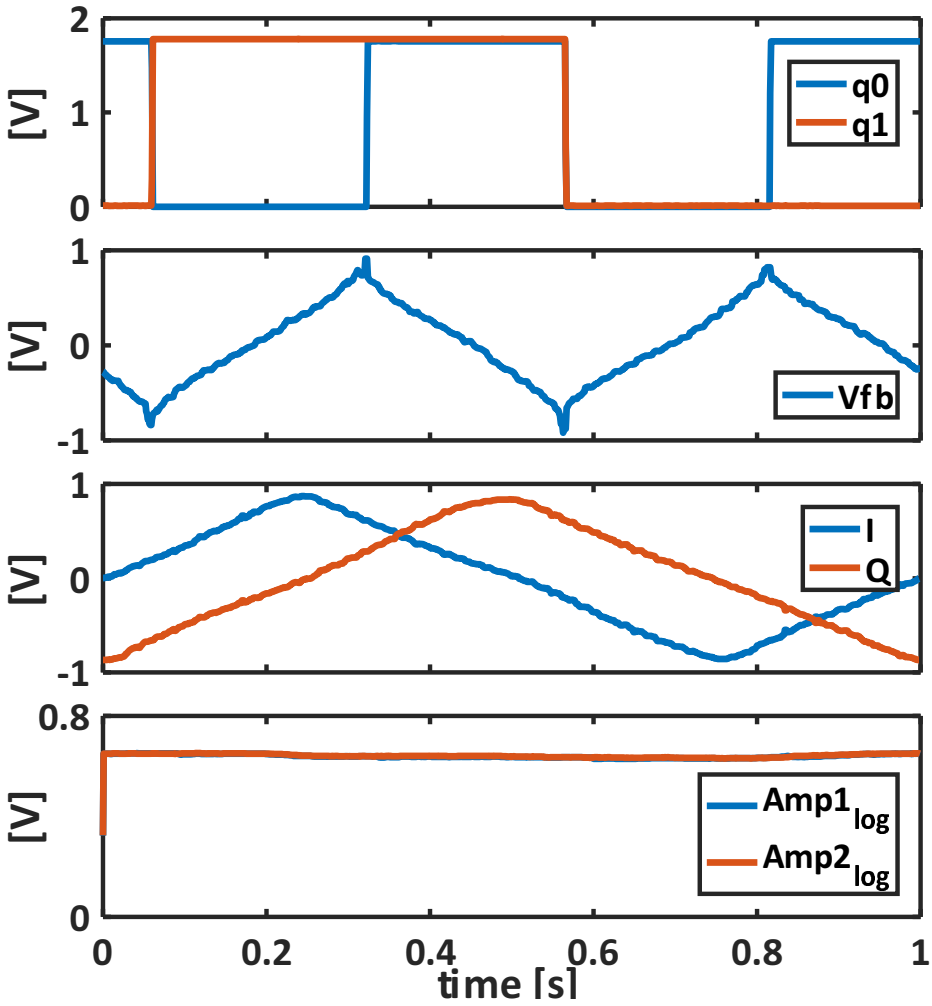

Fig. 8.6: Constant Amplitude Test Results: (a) Quadrant Bits; (b) Feedback Voltage; (c) Phase Measurement Outputs; (d) Amplitude Measurement Outputs.

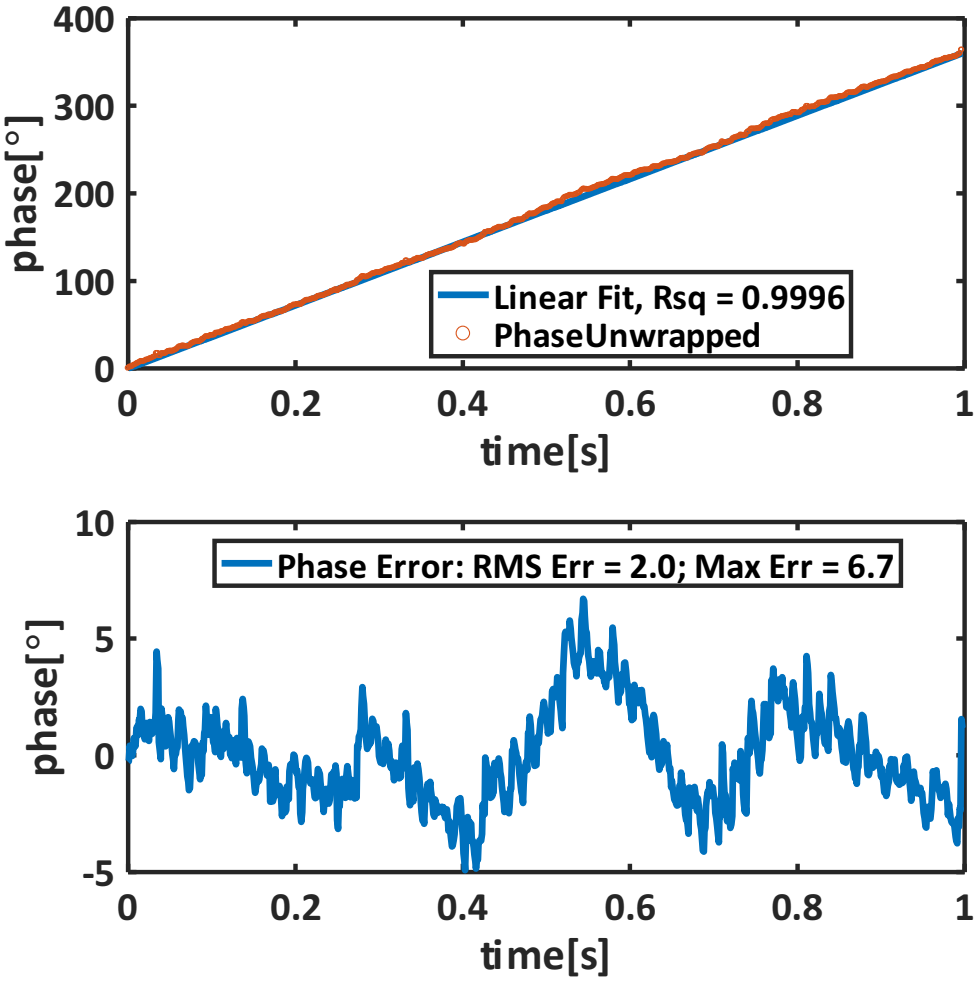

Fig. 8.7: Constant Amplitude Test Result: (a) Phase Reconstructed from I and Q phase measurements; (b) Phase Error.

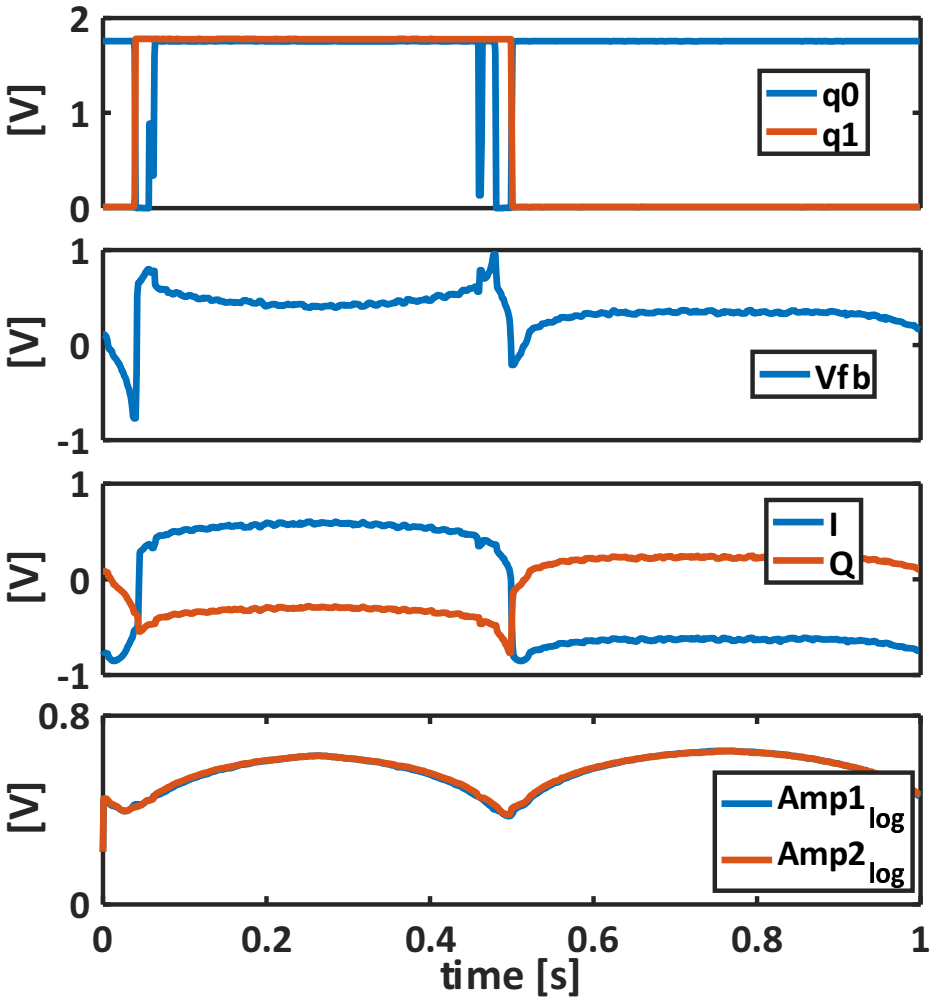

Fig. 8.8: Constant Phase Test Results for Linearly Varying Amplitude: (a) Quadrant Bits; (b) Feedback Voltage; (c) Phase Measurement Outputs; (d) Amplitude Measurement Outputs.

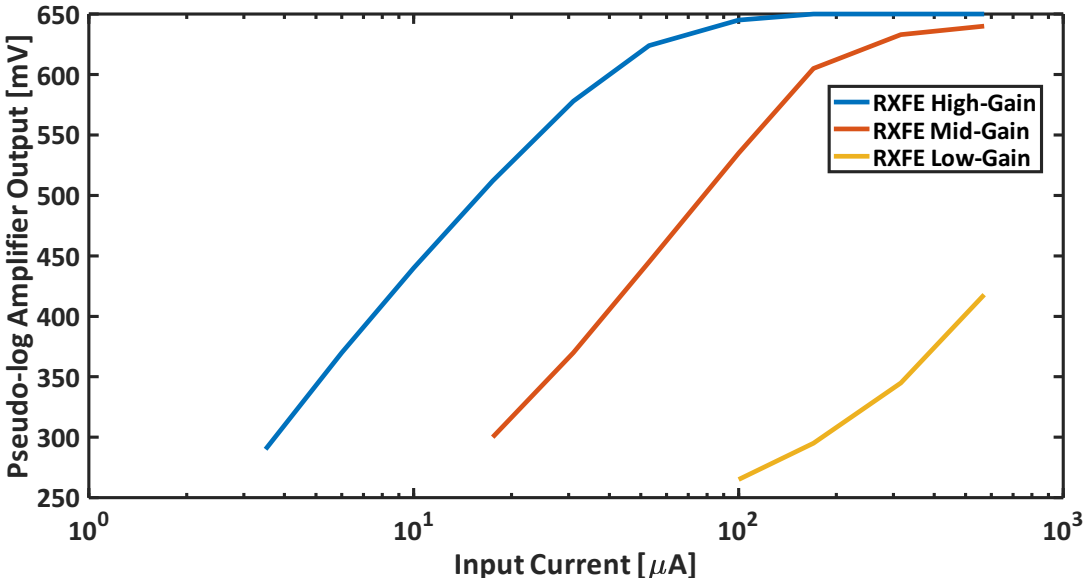

Fig. 8.9: Pseduo-log Amplitude Detector Measured Characteristic

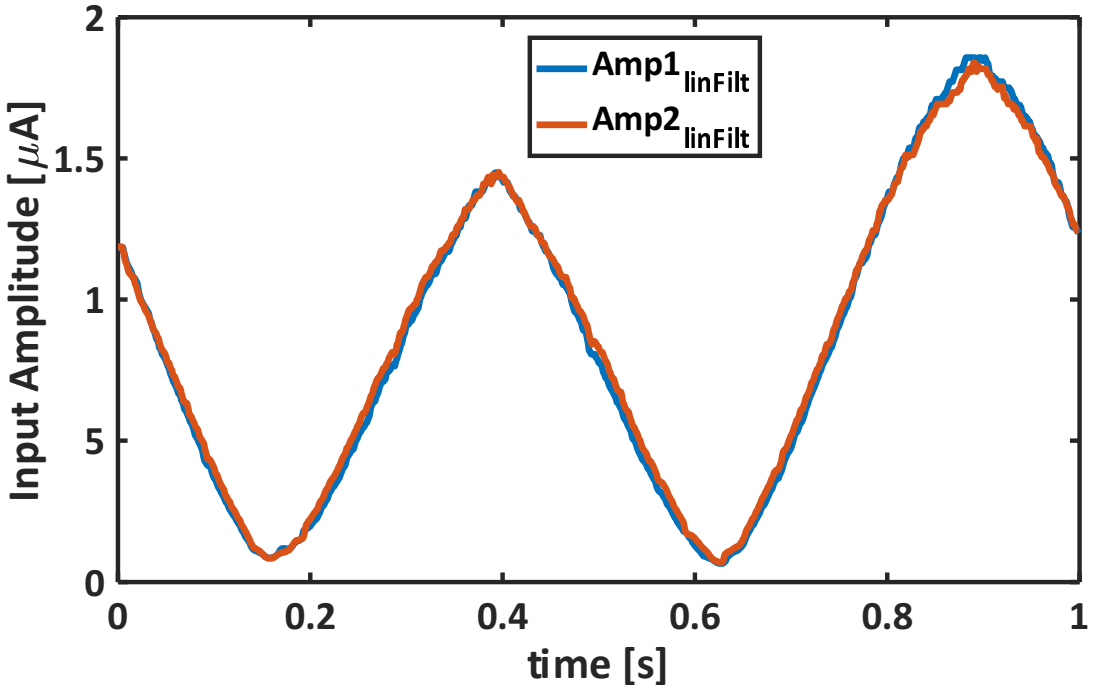

Fig. 8.10: Constant Phase Test Results for Linearly Varying Amplitude: Input Amplitude Calculated from Fig. 8.8 (d) using (8.3).

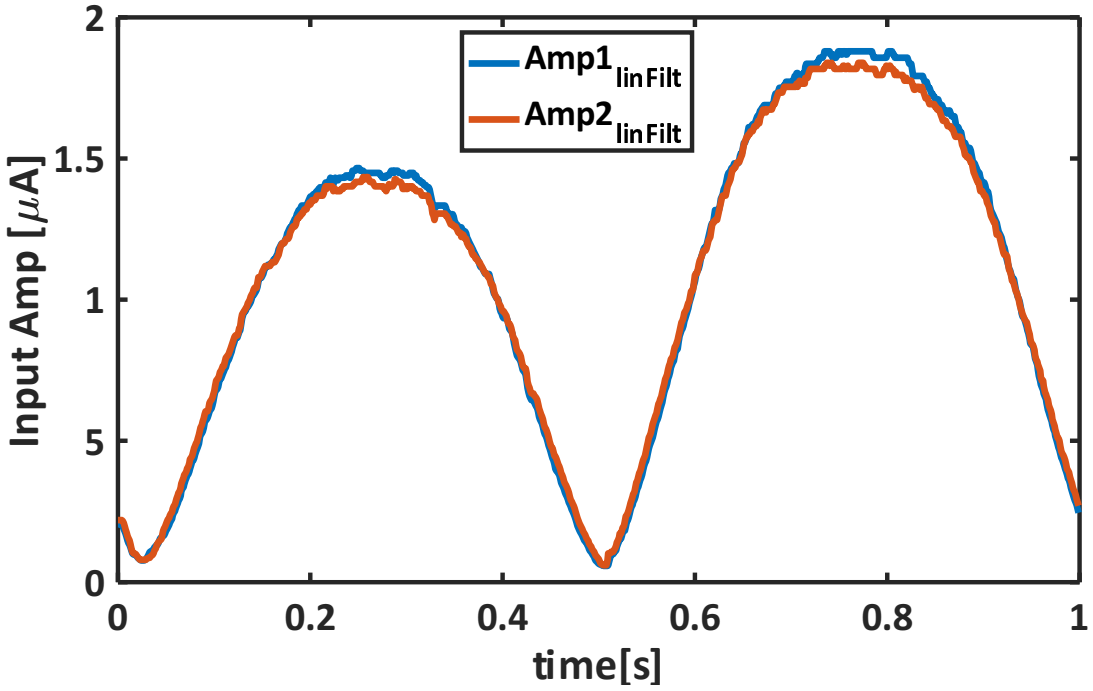

Fig. 8.11: Constant Phase Test Results for Sinusoidally Varying Amplitude

Chapter 9

Conclusion

In this dissertation, the diffuse optical imaging (DOI) has been explained as a low-cost non-invasive method for imaging body tissue up to a few centimeters deep. Different modalities of the DOI are compared, concluding that CW-DOI is too simple to measure the scattering, and more complicated time-resolved methods are required. Between the two time-resolved methods (i.e. FD-FOI and TD-DOI), FD-DOI is chosen – due to its simpler architecture and lower cost – to be implemented on chip. The physics of the amplitude-modulated light propagation inside a scattering medium has been explained; and measured parameters (phase-shift and modulation depth) relationship to the optical properties of the medium (absorption coefficient and reduced scattering coefficient) was derived. It was also shown how the FDPM measurement results are fit into the theoretical model to derive the optical properties of the tissue. It was then described how the use of multiple optical wavelengths in an FDPM measurement can provide enough information to separate the effect of scattering and absorption and extract the concentration of different chromophores inside a medium. The importance of accurate phase measurement is emphasized. The previous work done in this area and their drawbacks are explained. It is specifically pointed out that none of the existing instruments are suitable for a low-power, low-cost and wearable form for the vast

emerging applications that rely on these properties to become feasible.

The standard CMOS process was chosen as the fabrication process for its availability and low-cost. The proposed architecture is introduced with a focus on accurately tunable bandpass filtering to improve the sensitivity of the system.

Different schemes for implementing a wide-tuning range frequency synthesizer are compared. A compact quadrature CMOS ring oscillator is implemented. A new replica biasing scheme for this oscillator is employed that enables very wide tuning range for the oscillator. Different near-infrared photo-detectors are compared for FDPM application. The detector of choice (APD), is carefully studies and different noise factors affecting the sensitivity of the system are examined. Methods for improving the sensitivity by adjusting the gain of the APD or use of bandpath filtering are considered. As one of the most sensitive blocks of the system, the TIA design trade-offs are explained in details.

Novel ideas for reusing the N-path filter for low-power phase detection and amplitude rectification are presented. A feedback phase detector is implemented and its linearity is evaluated. A pseudo-log amplifier is implemented. It is shown that the addition of an attenuator stage to this amplifier can extend its detection range for higher input amplitudes.

A laser driver circuit with automatic power control to be interfaced with the chip is designed. Due to the need for high current gain at hundreds of MHz, a CMOS implementation of the laser driver will be inefficient and an external SiGe high-speed amplifier followed by a high-ft npn transistor is used in the design.

The characteristic of the fabricated chip is measured and evaluated at 400 MHz modulation frequency. Using the on-chip signal generator, the receiver has a sensitivity of 70 nA_{rms} and phase and amplitude measurement errors of 2° rms and 50 nA_{rms}, respectively. These measured errors are a combination of non-linearity and noise of multiple components including the receiver, signal generator, external amplifier, modulator, attenuator, as well as the resis-

tor used to convert the voltage to current. With further measurements, the non-linearities can be characterized and compensated in the measurements. With averaging the error due to noise can be reduced at the cost of longer measurement times.

To the best of our knowledge, this work is the first fully integrated multi-frequency FDPM sensor ever implemented. CMOS implementation of the FDPM system enables the future integration of the digital logic including the control unit, data processing unit and possibly wireless communication unit for a fully-integrated wearable FDPM SoC. The small size, low power and fast operation speed of this module enables applications like real-time sampling and multi-channel integration of these sensors for application like brain oxygenation monitoring.

References

[1] H. Tecco. 2016 Year End Funding Report: A reality check for digital health Rock Health 2016. [Online]. Available: https://rockhealth.com/reports/2016-year-end-funding-report-a-reality-check

[2] D. A. Boas, A. M. Dale, and M. A. Franceschini, "Diffuse optical imaging of brain activation: approaches to optimizing image sensitivity, resolution, and accuracy," *NeuroImage*, vol. 23, pp. S275 – S288, 2004, mathematics in Brain Imaging. [Online]. Available: http://www.sciencedirect.com/science/article/pii/S1053811904003763

[3] A. T. Eggebrecht, S. L. Ferradal, A. Robichaux-Viehoever, M. S. Hassanpour, H. Dehghani, A. Z. Snyder, T. Hershey, and J. P. Culver, "Mapping distributed brain function and networks with diffuse optical tomography," *Nature photonics*, vol. 8, no. 6, pp. 448–454, 2014.

[4] T. Durduran, G. Yu, M. G. Burnett, J. A. Detre, J. H. Greenberg, J. Wang, C. Zhou, and A. G. Yodh, "Diffuse optical measurement of blood flow, blood oxygenation, and metabolism in a human brain during sensorimotor cortex activation," *Opt. Lett.*, vol. 29, no. 15, pp. 1766–1768, Aug 2004. [Online]. Available: http://ol.osa.org/abstract.cfm?URI=ol-29-15-1766

[5] L. Meng, M. Cannesson, B. S. Alexander, Z. Yu, Z. N. Kain, A. E. Cerussi, B. J. Tromberg, and W. W. Mantulin, "Effect of phenylephrine and ephedrine bolus treatment on cerebral oxygenation in anaesthetized patients," *BJA: British Journal of Anaesthesia*, vol. 107, no. 2, pp. 209–217, 2011. [Online]. Available: +http://dx.doi.org/10.1093/bja/aer150

[6] J. P. Culver, T. Durduran, D. Furuya, C. Cheung, J. H. Greenberg, and A. G. Yodh, "Diffuse optical tomography of cerebral blood flow, oxygenation, and metabolism in rat during focal ischemia," *Journal of Cerebral Blood Flow & Metabolism*, vol. 23, no. 8, pp. 911–924, 2003, pMID: 12902835. [Online]. Available: http://dx.doi.org/10.1097/01.WCB.0000076703.71231.BB

[7] S. H. Chung, M. D. Feldman, D. Martinez, H. Kim, M. E. Putt, D. R. Busch, J. Tchou, B. J. Czerniecki, M. D. Schnall, M. A. Rosen, A. DeMichele, A. G. Yodh, and R. Choe, "Macroscopic optical physiological parameters correlate with microscopic proliferation and vessel area breast cancer signatures," *Breast Cancer Research*, vol. 17, no. 1, p. 72, May 2015. [Online]. Available: https://doi.org/10.1186/s13058-015-0578-z

[8] S. Jiang, B. W. Pogue, P. A. Kaufman, J. Gui, M. Jermyn, T. E. Frazee, S. P. Poplack, R. DiFlorio-Alexander, W. A. Wells, and K. D. Paulsen, "Predicting breast tumor response to neoadjuvant chemotherapy with diffuse optical spectroscopic tomography prior to treatment," *Clinical Cancer Research*, vol. 20, no. 23, pp. 6006–6015, 2014. [Online]. Available: http://clincancerres.aacrjournals.org/content/20/23/6006

[9] H. S. Yazdi, T. D. O'Sullivan, A. Leproux, B. Hill, A. Durkin, S. Telep, J. Lam, S. S. Yazdi, A. M. Police, R. M. Carroll, F. J. Combs, T. StrÃűmberg, A. G. Yodh, and B. J. Tromberg, "Mapping breast cancer blood flow index, composition, and metabolism in a human subject using combined diffuse optical spectroscopic imaging and diffuse correlation spectroscopy," *Journal of Biomedical Optics*, vol. 22, pp. 22 – 22 – 10, 2017.

[10] D. Roblyer, S. Ueda, A. Cerussi, W. Tanamai, A. Durkin, R. Mehta, D. Hsiang, J. A. Butler, C. McLaren, W.-P. Chen, and B. Tromberg, "Optical imaging of breast cancer oxyhemoglobin flare correlates with neoadjuvant chemotherapy response one day after starting treatment," *Proceedings of the National Academy of Sciences*, vol. 108, no. 35, pp. 14 626–14 631, 2011. [Online]. Available: http://www.pnas.org/content/108/35/14626.abstract

[11] A. E. Cerussi, V. W. Tanamai, D. Hsiang, J. Butler, R. S. Mehta, and B. J. Tromberg, "Diffuse optical spectroscopic imaging correlates with final pathological response in breast cancer neoadjuvant chemotherapy," *Philosophical Transactions of the Royal Society of London A: Mathematical, Physical and Engineering Sciences*, vol. 369, no. 1955, pp. 4512–4530, 2011. [Online]. Available: http://rsta.royalsocietypublishing.org/content/369/1955/4512

[12] L. F. Ferreira, D. K. Townsend, B. J. Lutjemeier, and T. J. Barstow, "Muscle capillary blood flow kinetics estimated from pulmonary O2 uptake and near-infrared spectroscopy," *Journal of Applied Physiology*, vol. 98, no. 5, pp. 1820–1828, 2005. [Online]. Available: http://jap.physiology.org/content/98/5/1820

[13] G. Ganesan, J. A. Cotter, W. Reuland, A. E. Cerussi, B. J. Tromberg, and P. Galassetti, "Effect of blood flow restriction on tissue oxygenation during knee extension," *Medicine and science in sports and exercise*, vol. 47, no. 1, p. 185–193, January 2015. [Online]. Available: http://europepmc.org/articles/PMC4246015

[14] B. Chance, M. Cope, E. Gratton, N. Ramanujam, and B. Tromberg, "Phase measurement of light absorption and scatter in human tissue," *Review of Scientific Instruments*, vol. 69, no. 10, pp. 3457–3481, 1998. [Online]. Available: http://dx.doi.org/10.1063/1.1149123

[15] B. J. Tromberg, L. O. Svaasand, T.-T. Tsay, and R. C. Haskell, "Properties of photon density waves in multiple-scattering media," *Appl. Opt.*, vol. 32, no. 4, pp. 607–616, Feb 1993. [Online]. Available: http://ao.osa.org/abstract.cfm?URI=ao-32-4-607

[16] S. L. Jacques and B. W. Pogue, "Tutorial on diffuse light transport," *J Biomed Opt*, vol. 13, no. 4, p. 041302, 2008.

[17] T. Durduran, R. Choe, W. Baker, and A. Yodh, "Diffuse optics for tissue monitoring and tomography," *Reports on Progress in Physics*, vol. 73, no. 7, p. 076701, 2010.

[18] R. C. Haskell, L. O. Svaasand, T.-T. Tsay, T.-C. Feng, B. J. Tromberg, and M. S. McAdams, "Boundary conditions for the diffusion equation in radiative transfer," *J. Opt. Soc. Am. A*, vol. 11, no. 10, pp. 2727–2741, Oct 1994. [Online]. Available: http://josaa.osa.org/abstract.cfm?URI=josaa-11-10-2727

[19] V. Venugopalan, J. Spanier, C. Hayakawa, D. Cuccia, A. Gardner, J. Ranasinghesagara, L. Malenfant, and J. Nguyen, "Virtual photonics," Laser Microbeam and Medical Program (LAMMP: P41 EB015890-33), 2014, [Online; accessed April-2014]. [Online]. Available: http://www.virtualphotonics.org/

[20] K. S. No, R. Kwong, P. H. Chou, and A. Cerussi, "Design and testing of a miniature broadband frequency domain photon migration instrument," *J Biomed Opt*, vol. 13, no. 5, p. 050509, 2008.

[21] C. Sthalekar and V. Koomson, "A CMOS Sensor for Measurement of Cerebral Optical Coefficients Using Non-Invasive Frequency Domain Near Infrared Spectroscopy," *Sensors Journal, IEEE*, vol. 13, no. 9, pp. 3166–3174, Sept 2013.

[22] C. C. Sthalekar, Y. Miao, and V. J. Koomson, "Optical Characterization of Tissue Phantoms Using a Silicon Integrated fdNIRS System on Chip," *IEEE Transactions on Biomedical Circuits and Systems*, vol. 11, no. 2, pp. 279–286, April 2017.

[23] M. Grozing, B. Phillip, and M. Berroth, "CMOS ring oscillator with quadrature outputs and 100 MHz to 3.5 GHz tuning range," in *ESSCIRC 2004 - 29th European Solid-State Circuits Conference (IEEE Cat. No.03EX705)*, Sept 2003, pp. 679–682.

[24] U. Stehr, F. Henkel, L. Dalluge, and P. Waldow, "A fully differential CMOS integrated 4th order reconfigurable GM-C lowpass filter for mobile communication," in *10th IEEE International Conference on Electronics, Circuits and Systems, 2003. ICECS 2003. Proceedings of the 2003*, vol. 1, Dec 2003, pp. 144–147 Vol.1.

[25] H. Photonics. (2017) Home page. [Online]. Available: www.hamamatsu.com/us/en/index.html

[26] ——. Si APD, S12023 series datasheet. [Online]. Available: http://www.hamamatsu.com/resources/pdf/ssd/s12023-02_etc_kapd1007e.pdf

[27] S. M. Park and H.-J. Yoo, "1.25-Gb/s regulated cascode CMOS transimpedance amplifier for Gigabit Ethernet applications," *IEEE Journal of Solid-State Circuits*, vol. 39, no. 1, pp. 112–121, Jan 2004.

[28] A. Ghaffari, E. A. M. Klumperink, M. C. M. Soer, and B. Nauta, "Tunable High-Q N-Path Band-Pass Filters: Modeling and Verification," *IEEE Journal of Solid-State Circuits*, vol. 46, no. 5, pp. 998–1010, May 2011.

[29] M. Darvishi, R. van der Zee, and B. Nauta, "Design of Active N-Path Filters," *IEEE Journal of Solid-State Circuits*, vol. 48, no. 12, pp. 2962–2976, Dec 2013.

[30] S. Yazdi and M. Green, "A precise 360-range phase detector based on an N-path filter," in *2016 14th IEEE International New Circuits and Systems Conference (NEWCAS)*, June 2016, doi: 10.1109/NEWCAS.2016.7604831.

[31] S. S. Yazdi, A. E. Cerussi, and M. M. Green, "A precise 360-range phase detector for fdNIRS application using a pair of XNORs," in *2015 IEEE 58th International Midwest Symposium on Circuits and Systems (MWSCAS)*, Aug 2015, doi: 10.1109/MWSCAS.2015.7282161.

[32] A. Valdes-Garcia, R. Venkatasubramanian, J. Silva-Martinez, and E. Sanchez-Sinencio, "A Broadband CMOS Amplitude Detector for On-Chip RF Measurements," *IEEE Transactions on Instrumentation and Measurement*, vol. 57, no. 7, pp. 1470–1477, July 2008.

[33] K. Koli and K. Halonen, "A 2.5 V temperature compensated CMOS logarithmic amplifier," in *Proceedings of CICC 97 - Custom Integrated Circuits Conference*, May 1997, pp. 79–82.

[34] S. Sedighzadeh Yazdi, "A highly linear phase detector for frequency domain diffuse optical spectroscopy implemented in 0.18 μm standard CMOS," Ph.D. dissertation, University of California, Irvine, 2014, copyright - Database copyright ProQuest LLC; ProQuest does not claim copyright in the individual underlying works; Last updated - 2016-06-04. [Online]. Available: https://search.proquest.com/docview/1648640935?accountid=14509